Topological spin dynamics in 2D Bose Lattices

a thesis presented for the degree of

Doctor of Philosophy of Imperial College London

and the

Diploma of Imperial College

by

Bogdan Galilo

Department of Mathematics

Imperial College

180 Queen's Gate, London SW7 2BZ

September 2017

I certify that this thesis, and the research to which it refers, are the product of my own work, and that any ideas or quotations from the work of other people, published or otherwise, are fully acknowledged in accordance with the standard referencing practices of the discipline.

Signed: _____

Copyright

Thesis advisor: Dr Ryan Barnett Bogdan Galilo

Topological spin dynamics in 2D Bose Lattices

Abstract

This thesis presents theoretical work devoted to the manifestation of the edge states of boson topological band insulators in optical lattice experiments with weakly-interacting spinor condensates. Although the investigation is presented mainly on a spin-one Kane-Mele model, many aspects of this thesis can be generalised to other lattice models.

One major question this thesis addresses is the relevance of topological edge states in the dynamics of the interacting boson systems. This thesis shows how interactions in quenched spinor condensates can facilitate the manifestation of the edge states of two dimensional topological lattice models. Provided certain quench and symmetry-related conditions are fulfilled, the edge states are found to be populated exponentially fast right after the quench. A growing edge spin current is also described. A preliminary numerical computation for later times suggests a particle redistribution from the edge back into the bulk.

The presence of a harmonic potential in optical lattice experiments often obscures the manifestation of the edge states. In relation to this problem, spinor condensates have been considered, and a sharpening of the boundaries is observed in the Thomas-Fermi regime. Moreover, for spin-± 1 states, despite the presence of the external potential, one can recover a band structure similar to that of a non-interacting model with hard-wall boundaries. Approximate analytical expressions for the edge-state energies in the presence of a harmonic potential are derived.

The results presented in this thesis aim to widen the understanding of the manifestation of boson topological edge states, and are in line with the current experiments with ultracold atoms. The thesis suggests mechanisms of

experimentally probing boson topological edge states and their quench dynamics with spinor condensates.

To everyone who has been nice to me, who supported me, and believed in me

Acknowledgments

I warmheartedly thank my scientific advisor Dr Ryan Barnett for giving me the opportunity to do a PhD at Imperial College, for suggesting exciting research topics, for his invaluable criticism which helped me improve, and for his support during the course of my PhD. I would also like to thank Dr Derek K. K. Lee for fruitful collaboration, numerous discussions, and valuable comments. I am grateful for the Schrödinger Scholarship Scheme and for the Roth Studentship for providing financial support. Many thanks to the department of mathematics for creating a comfortable working environment. A big thank you to everyone who supported me during my studies, who shared their love and respect. Finally, I would like to thank Dr Joe Bhaseen and Dr Florian Mintert for carefully reading and commenting on this thesis.

List of figures

Contents

1

Introduction

Physical systems are often classified and investigated for their properties. Such properties are important for the fundamental understanding of the physical phenomena that the system can experience, as well as many applications. The properties of physical systems, however, can be drastically altered at the interface of the system with other media, or even vacuum [3–5]. Aluminium, for instance, is chemically a very reactive metal. When in contact with water or oxygen it reacts immediately. Why are airplanes, which are exposed to rain and air, safe to operate when aluminium alloys are abundantly used in aircraft construction? The common knowledge is that a thin layer of aluminium oxide is formed at the surface of aluminium. This layer prevents aluminium from further entering into a chemical reaction [4]. Physically one can interpret this layer formation as being due to electromagnetic interactions. At the contact of aluminium with oxygen, an interfacial state is formed, which results in completely different chemical properties from the two regions it separates. The properties of the interface states can have important application in electronic devices too. The surface of contact of a semiconductor and a metal are known to alter electronic properties of the system [3, 6]. This is precisely the phenomenon responsible for the break-

through in electronics of semiconductor devices [7–10]. One therefore has to admit that experimental detection and investigation of surface properties is of great importance to understanding the nature of the interface states and the resulting properties.

This thesis is dedicated to the discussion of other types of interface states, related to the latest discoveries in material science, the ones of topological band insulators [11–13]. These are compounds that proved to have an electronically conducting surface while remaining in an insulating state. Furthermore, the electric properties of the surface have been found to be robust to small impurities, dislocations and defects provided certain symmetries are preserved. The origin of these properties has been mapped to the presence of a non-trivial topology, which, roughly speaking, states that a smooth deformation of the Hamiltonian describing the system while preserving certain symmetries does not drastically alter the electric properties of the system. It can be mapped to the existence of topological invariants that admit geometrical interpretations, and often appear in the form of winding numbers, Chern invariants and Berry phases. Extensive research in topological insulators has led to discoveries of electronic properties, such as chiral edge currents and chiral spin dynamics, that are very robust. This promises to bring various applications of topological phenomena to spintronics, semiconductors, and other electronic devices.

Because this thesis makes use of properties of two-dimensional topological insulators, let us give a historic overview and the current state of the field from the perspective relevant to this thesis. Probably one of the most significant breakthroughs that led to extensive studies of topological phases of matter is the discovery of the quantum Hall effect in 1980 [14]. In 1980 Klitzing, Dorda, and Pepper reported a measurement of Hall conductivity quantised by integer amounts of e^2/h, where e is the elementary charge and h is Planck's constant. This allowed measurements of Planck's constant to unprecedented precision. The quantised Hall conductance did not fit the common classification of the electronic states of matter at the time. Phases of matter, such as superfluids or ferromagnets, were described by the absence or presence of symmetries. For instance, a fluid can well be considered

translationally invariant, however a phase transition to a crystal breaks this symmetry. Ferromagnetism, which is an ordered phase determined by the presence of a non-vanishing magnetization, is another example. Quantum Hall systems do not fit into this picture, and it became clear that a new type of phase of matter was required in order to compliment the knowledge of electronic properties of matter. In the early experiments the quantum Hall effect was observed to occur in two-dimensional systems, for example in semiconductor quantum wells, when a strong magnetic field perpendicular to the plane of the sample was applied. Since the discovery of the quantum Hall effect a theory has developed and numerous experiments have been run that exploit the phenomena of quantum Hall conductivity. Probably one of the most relevant to this thesis is the theoretical proposal by Haldane of a model that exhibits quantum Hall conductance without the need of magnetic fields [15]. This is an example of a Chern insulator, in that there is an energy gap in the bulk energy spectrum (the system is insulating in the bulk provided the Fermi energy sits within the energy gap) and the gap is bridged by edge states. We will refer to this model as the Haldane model in this thesis, which will be discussed in detail in the next chapter. Another important development of the theory of topological insulators is the model introduced by Kane and Mele [16]. We will often use this model in our computations. Unlike the Haldane model the Kane-Mele model has an emergent quantum Hall current, that apart from being unidirectional, has its direction dependent on the spin orientation (a quantum spin Hall current). Furthermore, Kane and Mele introduced a topological invariant (Z_2 invariant) that characterizes the states as trivial or nontrivial band insulators. The quantum spin Hall phase was a topologically nontrivial phase, which preserved the time reversal symmetry. The Haldane and Kane-Mele models are the simplest examples of two-dimensional topological phases of matter. Although these models represented a simple introduction to novel phases of matter, its experimental realisation was not possible at the time. A closer to experimental realisation was the work on topological insulators by Bernevig, Hughes, and Zhang [17]. It predicted a quantum spin Hall effect in inverted type-III HgTe/CdTe quantum wells. Later experiments have confirmed the predictions of the existence of the quantum spin Hall effect [18–20].

On the other hand, since the discovery of the quantum Hall effect [14], the enormous research done in topological phenomena exploits mainly fermionic states of matter, such as electronic states in solids. Manifestation of topological phenomena for bosons – the other major type of particles – is less well understood. It could possibly bring in new discoveries unveiling new properties of matter, but at the moment it faces considerable experimental challenge. Experiments designed to model topological phenomena for non-fermionic states have been done. These include engineering mechanical systems such as two-dimensional topological lattices of spinning gyroscopes [21], and photonic lattices [22–26]. While the former is a completely classical system, the latter may involve quantum phenomena. Both realizations have interesting chiral dynamics at the edge of the lattice, but lack interactions and quantum spin dynamics. Cold atoms experiments, on the other hand, can deal with bosons which carry spin degrees of freedom, and allow a high degree of control of interactions and other parameters in experiments. A difficulty in the investigation of boson topological dynamics of ultra-cold atoms is that at low temperatures bosons condense in the lowest energy state, and this leaves the topological edge states highly irrelevant for the dynamics of the system. Ways to overcome some of these challenges is what motivated this work.

This thesis aims towards unveiling the topological boson dynamics in optical lattice experiments with ultra-cold atoms. It investigates various problems related to the population of boson topological edge states, the effect of weak interactions and presence of soft boundaries in optical lattice experiments with cold atoms. Chapter 2 equips the reader with basic concepts of topological band insulators, relevant lattice models, and basic features of ultracold atoms and optical lattice experiments that are at the heart of this thesis, and which are often utilised in the next Chapters. The main results of this thesis are presented in Chapter 3 to 6. Chapter 3 gives an insight on the Generating Function Technique of computing topological edge states analytically. Using this method the single-particle edge-state energies of the Haldane model [15] for an arbitrary local magnetic flux, and the edge-state energies of the Harper-Hofstadter model [27–31] for $2\pi/3$ magnetic flux per placket

have been analytically derived. The author of this thesis is not aware of any previous derivation of the exact analytical expressions of the specified models. In order to tackle the issue of probing the dynamics of spin one bosons in topological two-dimensional lattice models a quenching mechanism that involves a quadratic Zeeman term and a phenomenon known as dynamical instability are applied in Chapter 4. The idea suggests that the dynamics of a system driven out of equilibrium can be dominated by the edge(surface)-states provided certain conditions are fulfilled. A spin one generalization of the Kane-Mele model [16] is used to illustrate the concept, and the role of symmetries in this model is discussed. The results suggest a way that might allow for direct experimental observation of topological properties of weakly interacting bosons in optical lattice experiments, with consequences for the overall dynamics of the system. However, sharp boundary conditions similar to the ones encountered in solids for electrons have been implied to obtain the results in Chapter 4. Although experiments that design sharp boundaries have been created in cold atom experiments [32–34], the commonly adopted way of confining atoms is a harmonic trap which induces soft boundary conditions. Chapter 5 suggests a way to overcome the difficulty of soft boundaries in lattice experiments with spin one bosons. The effect of the harmonic potential on the topological manifestation of edge states in an interacting two-dimensional boson lattice model is thoroughly investigated, and it is shown that a band structure similar to the non-interacting model can be reconstructed for the spin ± 1 components of the spin fluctuation of the condensate. A rather generic analytical expression for the relevant edge-state energies is derived, and a bulk-boundary correspondence is obtained for a two-dimensional lattice model of interacting bosons in presence of harmonic confinement. The effect is illustrated on the spin-one Kane-Mele model [16]. All the derived expressions have been compared with numerical mean-field simulations, and show agreement. Chapter 6 offers an insight into the quench dynamics, discussed in Chapter 4, at later times after the quench. A numerical computation suggests a particle redistribution from the edge back into the bulk. The thesis concludes with an overview and a short discussion of the results combined in one picture. An outlook of open questions and motivation for future research finalises this thesis.

Some of the results presented in this thesis also appear in

- Chapter 4: Bogdan Galilo, Derek K. K. Lee, and Ryan Barnett, *Selective Population of Edge States in a 2D Topological Band System*, Phys. Rev. Lett. **115**, 245302 (2015)[1]

- Chapter 5: Bogdan Galilo, Derek K. K. Lee, and Ryan Barnett, *Topological Edge-State Manifestation of Interacting 2D Condensed Boson-Lattice Systems in a Harmonic Trap*, Phys. Rev. Lett. **119**, 203204 (2017)[2]

2

Background material (Models, Methods, Techniques)

This thesis is about topological condensed matter phenomena of ultra-cold atoms in optical lattices. In this chapter we give an overview of relevant background on both condensed matter phenomena of two dimensional topological band insulators, and ultra-cold atoms, on which this work heavily relies.

2.1 2D topological band insulators

Physics of the topological band insulators is a direction of condensed matter research. It comes from solid state physics where electronic states are of major interest. The interest in topological insulators comes in part, from the electric properties of the surface (edges) of the system, where under certain circumstances only the surface (edge) is electrically conductive. Moreover the surface (edge) conductivity comes in quanta when a bias electro-magnetic

field is applied, i.e. it is quantised. There are many ways to introduce topological band insulators. In what follows we bring a simple explanation of topological phenomena based on Bloch states in 2D lattice models, which is the most relevant to our thesis, and which should help the reader unfamiliar with these concepts to understand the research presented in this thesis. The reader, however, is encouraged to consult the relevant literature for more information on topological phenomena in condensed matter systems [11–13, 35].

A two-dimensional lattice is a periodic structure in the sense that it can be described by translations of a single unit cell along two directional vectors, called primitive lattice vectors. Due to translational symmetry along the primitive vectors the single particle states on the lattice can be described by Bloch states $|\psi(\mathbf{k})\rangle = e^{i\mathbf{k}\cdot\mathbf{r}} |u(\mathbf{k})\rangle$, where $\mathbf{r}$ is the lattice coordinate, $\mathbf{k}$ represents the wave-vector, and $|u(\mathbf{k})\rangle$ has the periodicity of the lattice. The states $|u(\mathbf{k})\rangle$ are defined up to an arbitrary phase $\phi(\mathbf{k})$. This reflects a local symmetry in k-space:

$$|u(\mathbf{k})\rangle \to e^{i\phi(\mathbf{k})} |u(\mathbf{k})\rangle . \tag{2.1}$$

Similar to a $U(1)$ gauge field one can introduce in $\mathbf{k}$-space an analogue to vector potential:

$$\mathbf{A} = -i \langle u(\mathbf{k})| \nabla_{\mathbf{k}} |u(\mathbf{k})\rangle , \tag{2.2}$$

and a 'magnetic' flux:

$$\gamma = \int_{\mathbb{BZ}} [\nabla_{\mathbf{k}} \times \mathbf{A}]_z d^2\mathbf{k}, \tag{2.3}$$

where the integral is taken over the Brillouin zone. The above quantities are known as Berry connection and Berry phase respectively [35, 36]. Both are due to the symmetries of the lattice Hamiltonian and at a first sight seem not to effect the physical observables. However, similarly to the electromagnetic gauge potential, the above quantities in certain circumstances can have an impact on observables such as the Hall conductivity. Band insulators

that exhibit non-zero Berry fluxes are called topological band insulators. We will come back to the quantities we just introduced when we will describe the edge-states of topological band insulators in the next chapters. In what follows we give a description of several models that have a non-trivial topological band structure. These include Su-Schrieffer-Heeger (SSH) [37, 38], Haldane [15] and Kane-Mele [16].

2.1.1 Su-Schrieffer-Heeger (SSH) Model

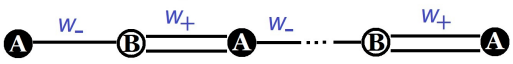

Figure 2.1: The lattice structure of the Su-Schrieffer-Heeger model.

The Su-Schrieffer-Heeger (SSH) model was introduced in the context of describing the electrical conductivity of the polymer polyacetylene [37, 38]. The model, however, has been considered in many contexts, not just for electronic states of the polyacetylene. It is probably the simplest lattice model one can write which exhibits non-trivial topological structure.

Consider a one-dimensional chain of N sites that can be populated by particles that can move from one site to its neighbour at a time. The simplest scenario is when it takes the same probability for a particle to move from one site to another. This can be encoded mathematically by introducing creation and annihilation operators for particles at each site j, $\hat{a}_j^\dagger$ and $\hat{a}_j$ respectively, and the Hamiltonian:

$$\hat{\mathcal{H}} = -w \sum_j (\hat{a}_j^\dagger \hat{a}_{j-1} + h.c.) - \mu a_j^\dagger \hat{a}_j \tag{2.4}$$

where the sum is taken along the chain sites and μ is the chemical potential. For instance, if the particles are fermions and the system is half-filled, $\mu = 0$. Here $\hat{a}_{j-1}$ annihilates a particle at site $j-1$, and $\hat{a}_j^\dagger$ creates a particle at the neighbour site j. The likelihood of hopping from one site to its neighbour is determined by w, while the bosonic (fermionic) nature of particles is encoded in the (anti-)commutation relations: $\hat{a}_j \hat{a}_j^\dagger \pm \hat{a}_j^\dagger \hat{a}_j = 1$ with the $+$ sign for

fermions and $-$ for bosons.

With periodic boundary conditions, the Hamiltonian (2.4) is readily diagonalisable by introducing new single particle operators $\hat{a}_k = \frac{1}{\sqrt{N}} \sum_j e^{ikj} \hat{a}_j$:

$$\hat{\mathcal{H}} = -\sum_k (2w \cos k + \mu) \hat{a}_k^\dagger \hat{a}_k. \tag{2.5}$$

It implies the existence of a band, and no gaps in the single particle energy spectrum. This corresponds to a metallic phase.

Importantly, the metallic phase in (2.4) could change to an insulating phase by breaking a certain symmetry. An insulating phase is reflected in the quasiparticle energy spectrum by the presence of an energy gap. The SSH model that we introduce below is a simple modification of (2.4) that opens such a gap. For (2.4) a gap opening can be achieved, for instance, by relaxing the requirement of having the same hopping amplitude from one site to another. This can be pictured as sites being connecting by bonds of different strength. Let us denote the odd sites by A and the even ones by B. Given the chain is aligned horizontally, the particles can come to the site B from the left or from the right. For the SSH model the likelihood of moving from the right from A to B is shifted, resulting in a shift of w by some amount δw. Moving from the left to site B compensates by $-\delta w$ (Fig. 2.1). This physics is described by the SSH Hamiltonian:

$$\hat{\mathcal{H}}_{\text{SSH}} = -\sum_j (w + (-1)^j \delta w) \hat{a}_j^\dagger \hat{a}_{j-1} + h.c. - \mu a_j^\dagger \hat{a}_j, \tag{2.6}$$

or if one relabels the operators,

$$\hat{\mathcal{H}}_{\text{SSH}} = -\sum_l (w_- \hat{a}_{Al}^\dagger \hat{a}_{Bl} + w_+ \hat{a}_{Al+1}^\dagger \hat{a}_{Bl} + h.c.) - \mu a_{Al}^\dagger \hat{a}_{Al} - \mu a_{Bl}^\dagger \hat{a}_{Bl} \tag{2.7}$$

where l labels the sites in the A (B)- sublattice and $w_\pm = w \pm \delta w$. Due to translational symmetry along l the above Hamiltonian can be simplified in

terms of $\hat{a}_{A(B)k} = \frac{1}{\sqrt{N}} \sum_l e^{ikl} \hat{a}_{A(B)l}$:

$$\hat{\mathcal{H}}_{\mathrm{SSH}} = \sum_k \sum_{\alpha,\beta=A,B} \hat{a}^\dagger_{\alpha k} \mathcal{H}^{\alpha\beta}_{\mathrm{SSH}}(k) \hat{a}_{\beta k}, \tag{2.8}$$

where

$$\mathcal{H}_{\mathrm{SSH}}(k) = h_0(k)\mathbb{I}_2 + \mathbf{h}(k) \cdot \boldsymbol{\sigma} \tag{2.9}$$

is a 2×2-matrix that can be decomposed in Pauli matrices $\boldsymbol{\sigma} = (\sigma_1, \sigma_2, \sigma_3)^{\mathrm{T}}$ and identity matrix $\mathbb{I}_2$ acting in the sublattice space. The decomposition coefficients are given by:

$$\begin{aligned} h_0(k) &= -\mu, & h_1(k) &= -(w - \delta w) - (w + \delta w)\cos k, \\ h_2(k) &= (w + \delta w)\sin k, & h_3(k) &= 0. \end{aligned} \tag{2.10}$$

The excitation energy spectrum is obtained by diagonalising $\mathcal{H}_{\mathrm{SSH}}(k)$ and consists of two bands of energy $-\mu \pm \sqrt{h_1^2(k) + h_2^2(k)}$ separated by a gap of the order of $2\delta w$. If the chemical potential is adjusted for the Fermi-energy to sit in the gap, then no excitations can be created until one overcomes the gap energy, so the system is said to be in an insulating phase.

Now, let us consider a finite system, which starts with a bond of strength $w_- = w - \delta w$, as it is shown in Fig. 2.1. Although there is no real difference between $\delta w < 0$ and $\delta w > 0$ for a periodic system, there is a considerable difference when open boundary conditions are considered. In fact, the two phases, $\delta w > 0$ and $\delta w < 0$, are topologically distinct. The manifestation of this difference in topological phases can be observed at the edge of the system. For $\delta w < 0$ there are no available states within the energy gap and the system is in a normal insulating phase. However, for $0 < \delta w < w$ edge states with a mid-gap energy appear. This is a signature of a topological phase. For a semi-infinite chain the edge-states are created by $\sum_l \phi_l \hat{a}^\dagger_{Al}$ with

$$\phi_l = (-1)^l \left(\frac{w - \delta w}{w + \delta w} \right)^l. \tag{2.11}$$

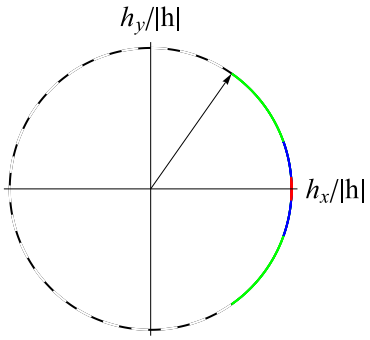

Figure 2.2: As k runs from 0 to 2π the unit vector $\mathbf{h}/|\mathbf{h}|$ covers an arc for $\delta w < 0$ and goes a full circular revolution for $\delta w > 0$, which corresponds to a non-trivial topological phase. Here green arc corresponds to $\delta w = -0.1w$, blue arc to $\delta w = -0.5w$, and red arc to $\delta w = -0.85w$.

The above expression will be derived in the following chapter as its derivation deserves a separate discussion.

The transition from normal insulating phase to a topological one occurs through a metallic phase at $\delta w = 0$ when the gap closes and δw changes the sign. The Zak phase, similar to the Berry phase, is an invariant for one-dimensional systems that does not change unless a topological phase transition occurs. It can be expressed in terms of bulk single-particle states:

$$Z^{(\nu)} = i \int_0^{2\pi} \phi_k^{(\nu)\dagger} \partial_k \phi_k^{(\nu)} dk, \tag{2.12}$$

where $\phi_k^{(\nu)}$ are the periodic in k (bulk) eigenvectors of $\mathcal{H}_{\mathrm{SSH}}$. The Zak phase vanishes in the normal insulating phase and is an integer multiple of π in topologically non-trivial phase ($\delta w > 0$). A geometrical interpretation can be given where the vector $\mathbf{h}(k)/|\mathbf{h}(k)|$ undergoes a full circular revolution around $\mathbf{h} = 0$ while k runs from 0 to 2π only in topological phase (Fig. 2.2).

2.1.2 Graphene and Haldane Models

Similar to one-dimensional metallic and insulating lattice models one can think of two-dimensional ones. However, there are many more ways to introduce a lattice in two-dimensions. In order to align with the context of

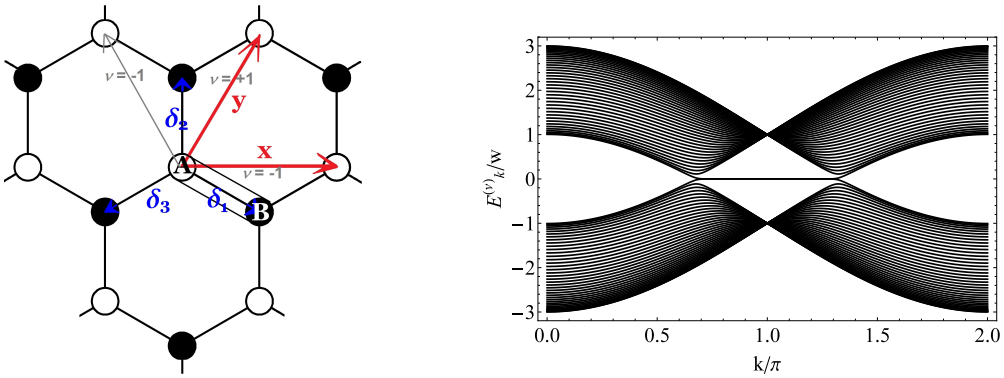

Figure 2.3: Left: The honeycomb lattice structure. Right: Energy spectrum of graphene with open boundary conditions applied in y-direction. A zero-energy dispersion of the edge-states connecting two Dirac cones is observed. Here k is the wave vector along x-direction, and $\mu = 0$.

this thesis, consider a two-dimensional system on a hexagonal lattice. The particles can move to the nearest sites along the three displacement vectors $\boldsymbol{\delta}_1$, $\boldsymbol{\delta}_2$ and $\boldsymbol{\delta}_3$ (Fig. 2.3). The unit cell contains two sites. These belong to two different sublattices, which we denote by A and B. The corresponding Hamiltonian

$$\hat{\mathcal{H}}_{\text{graphene}} = -w \sum_{\langle ij \rangle} \hat{a}_i^\dagger \hat{a}_j - \mu \sum_j \hat{a}_j^\dagger \hat{a}_j \tag{2.13}$$

can be reduced again to

$$\hat{\mathcal{H}}_{\text{graphene}} = \sum_{\substack{\mathbf{k} \\ \alpha,\beta=A,B}} \left(h_0(\mathbf{k}) \mathbf{I}_2 + \mathbf{h}(\mathbf{k}) \cdot \boldsymbol{\sigma}^{\alpha\beta} \right) \hat{a}_{\alpha\mathbf{k}}^\dagger \hat{a}_{\beta\mathbf{k}} = \sum_{\substack{\mathbf{k} \\ \alpha,\beta=A,B}} \mathcal{H}^{\alpha\beta}(\mathbf{k}) \hat{a}_{\alpha\mathbf{k}}^\dagger \hat{a}_{\beta\mathbf{k}}, \tag{2.14}$$

where $\langle ij \rangle$ represents summation over nearest neighbour sites, and $\hat{a}_{A(B)\mathbf{k}} = \frac{1}{\sqrt{N}} \sum_l e^{i\mathbf{k}\cdot\mathbf{l}} \hat{a}_{A(B)\mathbf{l}}$ with $\mathbf{l}$ labelling the unit cells. In the above expression

$$\begin{aligned} h_0(\mathbf{k}) &= -\mu, & h_1(\mathbf{k}) &= -w \textstyle\sum_{\eta=1}^3 \cos \mathbf{k} \cdot \boldsymbol{\delta}_\eta, \\ h_2(\mathbf{k}) &= -w \textstyle\sum_{\eta=1}^3 \sin \mathbf{k} \cdot \boldsymbol{\delta}_\eta, & h_3(\mathbf{k}) &= 0. \end{aligned} \tag{2.15}$$

This is commonly used to describe conduction band structure in graphene [39, 40] in the tight-binding approximation. Its energy spectrum has two bands

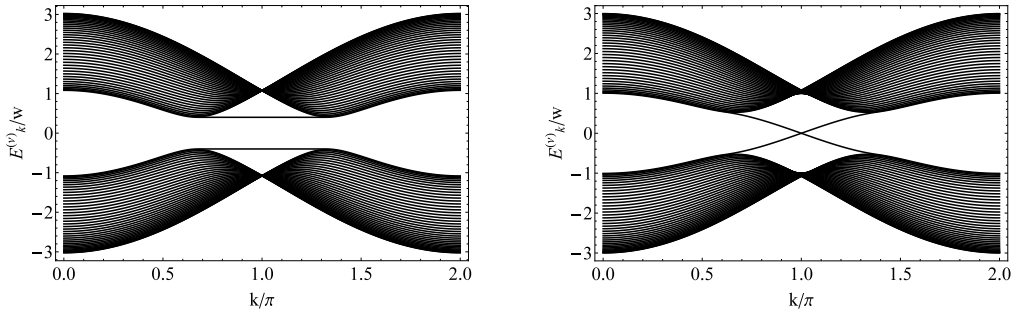

Figure 2.4: The energy spectrum of the Haldane model. Left: The gap is opened through the inversion symmetry breaking (2.16) with $\lambda = 0.4w$. Right: The time-reversal symmetry is broken by (2.17) with $\lambda = 0.2w$. Open boundary conditions are applied in the y-direction, and periodic in the x-direction. Here k is the wave vector along x-direction, and $\mu = 0$.

due to the two sublattices. The energy spectrum is, however, gapless (Fig. 2.3). Similar to the SSH model one can open a gap by breaking a symmetry. Two symmetries are present in the graphene model: inversion and time reversal symmetries. The inversion symmetry reads $\sigma_1 \mathcal{H}(\mathbf{k})\sigma_1 = \mathcal{H}(-\mathbf{k})$, while time reversal symmetry requires that the complex conjugated Hamiltonian $\mathcal{H}(\mathbf{k})^* = \mathcal{H}(-\mathbf{k})$. To break the inversion symmetry it is sufficient to add a constant staggering term

$$h_3(\mathbf{k}) = \lambda. \tag{2.16}$$

This opens a gap in the energy spectrum. If hard wall boundaries are imposed, states localised at the edge can emerge. However, no dispersion crosses the gap even for the emergent edge states (see Fig. 2.4). The system is then said to be in a normal insulating phase.

The emergence of edge states manifests differently if only the time reversal symmetry is broken. The time reversal symmetry can be broken, for instance, by adding the following term to the Hamiltonian:

$$h_3(\mathbf{k}) = \lambda \sum_{\eta,\eta',\eta''=1}^{3} \epsilon_{\eta\eta'\eta''} \sin \mathbf{k} \cdot (\boldsymbol{\delta}_{\eta'} - \boldsymbol{\delta}_{\eta''}), \tag{2.17}$$

where $\epsilon_{\eta\eta'\eta''}$ is Levi-Civita symbol. The emergent edge-states cross the gap as shown in Fig. 2.4. The term (2.17) can be justified by considering the

existence of a local magnetic-flux normal to the lattice plane, which mimics the symmetry of the lattice, and sums to zero net flux through the unit cell. The particle hopping to next-nearest neighbour site can generally obtain a phase ϕ due to magnetic flux, which can be expressed by an additional term to a spinfull version of the graphene Hamiltonian (2.13):

$$\delta\hat{\mathcal{H}} = \lambda \sum_{\langle\langle ij \rangle\rangle} e^{i\phi_{ij}} \hat{a}_i^\dagger \hat{a}_j + \text{H.c.} \tag{2.18}$$

The phase $\phi_{ij} = \pm\phi$ has to be of opposite sign for the two sublattices in order to cancel the net flux through the unit cell. Haldane showed that by opening the gap in this way the system becomes topologically non-trivial [15]. The corresponding Bloch Hamiltonian reads:

$$\hat{\mathcal{H}}_{\text{Haldane}} = \sum_{\mathbf{k}} h_0(\mathbf{k})\mathbb{I}_2 + \mathbf{h}(\mathbf{k}) \cdot \boldsymbol{\sigma}, \tag{2.19}$$

with

$$h_0(\mathbf{k}) = -2\lambda \cos\phi \sum_{\eta=1}^{3} \cos(\mathbf{k} \cdot \mathbf{b}_\eta) - \mu, \qquad h_1(\mathbf{k}) = -w \sum_{\eta=1}^{3} \cos(\mathbf{k} \cdot \boldsymbol{\delta}_\eta),$$
$$h_2(\mathbf{k}) = -w \sum_{\eta=1}^{3} \sin(\mathbf{k} \cdot \boldsymbol{\delta}_\eta), \qquad h_3(\mathbf{k}) = -2\lambda \sin\phi \sum_{\eta=1}^{3} \sin(\mathbf{k} \cdot \mathbf{b}_\eta).$$

It reduces to (2.17) for $\phi = \pi/2$. The energy spectrum has two bulk bands which for $\phi = \pi/2$ are:

$$\epsilon^{(\pm)}(\mathbf{k}) = -\mu \pm \big[w^2(3 + 2\cos k_x + 2\cos k_y + 2\cos(k_x - k_y)) \tag{2.20}$$
$$+\lambda^2(\sin k_y - \sin k_x - \sin(k_y - k_x))^2\big]^{1/2}. \tag{2.21}$$

The two energy dispersions that cross the gap are due to two edge states:

$$\epsilon_{\text{edge}}(\mathbf{k}) = -\mu \pm \frac{6\lambda \sin k}{\sqrt{w^2 + 16\lambda^2 \sin^2(k/2)}}, \tag{2.22}$$

where k is either k_x or k_y depending on whether the lattice periodicity is preserved in the x or y direction respectively. The derivation of the energy dispersion for the edge states requires a separate discussion and is given in the following chapter.

Edge-states crossing the gap can lead to observable effects in experiments and applications. When one selectively excites states within the energy gap only the edge-states contribute to the dynamics of the system. For electrons in solids one can effectively adjust the chemical potential for the Fermi energy to sit in the gap. For bosons, however, it is considerably more subtle since bosons do not form a Fermi sea. How to probe the edge-states dynamics of boson systems is the main question addressed in this thesis and ways to do it are suggested in the following chapters.

2.1.3 Kane-Mele Model

In what will be described in the following chapters, symmetries such as time-reversal symmetry play an important role. For reasons that will be made clear later, we would like to preserve the time-reversal symmetry while having chiral edge-states crossing the gap. The Haldane model does not fit this requirement. An extension of Haldane's model that preserves time-reversal symmetry is the Kane-Mele model [16]. We first extend our particle operators $\hat{a}_{j\sigma}$ by adding a spin index σ. More accurately the following term is added to the graphene Hamiltonian (2.13):

$$\hat{\mathcal{H}}_{\mathrm{SO}} = \lambda \sum_{\langle\langle ij \rangle\rangle} i\nu_{ij} \sum_{\sigma\sigma'} \hat{a}^{\dagger}_{i\sigma} S_z^{\sigma\sigma'} \hat{a}_{j\sigma'}, \tag{2.23}$$

where S_z is the 3rd spin matrix. For electronic states, S_z is the third Pauli matrix. In the future chapters, however, we consider bosons, which have spin 1. In this case

$$S_z = \begin{pmatrix} 1 & 0 & 0 \\ 0 & 0 & 0 \\ 0 & 0 & -1 \end{pmatrix}. \tag{2.24}$$

The term (2.23) vanishes for zero-spin components and decouples from the rest. Its energy spectrum reduces to the graphene model (2.13). Each of the spin-± 1 components is described by a Haldane model with the phase $\phi = \pm\pi/2$ correspondingly. However, the spin-± 1 components acquire opposite

phases while a particle moves to the next nearest-neighbour site. The energy spectrum for the spin-± 1 component will thus coincide with the Haldane model Fig. 2.4 (Right), with the exception of the opposite spin components of edge-states having opposite chirality.

2.2 Ultra-cold atomic gases

Advances in experiments with ultra-cold atomic gases and optical lattices allowed the realisation of many exciting phenomena such as Bose-Einstein condensates, atom interferometers, investigation of spinor condensates, etc. The most relevant application of ultra-cold gases to the current thesis is the modelling of Bose-Hubbard lattice models. In what follows we give a brief explanation of the field, and the key processes that are involved in cooling, trapping and realising lattice models of bosonic atoms. A more detailed review of these questions can be found in the literature [41–44].

Ultracold gases are dilute states of atoms at temperatures of the order and lower than a micro-Kelvin (μK). Atoms are generally prevented from forming a solid when the mean interatomic distance is much larger than the radius of interatomic interaction R_e:

$$\bar{\rho}^{\,-1/3} \gg R_e, \tag{2.25}$$

where $\bar{\rho}$ is the gas mean density. This is so called *dilute* limit. In this limit the motion of the atoms can be considered free. Once the atoms approach distances of the order and smaller than R_e the inter-atomic interactions play an important role. At very small temperatures, when the thermal de Broglie wavelength of the atomic gas, Λ_T, greatly exceeds the interaction radius, R_e, an *ultracold* regime is achieved. The de Broglie wavelength

$$\Lambda_T = \left(\frac{2\pi\hbar^2}{m k_B T} \right)^{1/2}, \tag{2.26}$$

where m is the atomic mass, increases with the decrease of temperature T. At high enough temperatures, for which $\bar{\rho}^{\,-1/3} \gg \Lambda_T$, the gas obeys

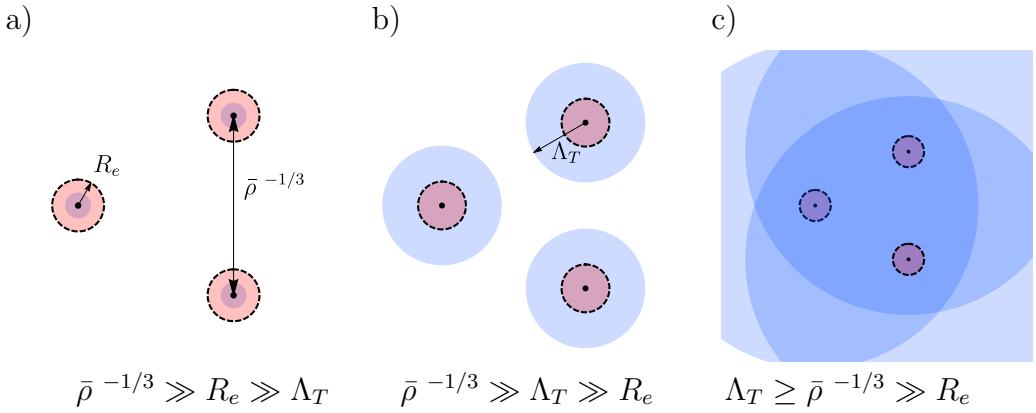

Figure 2.5: Schematic illustration of the length scales involved in a transition from a dilute gas of atoms (a) to a quantum ultracold gas (c). The characteristic length scales are the mean particle separation $\bar{\rho}^{-1/3}$, the interatomic interaction range R_e, and the atomic thermal de Broglie wavelength Λ_T.

Boltzmann statistics and therefore can be considered *classical*. At very low temperatures, for which Λ_T becomes comparable to the interatomic separation length scale $\bar{\rho}^{-1/3}$, quantum effects become relevant. In regimes of $\bar{\rho}^{-1/3} \leq \Lambda_T$ the gas obeys quantum statistics, and as a result in the regime of ultracold temperatures macroscopic properties of the gas depend on whether the atoms are bosons or fermions. The gas is then said to be *quantum*. If the temperatures are small enough, smaller than a certain characteristic critical temperature of the gas, a quantum degeneracy is reached. For bosons, which are the main topic of this thesis, the underlining degeneracy is reflected in the macroscopic occupation of the lowest energy state. Such a state is called *Bose-Einstein condensate* (BEC).

Currently many scientific laboratories all around the world do research with ultracold atoms and optical lattices. The first quantum gases, however, were created in 1995 at JILA (atoms of ^{87}Rb [45]), at MIT (atoms of Na [46]), and at Rice (atoms of ^{7}Li [47]).

2.2.1 Zeeman effect

Atoms can be manipulated using magnetic fields. This may sound surprising since atoms are electrically neutral. However, atoms are composite particles

made out of a positively charged core of nucleons (protons and neutrons), and negatively charged electrons. Both nucleus and electrons have their own magnetic moments, $\boldsymbol{\mu}_n$ and $\boldsymbol{\mu}_e$ respectively, which couple to external magnetic fields. The energy of such coupling is $-(\boldsymbol{\mu}_n + \boldsymbol{\mu}_e) \cdot \mathbf{B}$, where $\mathbf{B}$ is the external magnetic field. The alkali atoms, which are commonly used in experiments with ultra-cold atoms, have a single valance electron on the outer shell. The electrons from the other electron shells screen out the electromagnetic fields and do not contribute to the total magnetic moment of the electron cloud of alkali atoms. Since the valance electron of alkali atoms occupies the s-orbital with orbital angular momentum $\mathbf{l} = \mathbf{0}$ the total electron magnetic moment is determined by the valance electron spin $\mathbf{s}$ alone:

$$\boldsymbol{\mu}_e = -g_s \mu_B \mathbf{s}, \tag{2.27}$$

where $g_s \approx -2$ is known as electron g-factor, and $\mu_B = \dfrac{e\hbar}{2M_e c}$ is called the Bohr magneton, where e and M_e are the elementary charge and electron mass correspondingly. The nuclear magnetic moment is determined by the orbital motion of positively charged protons, and by the proton and neutron spins. These effectively sum up to a nuclear spin $\mathbf{I}$. For alkali atoms like ^{23}Na, ^{39}K and ^{87}Rb $I = 3/2$. The total nuclear magnetic moment is therefore given by

$$\boldsymbol{\mu}_n = -g_I \mu_N \mathbf{I}, \tag{2.28}$$

where g_I is the nuclear g-factor, and $\mu_N = \dfrac{e\hbar}{2M_n c}$ is the nuclear magneton, where M_n is the nucleon mass. Even in the absence of any external magnetic field the electrons interact with the nucleus electromagnetically. In the absence of such interaction the nucleus and electron magnetic moment degrees of freedom decouple, which results in degeneracy of states with a fixed I but different s values. An electromagnetic interaction between the nucleus and electron moments, however, persists. This leads to a lifting of degeneracy, referred to as hyperfine splitting. The Hamiltonian describing the hyperfine coupling is:

$$\hat{\mathcal{H}}_{\text{hf}} = A\hat{\mathbf{I}} \cdot \hat{\mathbf{s}}, \tag{2.29}$$

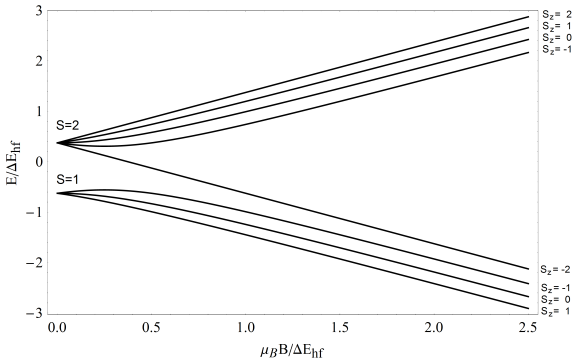

Figure 2.6: Hyperfine splitting of energy levels of alkali atoms with nuclear spin $I = 3/2$ in presence of magnetic field B. Here the energy is shown in units of hyperfine splitting energy at zero magnetic field $\Delta E_{\rm hf}$, and μ_B is Bohr magneton.

where $\hat{\mathbf{I}}$ and $\hat{\mathbf{s}}$ denote the nucleus and electron spin operators. The value of coefficient A is usually determined experimentally by measuring the hyperfine splitting $\Delta E_{\rm hf}$ in the absence of a magnetic field:

$$A = \frac{2\Delta E_{\rm hf}}{2I+1}. \tag{2.30}$$

The presence of an external magnetic field lifts the state degeneracy further (Fig. 2.6) and is described by the Hamiltonian

$$\hat{\mathcal{H}}_{\rm hf}(\mathbf{B}) = A\hat{\mathbf{I}}\cdot\hat{\mathbf{s}} - (\hat{\boldsymbol{\mu}}_e + \hat{\boldsymbol{\mu}}_n)\cdot\mathbf{B}. \tag{2.31}$$

One can neglect the nuclear magnetic moment $\hat{\boldsymbol{\mu}}_n$ in the above expression because of it being considerably smaller than the electron moment due to the nucleus being heavier. The Hamiltonian (2.31) commutes with the total angular momentum operator of the atom (atom spin) $\hat{\mathbf{S}} = \hat{\mathbf{I}} + \hat{\mathbf{s}}$ projected along the magnetic field direction. Labelling our z axis along the magnetic field, and m_I and m_s the nuclear and spin components along the magnetic field respectively, the conservation of $(\hat{\mathbf{I}} + \hat{\mathbf{s}})\cdot\mathbf{B}$ implies $m_S = m_I + m_s$ is a good quantum number. The Hamiltonian (2.31) then decouples for states with fixed $m_I + m_s$. For ^{87}Rb and ^{23}Na atoms, which are relevant to this thesis, $I = 3/2$ and $S = 3/2 - 1/2 = 1$. Assuming the magnetic field is small,

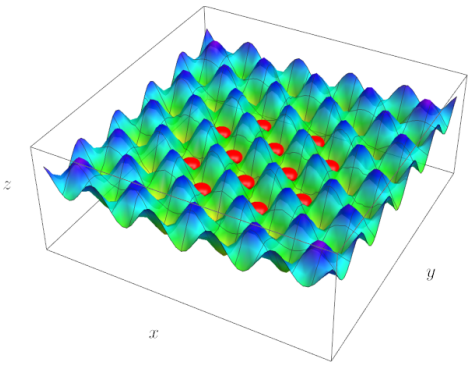

Figure 2.7: Illustration of how atoms are trapped in an optical lattice experiment. Here are shown waves of light in horizontal directions with atoms (red balls) being trapped in local minima of the potential.

the $\hat{\mathcal{H}}_{\rm hf}(\mathbf{B})$ can be approximately diagonalised to give:

$$E_{S=1} \approx -pm_S + q(m_S^2 - 1), \tag{2.32}$$

where $p = \mu_B B/2$ and $q = p^2/\Delta E_{\rm hf}$. The above energy values correspond to the eigenstates of the Hamiltonian:

$$\hat{\mathcal{H}} = -p\hat{S}_z + q(\hat{S}_z^2 - 1), \tag{2.33}$$

where $\hat{S}_z$ is the component of spin operator along the magnetic field $\mathbf{B}$. The linear term in $\hat{S}_z$ corresponds to the linear Zeeman term, while the quadratic term is called quadratic Zeeman term. For more detailed information on Zeeman interaction the reader can consult for instance [42, 44, 48, 49].

In later chapters, q will play a crucially important role. In particular, it is a parameter we use to quench.

2.2.2 Atom trapping techniques

Using external electromagnetic fields several techniques have been engineered to trap and control atoms. For reasons of a general overview of the field we briefly describe some of the main techniques below. Though such a description improves the understanding of the current thesis, it is not main topic of the thesis and the reader is advised to consult further literature [41, 42] if

necessary.

Magneto-Optical Trap (MOT). A nonuniform stationary magnetic field can be used to confine atoms in magneto-optical traps. Such field interacts with the magnetic moment of the atoms and induces an attractive force towards the minimum of the magnetic field. The Ioffe-Pritchard magnetic trap is the most commonly used magnetic trap. The decreasing magnetic field at the edges of the trap serves as a potential wall for the atomic gas trapped inside. Though these traps have been one of the first traps to confine atoms in experiments, nowadays optical lattices serve a more versatile trapping mechanism.

Optical lattices. Stark effect. Atoms can be trapped using optical lattices, a periodic interference pattern of shined laser beams. Subjected to an electric field $\mathbf{E}(\mathbf{r},t) = \mathbf{E}(\mathbf{r})e^{-i\omega t} + \mathbf{E}^*(\mathbf{r})e^{i\omega t}$ atoms acquire electric dipole moments $\mathbf{d}$ which couples to the field, and which, depending on the field frequency ω, drives the atoms towards the intensity minima/maxima of the optical lattice. This mechanism is known as the Stark effect, and can be understood as follows. A change in external electric field changes the energy of an atom from its ground state energy E_0 by an amount of

$$\Delta E = -\frac{\langle \mathbf{E}^2(t)\rangle_t}{2\hbar} \sum_n |\langle n|\hat{\mathbf{d}}\cdot\hat{\boldsymbol{\epsilon}}||0\rangle|^2 \frac{2\omega_{n0}}{\omega_{n0}^2 - (\omega + i\Gamma_n)^2}, \tag{2.34}$$

where $\langle\ \rangle_t$ denotes the time average over one oscillation period of the electric field, $\hat{\boldsymbol{\epsilon}}$ is the unit vector along the direction of the electric field, $\hbar\omega_{n0} = E_n - E_0$ is the transition energy from the ground state $|0\rangle$ to the unperturbed excited state $|n\rangle$ with energy E_n. We also introduced the decay rate due to spontaneous emission Γ_n. The energy change (2.34) can be regarded as an effective potential. The electric field consequently induces a force, which is the gradient of the potential. Suppose the sum in (2.34) is dominated by a resonance frequency ω_R. For alkali atoms of ^{23}Na and ^{85}Rb, for instance, ω_R is 589nm and 780nm respectively [50], which can be accessed by lasers. If the laser frequency ω is close to the resonance one, i.e. the detuning $\delta = \omega - \omega_R$

is small in comparison to ω_R, then the sign of ΔE is determined by the sign of δ. When $\delta > 0$ (blue detuning) the energy change ΔE is positive and the atoms experience a force towards low electric field regions. When $\delta < 0$ (red detuning) the energy change ΔE is negative, forcing atoms to move towards high electric field regions. This allows confining atoms in the extrema of the optical lattice potential by adjusting the detuning frequency. Such a trapping method is very versatile because not only it allows controlling atom location while cooling, but also mimicking crystal structures analogous to solid crystals. This opens wide opportunities for simulation of various condensed matter phenomena on a lattice.

2.2.3 Cooling mechanisms

Cooling a gas of atoms by avoiding transition to a solid required new unconventional approaches. Ways to keep the mean separation of atoms larger than the radius of inter-atomic interactions while cooling the gas down was a considerable experimental challenge. Standard cooling process by the first half of twentieth century involved the use of a refrigerator to cool down a vessel holding the probe that needs to be cooled [51]. Techniques developed for cooling gases using electromagnetic waves allowed to achieve considerably lower temperatures (for a more detailed review of the field and its history please consult for instance [52–56]). Such techniques require manipulation at the atomic scale.

Doppler cooling. Atoms can absorb electromagnetic waves. The absorbed energy drives the atom into an excited state determined by a change of internal degrees of freedom such as electron configurations. The absorption happens in quanta of energy E_{R} which has to match the energy required to excite the atom, for instance by exciting an electron to a vacant orbital state. For a stationary atom only electromagnetic waves with the frequency $\omega_{\mathrm{R}} = E_{\mathrm{R}}/\hbar$ within the resonance width can be absorbed. For example, the valence electrons of Na and Rb atoms can be excited using laser beams of wavelengths of 589nm and 780nm respectively (see, for instance, Table A.1

in [50]). Atoms, especially before cooling, are constantly in motion. This leads to a shift in the frequency of light that atoms experience, a Doppler shift. The Doppler shift in frequency $\delta\omega_R$ depends on the speed the atoms move with. Consider for simplicity a one-dimensional system as illustrated in Fig. 2.8, and let the laser beam have a frequency slightly detuned below the resonance frequency of the atoms. Atoms moving against the laser beam absorb light of frequency $\omega_R^{'} = \omega_R - \delta\omega_{\text{Doppler}} = \omega_{\text{laser}}$, and hence are in resonance with the detuned laser. Atoms moving in the direction of the laser beam have their resonance frequency shifted to $\omega_R^{'} = \omega_R + \delta\omega_{\text{Doppler}}$, and so are off resonance with the detuned laser. Consequently only atoms moving against the laser beam absorb light. With the absorption of photons atoms also acquire photons' momenta which leads to a change of the initial momenta of the atoms. If an atom absorbs a particle of light moving towards it then the atom slows down. A slow down of the atoms translates to a decrease in its kinetic energy, and consequently in the temperature of the whole ensemble. This idea can be generalised to all three dimensions by shining laser light from various direction to confine all three degrees of movement of atoms. So far, however, we neglected one important thing: after photons are absorbed atoms are driven to an energetically excited state which leads to spontaneous emission of photons. However, the photons that are spontaneously emitted have a random direction, so on average spontaneous emission does not lead to a change of momenta of the moving atoms. The effect of the spontaneous emission becomes relevant when the heating due to spontaneous emission equilibrates with the laser cooling. This sets up a limit on the temperature that can be achieved using Doppler cooling around 100μK, the so called Doppler limit. Ways to overcome the Doppler limit have been found. An important cooling technique which allows achieving temperatures of the order of nK is evaporative cooling.

Evaporative cooling relies on the idea of releasing the excess of heating in the atomic gas by releasing the most energetic atoms. This can be achieved by shining radio-frequency radiation on atoms, which after absorbing the radiation flip the spin and become high-field seeking. After switching from low-field to high-field seeking atoms that have enough energy escape

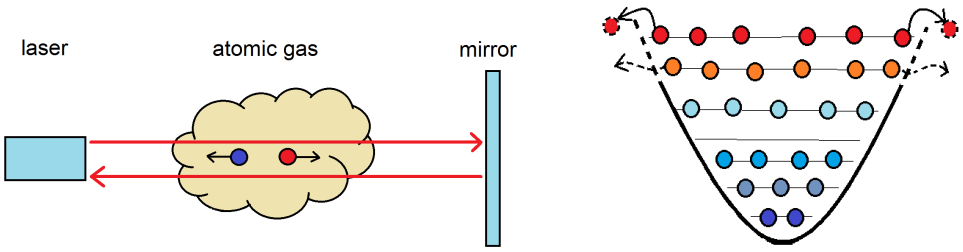

Figure 2.8: Schematic illustration of Doppler (left) and evaporative (right) cooling mechanisms. Left: laser light slows down atoms illustrated in blue, while the reflected light slows down atoms illustrated in red using Doppler effect. Right: high energetic atoms escape the gas once confining potential was lowered (from the dashed line to the solid line). The dashed line illustrates the opening of a channel of energy drainage in the trapping potential. Both pictures are just schematic illustrations and are skipping important details. Its main purpose is delivering the major idea of the cooling process.

the magnetic trap. This way the 'hottest' atoms are released. The remaining atomic ensemble on the way to reaching a new thermal equilibrium acquires a lower temperature. Evaporative cooling is usually the final cooling stage. It allows reaching critical temperatures for Bose-Einstein condensation. Although evaporative cooling allows reaching very low temperatures its drawback is the loss of particles in the process. Consequently it relies on sufficiently high atom density as well as short thermalisation time inside the trap.

2.2.4 Spinor condensates

Spinor condensates play an important role in this thesis. We use spinor condensates to investigate the quenched dynamics of two-dimensional boson lattice systems in Chapter 4, and to investigate the effect of the confining harmonic potential on the topological manifestation of edge-states in Chapter 5. The origin of spin-dependent interactions in atomic gases and the concept of spinor condensates we briefly introduce below. A more detailed review can be found in [56, 57].

If atoms have magnetic moments and can be manipulated using electromagnetic fields, one can also ask whether atoms can have spin-dependent interactions. In experiment with ultra-cold atoms such interactions can be

achieved effectively through the scattering process of a mixture of different hyperfine states. Let us consider a scattering process of two boson states. This is described by introducing a two-body interaction potential $U(\mathbf{r}_1-\mathbf{r}_2)$, which depends on the relative position of the two scattering atoms $\mathbf{r}_1-\mathbf{r}_2$ and on spin degrees of freedom. Assuming that the spatial and spin degrees of freedom are separated, one can make use of the interaction properties to guess the form of the interaction potential. The atomic scattering is usually a local process, i.e. it happens in the same point in space, and one can consider the spatial dependence of the interaction potential to be $\sim \delta(\mathbf{r}_1-\mathbf{r}_2)$. Assuming spin-rotational invariance, the suitable basis to describe the spin degrees is the one of the hyperfine multiplet with total angular momentum $\mathcal{F}$, which for bosons in hyperfine level S is an even number between 0 and $2S$. For atoms of spin $S=1$, which are relevant to the current thesis, two identical boson atoms can couple in an s-states with $\mathcal{F}=0$ and $\mathcal{F}=2$ only, since the wave function of $\mathcal{F}=1$ cannot be symmetric. Denoting by $\mathcal{P}_\mathcal{F}$ the projection operator into states with total angular momentum $\mathcal{F}$, one can write

$$U(\mathbf{r}_1-\mathbf{r}_2)=\delta(\mathbf{r}_1-\mathbf{r}_2)(U_0\mathcal{P}_0+U_2\mathcal{P}_2), \tag{2.35}$$

where $U_\mathcal{F}=4\pi\hbar a^{(\mathcal{F})}/m$ are expressed in terms of the corresponding s-wave scattering lengths $a^{(\mathcal{F})}$ and atom mass m. The projection operators can be expressed in terms of the atom angular momentum operators $\mathbf{S}_1$ and $\mathbf{S}_2$: $\mathcal{P}_0=(1-\mathbf{S}_1\cdot\mathbf{S}_2)/3$ and $\mathcal{P}_2=(2+\mathbf{S}_1\cdot\mathbf{S}_2)/3$. The interaction potential (2.39) is then reduced to

$$U(\mathbf{r}_1-\mathbf{r}_2)=\delta(\mathbf{r}_0-\mathbf{r}_2)(c_0+c_2\mathbf{S}_1\cdot\mathbf{S}_2), \tag{2.36}$$

where

$$c_0=\frac{4\pi\hbar}{m}\left(\frac{2a^{(2)}+a^{(0)}}{3}\right) \text{ and } c_2=\frac{4\pi\hbar}{m}\left(\frac{a^{(2)}-a^{(0)}}{3}\right). \tag{2.37}$$

Introducing annihilation and creation operators, $\hat{\Psi}_{\mathbf{r},\alpha}$ and $\hat{\Psi}^\dagger_{\mathbf{r},\alpha}$, for bosons in spin state α, one can write the Hamiltonian term corresponding to the spin

interaction potential in second quantised form:

$$\hat{\mathcal{H}}_S = \int d\mathbf{r} \left(\frac{c_0}{2} \hat{\Psi}^\dagger_\alpha \hat{\Psi}^\dagger_{\alpha'} \hat{\Psi}_{\alpha'} \hat{\Psi}_\alpha + \frac{c_2}{2} \hat{\Psi}^\dagger_\alpha \hat{\Psi}^\dagger_{\alpha'} \mathbf{S}_{\alpha\beta} \cdot \mathbf{S}_{\alpha'\beta'} \hat{\Psi}_{\beta'} \hat{\Psi}_\beta \right), \tag{2.38}$$

where summation is implied in repeating indexes and $\mathbf{S} = (S_x, S_y, S_z)$ denote the 3×3 spin-one matrices:

$$S_x = \frac{1}{\sqrt{2}} \begin{pmatrix} 0 & 1 & 0 \\ 1 & 0 & 1 \\ 0 & 1 & 0 \end{pmatrix}, \quad S_y = \frac{i}{\sqrt{2}} \begin{pmatrix} 0 & -1 & 0 \\ 1 & 0 & -1 \\ 0 & 1 & 0 \end{pmatrix}, \quad S_z = \begin{pmatrix} 1 & 0 & 0 \\ 0 & 0 & 0 \\ 0 & 0 & -1 \end{pmatrix}.$$

Similar expressions to (2.38) can be obtained for higher spins. For further details we refer to the literature. The current thesis relies on (2.38) and we will make use of the spin-interaction term in next chapters.

Both Zeeman and spin interactions affect the ground state of boson system. Let us briefly describe how the interplay between the Zeeman and spin interaction terms determine the ground state. The total effective Hamiltonian for a system of spin $S = 1$ boson atoms is:

$$\hat{\mathcal{H}} = \hat{\mathcal{K}} + \hat{\mathcal{V}}_{\text{ext}} + \hat{\mathcal{H}}_Z + \hat{\mathcal{H}}_S, \tag{2.39}$$

where $\hat{\mathcal{H}}_Z$ and $\hat{\mathcal{H}}_S$ are the Zeeman and spin-interaction terms introduced earlier, $\hat{\mathcal{V}}_{\text{ext}}$ accounts for the confining potential and $\hat{\mathcal{K}}$ stands for kinetic term. Usually $\hat{\mathcal{K}}$ is related to $-\hbar^2\nabla^2/2m$. However, in presence of an optical lattice one can come to an effective kinetic term that reflects the hoping on the lattice sites. We will use this in our next chapters.

If c_2 is positive (negative), the ground state will be the state that minimises (maximises) the expectation value of $\hat{\mathbf{S}}^2$, and corresponds to a polar or antiferromagnetic (ferromagnetic) state.

2.2.5 Synthetic gauge fields

While optical lattice experiments with ultracold atoms are used to model various condensed matter phenomena, in order to model phenomena related

to topological band insulators one has to be able to mimic for instance the local magnetic fluxes we required for the Haldane model in this chapter. This can be achieved using synthetic, also referred to artificial, gauge fields. The idea it to manipulate atoms trapped in experiments in a way that these would behave similar to charged particles with a local gauge field. The benefit of inducing such synthetic (artificial) gauge fields is not restricted to only modelling topological band insulators, but also induce non-commutative gauge algebra [58], engineer exotic topological phases and artificial dimensions [59, 60].

Although there are many proposals on how to engineer artificial gauge fields (for a review see [61, 62]) we will give a brief comment on the most known ones, and will restrict ourselves to the use of the time-periodic manipulation with optical lattices used to induce gauge fields, which is closely related to the engineering of the honeycomb lattice model frequently used in this thesis.

Probably one of the best known ways of inducing synthetic gauge fields is via rotating the atomic gas [44, 61–63]. To understand the effect one has to remember that a rotating frame with angular velocity $\mathbf{\Omega}$ makes particles of mass M and moving with velocity $\mathbf{v}$ with respect to the rotating system experience a Coriolis force $\mathbf{F}_{\mathrm{C}} = -2M(\mathbf{\Omega} \times \mathbf{v})$. This force is analogous to the Lorenz force $\mathbf{F}_{\mathrm{L}} = -q\mathbf{B} \times \mathbf{v}$ that exerts on a charged particle with charge q moving in an external magnetic field $\mathbf{B}$. This leads to an effective electromagnetic gauge field that has to be added to the single particle momentum operator: $\mathbf{p} \to \mathbf{p} - M\mathbf{\Omega} \times \mathbf{r}$. To be more accurate, consider a gas trapped in a harmonic potential $V_\omega = M\omega^2\mathbf{r}^2/2$. In the frame co-rotating with the system the gas is described by the single-particle Hamiltonian:

$$\mathcal{H}_{\mathbf{\Omega}} = \int d\mathbf{r} \left(\frac{1}{2M} |\mathbf{p}\Psi|^2 + \frac{M\omega^2\mathbf{r}^2}{2} |\Psi|^2 + M\Psi^\dagger \mathbf{\Omega} \cdot (\mathbf{p} \times \mathbf{r})\Psi \right) + \mathcal{H}_{\mathrm{int}}, \tag{2.40}$$

where we have grouped the interaction terms in $\mathcal{H}_{\mathrm{int}}$. The terms inside the

integral can be regrouped to give:

$$\mathcal{H}_{\mathbf{\Omega}} = \int d\mathbf{r} \ \left(\frac{1}{2M} |\left(\mathbf{p} - M\mathbf{\Omega} \times \mathbf{r}\right) \Psi|^2 + \frac{M\left(\omega^2 - \Omega^2\right)\mathbf{r^2}}{2} |\Psi|^2 \right) + \mathcal{H}_{\text{int}}. \tag{2.41}$$

In this form one identifies a gauge-like field $\mathbf{A}_{\text{rot}} = M\mathbf{\Omega} \times \mathbf{r}$ artificially induced via rotating the gas of atoms. Moreover, in the limit of $\Omega^2 = \omega^2$ the presence of the harmonic confining potential is completely absorbed into the induced synthetic gauge field $\mathbf{A}_{\text{rot}}$, and the system mimics a charged gas in an external 'magnetic field'.

A more recent approach for simulating topological band insulator in optical lattice experiments is via applying time-periodic perturbation (shaking) [58, 61, 64, 65]. The idea is based on a cyclic evolution due to such periodic driving that leads to an effective description of the system with induced gauge-like potentials. Instead of rotating consider moving the optical lattice with trapped atoms along a cyclic trajectory: $\mathbf{r}_{\text{lattice}}(t)$. This leads to a shift in the lattice wave-vector by an acquired lattice momenta $\mathbf{p}_{\text{lattice}} = M\dot{\mathbf{r}}_{\text{lattice}}$, which appears as a phase-factor in the resulting tight-binding lattice Hamiltonian:

$$\hat{\mathcal{H}}_{\text{shaken}} = \sum_{jj'} e^{i\mathbf{p}_{\text{lattice}} \cdot (\mathbf{r}_j - \mathbf{r}_{j'})} w_{jj'} \hat{a}_j^\dagger \hat{a}_{j'}, \tag{2.42}$$

where $\mathbf{r}_j$ denotes the lattice coordinate of site j, $w_{jj'}$ stand for the tunnelling amplitude from site j' to site j in the absence of shaking, and $\hat{a}_j$ creates a particle at site j. The Hamiltonian operator $\hat{\mathcal{H}}_{\text{shaken}}$ has time-dependent parameters. However, for a slow time-periodic modulation over a period T, one has a small parameter $\omega = 2\pi/T$ to expand the Hamiltonian $\hat{\mathcal{H}}_{\text{shaken}}$ in terms of non-modulated, i.e. stationary, components. The advantage over the rotating-frame modulation is that the lattice symmetry can be preserved. This led to the engineering of lattice models such as the Haldane model [15, 64], and Harper-Hofstadter model [30, 31, 66]. We will assume the experimental availability of these models, and focus on the investigating condensed matter related phenomena in the rest of the thesis.

2.3 Conclusion

In this chapter we introduced the basic concepts of one- and two-dimensional topological insulators, topological edge-state manifestations of several non-interacting models, the atomic trapping and cooling techniques, as well as the basic features of trapped atomic gases. The following chapters, which represent the bulk and the original part of this thesis, rely on the concepts just presented. A more detailed description of the topics described in this chapter does not fall under the main purpose of this work, and we refer the reader for further details to the literature (for instance [41, 42, 44, 56, 61–63]).

3

Edge states of non-interacting lattice models

This thesis is centred around properties and manifestations of the topological edge states in interacting boson lattice models. Prior to considering interactions, however, it is useful to discuss the edge states of non-interacting models. In this chapter we derive exact analytical expressions of the edge states of the Su-Schrieffer-Heeger (SSH), Haldane, Kane-Mele and Harper-Hofstadter (at $2\pi/3$ magnetic flux per plaquette) models. To our knowledge the exact analytical expressions for the edge states of these models (except for the SSH model) have not been previously derived in the literature, and we regard our finding as part of the original work of the current thesis.

Various analytical methods have been developed to investigate topological edge states in lattice models. These methods usually rely on open boundary conditions (hard wall), or a domain wall which delimits lattices of different topological band structure. These include, but are not limited to, long-wave approximation, transfer matrix method [67], Green's function approach [68]

and generating function method [69, 70]. A good review of various techniques is given in [71]. The long-wave expansion is already an approximation, but can give some important edge-state features like chirality. Transfer matrix method comes from electromagnetic wave-guide theory, and allows one to find edge states as eigenstates of a transfer matrix. The amplitude of the edge states decreases from the edge into the bulk, and is determined by what we will refer to as decaying exponents. These exponents can be found numerically, for instance, within the framework of the transfer matrix approximation. Finding analytical expressions of edge states, however, can generally give more information of the edge states. As it will be explained in Chapter 4 a topological lattice system driven out of equilibrium can lead to unstable edge modes. This instability will manifest itself in the emergence of complex eigenvalue spectra of the edge modes. Knowing analytical expressions of edge states, in this case, can give information about the stability of eigen modes, and how the localisation properties change with the change of parameters in the system. Below we will describe a generating function method. Its remarkable feature, as it will soon become clear, is that for lattices with a small number of sublattice sites in the unit cell this method often gives a simpler way of finding decaying exponents analytically.

3.1 Generating function method (general idea)

We start with the non-interacting Hamiltonian describing particles moving from one site to another on a lattice:

$$\hat{\mathcal{H}}_{\text{lattice}} = \sum_{j,j'} \hat{\psi}_j^\dagger \mathcal{H}_{\text{lattice}}^{j,j'} \hat{\psi}_{j'},$$

where j labels the unit cell, $\hat{\psi}_j = (\hat{\psi}_{jA_1}, \hat{\psi}_{jA_2}, ..., \hat{\psi}_{jA_s})^{\text{T}}$ is a vector of annihilation operators at each sublattice A_1,... A_s, while $\mathcal{H}_{\text{lattice}}$ denotes the Hamiltonian matrix. A lattice is described by its primitive vectors. For matters of convenience let us pick up an arbitrary primitive lattice vector and align our x-axis along it. We now relabel the unit-cells along the x-axis by l. Often it is enough to keep only terms corresponding to hoppings up to the

nearest neighbour unit-cells. In this case the lattice Hamiltonian matrix can be written in the form:

$$\mathcal{H}^{l,l'}_{\text{lattice}} = \tilde{V}_l \delta_{l,l'+1} + V_l \delta_{l,l'-1} + R_l \delta_{l,l'},$$

where V_l, $\tilde{V}_l$, and R_l are matrices acting in the sublattice space. Diagonalisation of the above Hamiltonian is equivalent to solving an eigenvalue equation:

$$\tilde{V}_l \phi_{l+1} + V_l \phi_{l-1} + R_l \phi_l = E \phi_l, \tag{3.1}$$

where E and ϕ_l are the energies and eigenvectors correspondingly. The models of our main interest in our work have R, V and $\tilde{V}$ independent on l, and $\tilde{V} = V^\dagger$. This is the case for homogeneous lattices without dissipation. Under these conditions, for an infinite system or a system with periodic boundary conditions, a suitable basis for diagonalisation of $\mathcal{H}^{l,l'}_{\text{lattice}}$ is obtained by Fourier transform along the primitive vectors. This corresponds to single particle states extended in the bulk. With the introduction of hard-wall boundaries, which we will often refer to as open boundary conditions, localized states at the edge can appear. These excitations cannot be obtained by means of a Fourier transform since these states are not extended, and other computational methods have to be developed. For a small number of sublattice sites in a unit-cell the *Generating Function Approach (GFA)*, which we introduce bellow, can be very useful in finding analytical expressions of the edge states. This approach has previously been used in describing topological edge states in the Shockley model [69], as well as in topological models with five Chern bands [70].

A hard wall boundary at $l \leq 0$ of a semi-infinite lattice system is introduced by an open boundary condition at $l = 0$:

$$V^\dagger \phi_1 + R \phi_0 = E \phi_0. \tag{3.2}$$

To solve the equations (3.1) and (3.2) we next introduce a generating function

$$G(z) = \sum_{l=0}^{+\infty} z^l \phi_l, \tag{3.3}$$

where z is some complex variable. The eigenvectors ϕ_l can be extracted from $G(z)$: $\phi_l = \partial_z^l G(z)|_{z=0}/l!$. The eigenvalue problem for ϕ_l translates onto an equation for the generating function:

$$\left[V^\dagger + z(R-E) + z^2 V\right] G(z) = V^\dagger \phi_0. \tag{3.4}$$

This can be formally solved to give:

$$G(z) = \left[V^\dagger + z(R-E) + z^2 V\right]^{-1} V^\dagger \phi_0. \tag{3.5}$$

Now, $G(z)$ has poles $z = z_\alpha$, where α ranges from one to twice the dimension of the matrix R. $G(z)$ can be written in a form that makes the pole structure apparent:

$$G(z) = g(z)\Pi_\alpha (z - z^\alpha)^{-1}, \tag{3.6}$$

where $g(z)$ is a polynomial in z, and z_α satisfy

$$Q(z) \stackrel{\text{def}}{=} \det\left(V^\dagger + z_\alpha(R-E) + z_\alpha^2 V\right) = 0. \tag{3.7}$$

For the Haldane model, for instance, V, $V^\dagger$ and R are 2×2-matrices and equation (3.7) admits four solutions z_α. For extended states these are just plane waves. However, for edge states the z_α determine how fast the states decay into the bulk. This can be seen by noticing that $1/(z - z_\alpha) = -\sum_{n=0}^{+\infty} z^n / z_\alpha^{n+1}$ for $|z_\alpha| > 1$ in (3.7). It can be shown that for each z_α there is a z_β satisfying (3.7), but which is related to z_α by $|z_\alpha z_\beta| = 1$. This corresponds to growing into the bulk states, which have to be excluded. The only way to do this is to have ϕ_1 cancel the undesirable poles in (3.5). As it will be shown in the examples below the remarkable advantage of Generating Function Method is that one can find the eigenvalues for energy dispersion E without solving equation (3.7).

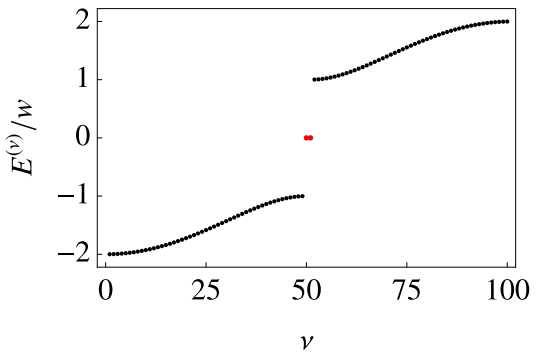

Figure 3.1: The energy spectrum of the Su-Schrieffer-Heeger model for $\delta w = w/2$, $\mu = 0$ and 100 sites. Here ν labels the eigenstates. The zero energy values $E^{(\text{edge})} = 0$ that are shown in red belong to the edge states.

We now apply the generating function approach to find analytical expressions for topological edge states of the Su-Schrieffer-Heeger (SSH), Haldane, and Harper-Hofstadter models. The most relevant to this thesis is the Haldane model. However it is useful to start with considering a one-dimensional SSH model before introducing more complicated two-dimensional ones.

3.2 Su-Schrieffer-Heeger (SSH) Model

The Su-Schrieffer-Heeger model has been already introduced in the previous chapter so we start from the SSH Hamiltonian in terms of sublattice index A and B straight away:

$$\hat{\mathcal{H}}_{\text{SSH}} = -\sum_{l}(w_{-}\hat{a}^{\dagger}_{Al}\hat{a}_{Bl} + w_{+}\hat{a}^{\dagger}_{Al+1}\hat{a}_{Bl} + h.c.) - \mu a^{\dagger}_{Al}\hat{a}_{Al} - \mu a^{\dagger}_{Bl}\hat{a}_{Bl}, \quad (3.8)$$

where l labels the sites in the A (B)- sublattice and $w_{\pm} = w \pm \delta w$. We consider an infinite system with a left edge, so $l \geq 0$. The model is identical to the Shockely model, which was already investigated using the generating function method in [69]. The energy spectrum consists of two bulk bands and zero-energy points belonging to edge states once the hard-wall boundaries are

implied (Fig. 3.1). We next bring the Hamiltonian (3.8) to the form:

$$\hat{\mathcal{H}} = \sum_l \hat{\mathbf{a}}_l^\dagger \left[V^\dagger \hat{\mathbf{a}}_{l+1} + V \hat{\mathbf{a}}_{l-1} + R \hat{\mathbf{a}}_l \right], \tag{3.9}$$

with $\hat{\mathbf{a}}_l = (\hat{a}_{Al}, \hat{a}_{Bl})^{\mathrm{T}}$, and the corresponding matrices

$$V = -w_+ \begin{pmatrix} 0 & 1 \\ 0 & 0 \end{pmatrix}, R = \begin{pmatrix} -\mu & -w_- \\ -w_- & -\mu \end{pmatrix}.$$

Diagonalizing the Hamiltonian translates to solving the corresponding Schrödinger equation

$$V^\dagger \phi_{l+1} + V \phi_{l-1} + R \phi_l = E \phi_l \tag{3.10}$$

for $l > 1$ with an open boundary condition at $l = 0$:

$$V^\dagger \phi_1 + R \phi_0 = E \phi_0. \tag{3.11}$$

Here ϕ_l have two components, ϕ_l^A and ϕ_l^B, corresponding to the two sublattices. We switch to the generating function representation: $G(z) = \sum_{l=0}^{+\infty} z^l \phi_l$. Following (3.5) one finds

$$G(z) = \frac{-\phi_1^A w_+}{z(E+\mu)^2 - (w_- + z w_+)(w_+ + z w_-)} \begin{pmatrix} w_- + w_+ z \\ (E+\mu) z \end{pmatrix}. \tag{3.12}$$

The denominator of (3.12) has two poles:

$$z_{1(2)} = \frac{(E+\mu)^2 - w_-^2 - w_+^2 \pm \sqrt{\left((E+\mu)^2 - w_-^2 - w_+^2\right)^2 - 4 w_+^2 w_-^2}}{2 w_- w_+}. \tag{3.13}$$

Notice that these poles satisfy $|z_1 z_2| = 1$. This conclusion could also be reached by applying Vieta's theorem (see Appendix B), rather than solving the equation for the zeros of the denominator in (3.12). For the edge states to be decaying, only $|z_\alpha| > 1$ is allowed, and hence the other pole has to cancel. This can happen only when the energy of the edge state E is equal

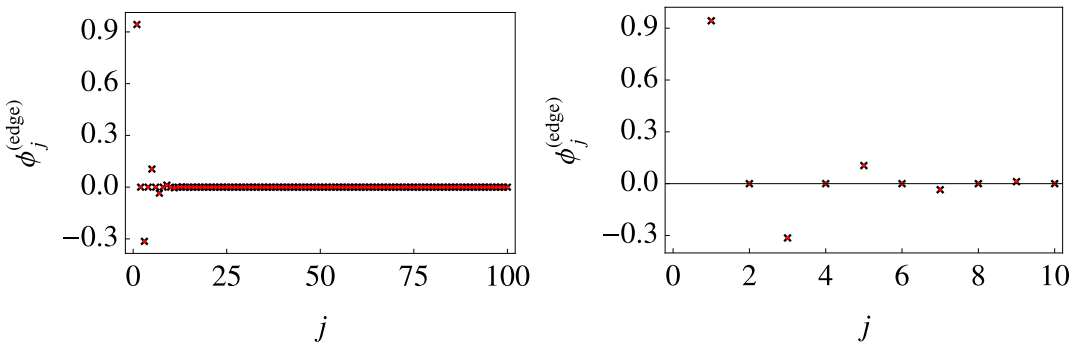

Figure 3.2: The eigenvector ϕ_j of Su-Schrieffer-Heeger Hamiltonian for $\delta w = w/2$ vs site label j. The right figure shows a zoomed in picture of the left one. The red points correspond to edge states found numerically by exact diagonalisation of the Hamiltonian matrix, while the crosses denote the analytical expression (3.15). Here the function ϕ_j is normalized to one: $\sum_j \phi_j^* \phi_j = 1$.

to $-\mu$, i.e. it stays in the middle of the gap, as can be noticed from (3.12). The generating function in this case reduces to:

$$G(z) = \frac{\phi_1^A w_+/w_-}{z - z_0} \begin{pmatrix} 1 \\ 0 \end{pmatrix}, \tag{3.14}$$

where the only pole that survives $z_0 = -w_+/w_-$ has to be by its absolute value greater than 1 for the series $\{\phi_l = \partial_z^l G(z)|_{z=0}/l!\}_{l\geq 1}$ to converge:

$$\phi_l = \phi_1^A \left(1 + \frac{1}{z_0} + \frac{1}{z_0^2} + \frac{1}{z_0^3} + ...\right) \begin{pmatrix} 1 \\ 0 \end{pmatrix}. \tag{3.15}$$

This condition of the existence of the edge states is exactly the condition of ensuring non-trivial topology $|w_-/w_+| < 1$, which reflects the bulk-boundary correspondence of the Su-Schrieffer-Heeger model.

3.3 Haldane Model

Finding analytical expressions for the edge states in two-dimensional models can be considerably more complicated. The generating function of two-dimensional models can have more poles which require careful treatment. Below we use the generating function approach to find the edge states of the

non-interacting Haldane model. The results of this discussion will be used in the next chapters of this thesis. We skip the introduction of the Haldane model since it was given in the previous chapter. In what follows we consider an infinite lattice with lattice primitive vectors $\mathbf{a}_1$ and $\mathbf{a}_2$. Let k be the wave vector along $\mathbf{a}_2$, and $l \geq 0$ label the unit-cells along $\mathbf{a}_1$. Furthermore, we consider a single open boundary at $l = 0$ at the site belonging to the A-sublattice. One could also consider an open boundary in the $\mathbf{a}_2$ direction. The solution described below is applicable in this case too. Because of the periodicity along $\mathbf{a}_2$ the Schrödinger equation (3.1) has k-dependent coefficients V_k and R_k:

$$V_k \phi_{l+1,k} + V_k^\dagger \phi_{l-1,k} + R_k \phi_{l,k} = E_k \phi_{l,k} \tag{3.16}$$

for $l > 1$, and

$$R_k \phi_{0,k} + V_k \phi_{1,k} = E_k \phi_{0,k} \tag{3.17}$$

reflects the open boundary condition at site $l = 0$. For the Haldane model one has:

$$R_k = \begin{pmatrix} 2\lambda \cos(k + \varphi) & -w(1 + e^{-ik}) \\ -w(1 + e^{ik}) & 2\lambda \sin(k - \varphi) \end{pmatrix} \tag{3.18}$$

and

$$V_k = \begin{pmatrix} 2\lambda e^{-ik/2} \cos(k/2 - \varphi) & -w \\ 0 & 2\lambda e^{-ik/2} \cos(k/2 + \varphi) \end{pmatrix}. \tag{3.19}$$

The generating function $G(z) = \sum_{l=0}^{+\infty} z^l \phi_l$ has generally four poles which obey equation (3.7). This equation is a fourth order polynomial in z, and admits analytical solution. However, finding the poles and furthermore analysing them is a complicated task. Instead of doing so we remind ourselves that only half of the roots will be suitable for the edge states since the other half correspond to growing instead of decaying states. Therefore two poles have to naturally cancel from both the numerator and the denominator of $G(z)$. We can represent each component of $G(z)$ as a ratio of two

polynomials:

$$G(z) = \frac{1}{Q(z)} \begin{pmatrix} a_1 z^2 + b_1 z + c_1 \\ a_2 z^2 + b_2 z + c_2 \end{pmatrix}, \tag{3.20}$$

where $a_{1(2)}$, $b_{1(2)}$ and $c_{1(2)}$ are complex coefficient which depend on the energy E, wave-vector k and the boundary vector ϕ_0. Since both roots of the numerator have to cancel, instead of finding the zeros of the denominator one can require the polynomials sitting in the numerator to have the same roots:

$$\frac{a_1}{a_2} = \frac{b_1}{b_2} = \frac{c_1}{c_2}. \tag{3.21}$$

The above relation can be solved to give ϕ_0:

$$V^\dagger \phi_0 = \phi_0^{(A)} \begin{pmatrix} 1 \\ e^{ik/2}\xi \end{pmatrix}, \tag{3.22}$$

and the edge-state energy:

$$\begin{aligned} E_{\text{edge}}(\mathbf{k}) = 2 \big[& w^2 \xi \cos(k/2) + \lambda \big(w(1 - \xi^2 + \cos k) \cos\varphi - w(1 + 2\xi^2) \sin k \sin\varphi \\ & -2\lambda\xi \sin(3k/2) \sin(2k)) \big] / \left[\xi (w\xi - 4\lambda \sin(k/2) \sin\varphi) \right], \end{aligned} \tag{3.23}$$

where

$$\xi = -\frac{w \pm \sqrt{w^2 - 8\lambda^2(\cos k + \cos(2\varphi))}}{4\lambda \cos(k/2 - \varphi)}. \tag{3.24}$$

The sign $\pm$ corresponds to the two edge eigenvector solutions, only one of which is decaying into the bulk. For a lattice geometry with two boundaries, the growing solution would correspond to a decaying edge state at the other boundary. For $\varphi = \pi/2$ the expression for the edge-state energy dispersion considerably simplifies:

$$E_{\text{edge}}(\mathbf{k}) = -\mu \pm \frac{6\lambda \sin k}{\sqrt{w^2 + 16\lambda^2 \sin^2(k/2)}}. \tag{3.25}$$

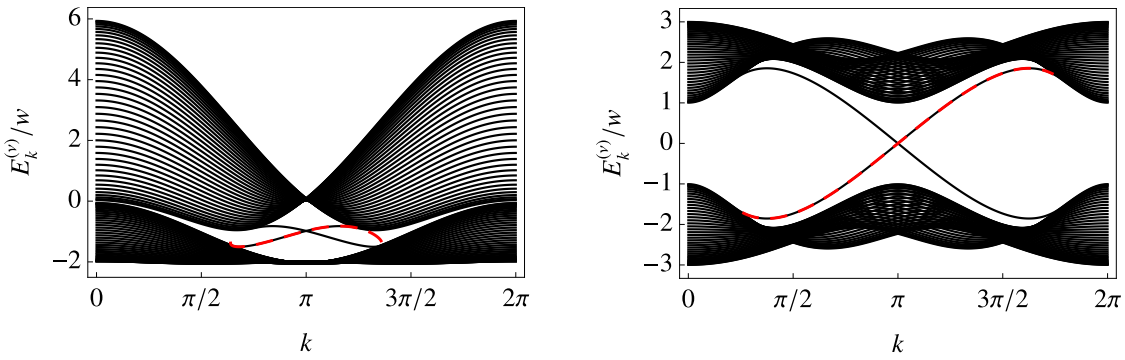

Figure 3.3: Energy spectrum of the Haldane model for $\varphi = \pi/16$ (left) and $\varphi = \pi/2$ (right), and $\lambda = w/2$. The black lines correspond to data obtained numerically by exact diagonalisation of the Hamiltonian matrix. Dashed red lines, which go on top of the black ones, correspond to the analytical expression (3.23). The overlap of dashed red lines with the black ones indicates a very good agreement of the analytical result with the numerical one.

The eigenvectors ϕ_l are straight-forwardly obtained from the generating function $\phi_l = \partial_z^l G(z)|_{z=0}/l!$ by substituting the expression for E_{edge} into $G(z)$. For $\varphi = \pi/2$ this gives:

$$\phi_l(k) = C_N \left(\frac{1}{z_1^l} - \frac{1}{z_2^l} \right) \phi_0, \tag{3.26}$$

where C_N is a normalization coefficient,

$$\phi_{0,k} = \begin{pmatrix} e^{-ik/2} \left(\sqrt{w^2 + 16\lambda^2 \sin^2(k/2)} + w \right) \\ 4\lambda \sin(k/2) \end{pmatrix}, \tag{3.27}$$

and the edge states decaying coefficients z_1 and z_2 are

$$z_{1,2} = e^{-ik/2} \cos(k/2) \, \frac{(\zeta^2 - 3w^2) \pm 2\sqrt{(\zeta^2 - 3w^2)^2 - 16\lambda^2 \tan^2(k/2))}}{\zeta(\zeta - w)}, \tag{3.28}$$

where $\zeta = \sqrt{w^2 + 16\lambda^2 \sin^2(k/2)}$. The normalization coefficient C_N can be set by the normalization condition $\sum_{l=0}^{+\infty} \phi_l^\dagger \phi_l = 1$.

In Fig. 3.3 we compare the derived analytical result for the edge-state dis-

persion with numerically computed dispersion in the strip geometry. For sufficiently large systems (so that the edge states on opposite sides of the system are decoupled), excellent agreement is found between the results.

3.4 Hofstadter Model

Finding exact analytical expression for the edge states for lattices with more complicated structure such as more than two sublattice sites in the unit-cell can be rather complicated or might not be possible. Here we discuss a very common two-dimensional model on a square lattice which has a more complex sublattice structure, the Harper-Hofstadter model. This model describes particles on a square lattice under the presence of a uniform perpendicular magnetic field. When the magnetic length is much larger than the lattice constant, one finds large degeneracies in the eigenstates (Landau levels). On the other hand, when the magnetic length is comparable to the lattice constant, a much more complex eigenspectrum results, commonly known as the Hofstadter Butterfly [27–31].

We start with the Hamiltonian of the Harper-Hofstadter model:

$$\hat{\mathcal{H}} = -w \sum_j \hat{a}^\dagger_{j+\hat{x}} \hat{a}_j + \hat{a}^\dagger_{j-\hat{x}} \hat{a}_j + e^{-i\gamma x_j} \hat{a}^\dagger_{j+\hat{y}} \hat{a}_j + e^{-i\gamma x_j} \hat{a}^\dagger_{j-\hat{y}} \hat{a}_j, \tag{3.29}$$

where there is a local magnetic flux determined by $\gamma = 2\pi/q$ at each plaquette of the lattice. For an integer q the unit-cell has q sublattice sites. For $q = 2$ the energy spectrum is given by two energy bands, and no gap is present. The biggest flux one can have while having a gap is $\gamma = 2\pi/3$. There are three sites in the unit cell in this case. For the sake of clarity let us focus on the x-axis, introduce a label l of the unit cell along this axis, and group the annihilation operators into a unit-cell vector operator $\hat{\mathbf{a}}_l(k) = (\hat{a}_{l,A}(k), \hat{a}_{l,B}(k), \hat{a}_{l,C}(k))$. Here A, B, C correspond to the tree sublattices, and we introduced the wave-vector k due to the periodicity along the y-axis. The Hamiltonian then

can be written as:

$$\hat{\mathcal{H}} \;=\; \sum_l \hat{\mathbf{a}}^\dagger \left[V^\dagger \hat{\mathbf{a}}_{l+1} + V \hat{\mathbf{a}}_{l-1} + R\ \hat{\mathbf{a}}_l \right], \tag{3.30}$$

where one identifies the 3×3-matrix coefficients:

$$V \;=\; -w \begin{pmatrix} 0 & 0 & 1 \\ 0 & 0 & 0 \\ 0 & 0 & 0 \end{pmatrix}, R = -w \begin{pmatrix} 2\cos k & 1 & 0 \\ 1 & 2\cos\left(k - \frac{2\pi}{3}\right) & 1 \\ 0 & 1 & 2\cos\left(k + \frac{2\pi}{3}\right) \end{pmatrix}.$$

The corresponding generating function (3.5) is readily found:

$$G(z) = \frac{\phi_0^{(A)}}{\left[z^2 - \frac{z_2}{z_1}\left(z_2 + \frac{1}{z_1}\right) z + 1 \right] - 3z\frac{E}{w}\left(1 - \frac{z_2}{z_1}\right)} \begin{pmatrix} -\frac{1}{z_1}(z - z_1) \\ (z - z_2) \\ -\left(1 - \frac{z_2}{z_1}\right) \end{pmatrix}, \tag{3.31}$$

where $z_1 = w/\left(E + 2w\cos\left(k - \frac{2\pi}{3}\right)\right)$ and $z_2 = \left(E + 2w\cos k\right)/w$. The denominator is given by a second order polynomial in z and has two zeroes $z_{p,1}$and $z_{p,2}$. Applying Vieta's relation (see Appendix B) for the denominator one gets that $z_{p,1} \cdot z_{p,2} = 1$. The pole that is smaller than one has to be cancelled in order to exclude the growing solution of the Schrödinger equation. This gives a restriction on the energies E, which results in the dispersion relation for edge modes. A cancellation of the pole is only possible if the third component of $G(z)$ vanishes since it does not depend on z:

$$z_0^{-1} \stackrel{\text{def}}{=} z_2 = z_1 = -\sqrt{3}\sin\left(k - \frac{\pi}{3}\right) \pm \sqrt{1 + 3\sin^2\left(k - \frac{\pi}{3}\right)}. \tag{3.32}$$

This gives the edge-state energy dispersion:

$$E_\pm^{\text{edge}}(k) = -w\cos\left(k - \frac{\pi}{3}\right) \pm w\sqrt{1 + 3\sin^2\left(k - \frac{\pi}{3}\right)}. \tag{3.33}$$

The edge-state dispersion crosses the gap, and connects different bulk energy bands. The points k where the edge energy connects with the bulk band

satisfy the condition $|z_0(k)| = 1$. Altogether with the requirement $|z_0(k)| \geq 1$ one has:

$$z_0^{-1} = \begin{cases} -\sqrt{3}\sin\left(k - \frac{\pi}{3}\right) - \sqrt{1 + 3\sin^2\left(k - \frac{\pi}{3}\right)}, & \text{for } \sin\left(k - \frac{\pi}{3}\right) < 0 \\ -\sqrt{3}\sin\left(k - \frac{\pi}{3}\right) + \sqrt{1 + 3\sin^2\left(k - \frac{\pi}{3}\right)}, & \text{for } \sin\left(k - \frac{\pi}{3}\right) > 0 \end{cases}, \tag{3.34}$$

and

$$E_{\text{edge}}(k) = \begin{cases} -w\cos\left(k - \frac{\pi}{3}\right) - w\sqrt{1 + 3\sin^2\left(k - \frac{\pi}{3}\right)}, & \text{for } \sin\left(k - \frac{\pi}{3}\right) < 0 \\ -w\cos\left(k - \frac{\pi}{3}\right) + w\sqrt{1 + 3\sin^2\left(k - \frac{\pi}{3}\right)}, & \text{for } \sin\left(k - \frac{\pi}{3}\right) > 0 \end{cases}. \tag{3.35}$$

Plugging these results into the generating function $G(z)$ gives

$$G(z) = \frac{\phi_1^{(A)}}{(1 - z/z_0)} \begin{pmatrix} 1 \\ -1/z_0 \\ 0 \end{pmatrix}. \tag{3.36}$$

The third element in (3.36) vanishes due the pole cancellation in (3.31). Although the same occurred to the last element of the generating function for the SSH model (3.14), the elements of the generating functions are generally non-vanishing. An example would be the Haldane model (3.27), which was discussed in the previous section. From the generating function $G(z)$ one immediately restores the eigenvectors $\phi_l = \partial_z^l G(z)|_{z=0}/l!$:

$$\phi_l = \frac{\phi_1^{(A)}}{z_0^l} \begin{pmatrix} 1 \\ -1/z_0 \\ 0 \end{pmatrix}. \tag{3.37}$$

The coefficient $\phi_0^{(A)}$ can be fixed by a normalisation condition. The density $\phi_l^\dagger \phi_l$ decays as $1/|z_0|^l$ at large values of l, i.e. far from the boundary $l = 0$. To be more accurate, $\log \phi_l^\dagger \phi_l = -l \log |z_0|^2 + \log\left(|\phi_0^{(A)}|^2 (1 + |z_0|^{-2})\right)$. Fig. 3.4 (a) shows energy spectrum obtained by exact diagonalisation of the Hamiltonian matrix (black lines). The analytical expression (3.35) is

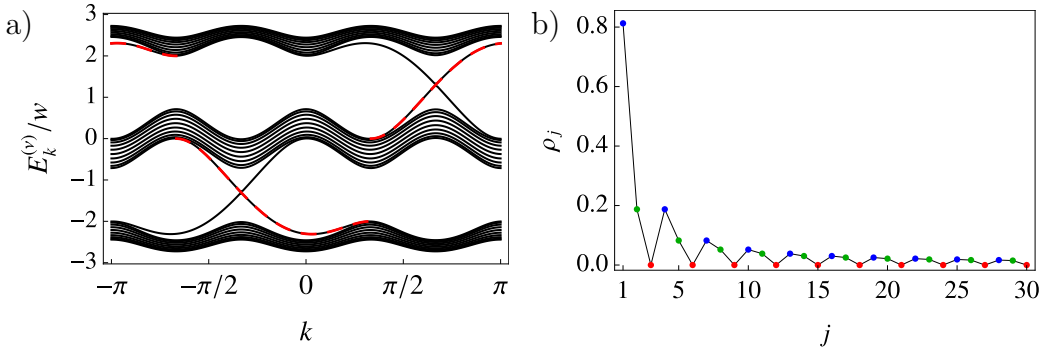

Figure 3.4: Figure (a) shows energy-band structure of the Harper-Hofstadter model with $B = 2\pi\hat{x}/3$. In black are shown the three bulk energy-bands and the edge states connecting them. The red dashed lines, which go on top of the black ones, correspond to the analytical expressions for the edge modes (3.35). Figure (b) shows the density ρ_j of the edge states connecting the lowest two bulk energy bands, and integrated over the wave-vector k from $-2\pi/3$ to $\pi/3$ at each site j. $\phi_0^{(A)}$ has been fixed by requiring $|\phi_0^{(A)}|^2+|\phi_0^{(B)}|^2+|\phi_0^{(C)}|^2 = 1$. Open boundary conditions are imposed at the edge of a chain of 10 unit-cells along the x direction. Blue, green and red points correspond to the three sublattices A, B, and C respectively.

illustrated by dashed red lines shown on top of the black ones. The overlap of the dashed red lines and the black lines illustrates the good agreement of the analytical result with the numerical one.The density ρ_j for the edge states connecting the lowest two bulk energy bands, and integrated over the wave-vector k from $-2\pi/3$ to $\pi/3$ at each site j, are shown in Fig. 3.4 (b). It shows how the edge state is localized at the edge. The blue, green and red points correspond to the three sublattices A, B, and C respectively. The variations in the density within the unit cell that are seen in Fig. 3.4 (b) are due to the sublattices being inequivalent.

3.5 Conclusions and outlook

In this chapter analytical expressions for the edge energies and edge states have been derived for the non-interacting Su-Schrieffer-Heeger (SSH), Haldane, Kane-Mele and Harper-Hofstadter (at $2\pi/3$ magnetic flux per plaquette) models. Although topological edge states can also be investigated numerically, analytical expressions have the advantage of being exact, of capturing the interplay of all the parameters of the model simultaneously, and can be

used in analytical derivation of other quantities. For instance, the exact expression for the energy of the edge states of the Kane-Mele model will allow us to find the edge-state energy dispersion in presence of weak interactions in Chapter 4. It will also be used in the derivation of time evolution of the particle density and edge spin current in a quenched weakly interacting topological system. It it the analytical expression for the edge states that will allow us to determine a time scale for the spin current to increase exponentially and dominate the time evolution of a quenched system (4.36). Other possible uses of analytical expressions derived in this chapter include the analytical investigation of the emergence of edge states, their characteristic localisation length scale, and finite-size effects. It is also worth mentioning that the edge energy dispersion for solid-state topological insulators is accessible using angle-resolved photoemission spectroscopy (ARPES) [72].

4

Dynamical instability and topological boson dynamics

4.1 Introduction

With the development of laser cooling techniques it became possible to reach cold enough temperatures for bosonic systems to condense in a single state, known as a Bose-Einstein condensate (BEC). This allowed scientists to test quantum phenomena at a macroscopic level and directly observe the particle distributions driven by this quantum phenomena. On the other hand experiments with optical lattices give a remarkable opportunity to model lattice structures with adjustable interaction couplings, making possible testing different quantum models and specific phenomena which is sometimes difficult to analyse in solids. This thesis focuses on the realization of topological phases in ultra-cold atoms in optical lattice experiments. The main interest in topological systems focuses around the edge modes that emerge at the border of two media of different topological phase, or at the side of the material. Topological edge states in electronic systems can have important consequences on the properties of topologically non-trivial systems, lead-

ing to quantum Hall conductivity and the absence of back scattering. The topological properties for bosons are much less investigated, and ultracold atoms offer a remarkable opportunity for the realization of boson topological lattice models. Unlike fermions, bosons do not obey the Pauli exclusion principle, and particles condense in the ground state at zero temperature. This creates additional difficulties in investigating the topological properties for Bose systems as the higher-energy topological edge states remain largely unimportant for the dynamics of the system. In this chapter a scheme that makes the edge-state dynamics of a two-dimensional topological boson system dominant is discussed. At the centre of this scheme lies the idea of dynamical instability [73–77]. This chapter includes some main results of this thesis. It shows how one can make topological edge-states dynamically unstable while preserving dynamical stability of the bulk states in interacting boson 2D optical lattices of ultracold atoms. Such a process requires preparing the system out of equilibrium and a quench mechanism for this is suggested. Prior to moving to two-dimensional lattices, however, the basic concepts of dynamical instability will be introduced, and the main idea of a such mechanism will be illustrated on a one-dimensional chain of the Su-Schrieffer-Heeger (SSH) model. To my knowledge the idea of populating topological boson edge-states in optical lattices with ultra-cold atoms using the dynamical instability mechanism was first suggested in [78]. The edge-states in one-dimensional systems, however, are not chiral and therefore do not exhibit dynamics. Two-dimensional systems are more interesting in this sense, but, being more complex, two-dimensional systems require a different treatment. In particular, it will be shown that a more involved quench mechanism is necessary, and symmetries of the system will play a much more important role than in one-dimensional models.

4.1.1 Dynamical instability

This chapter relies on a concept called the dynamical instability. As it will be explained below, this type of instability can be related to the quantum inverted harmonic oscillator problem. Attempts to diagonalize the Hamiltonian will lead to a complex, as opposed to real, eigenspectrum. As a result,

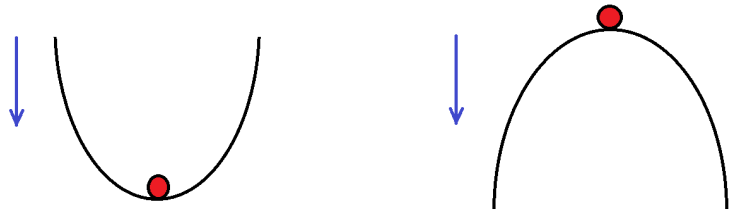

Figure 4.1: Example of stable (left) and unstable (right) equilibrium states. A ball on the bottom (left) is in a stable equilibrium state. A ball on the top of the hill represents an unstable state, since any small deviation from its equilibrium point would drive the ball down the hill without any chance of returning to its initial state. The balls are assumed to be subject to a gravitational force acting in the direction indicated by the arrow.

observables such as particle density attain exponential growth in the time evolution of the system. Let us now explain all the above statements in detail.

Before we introduce the concept of dynamical instability we first remind the reader of two relevant classical examples of stable and unstable equilibrium states (depicted in Fig. 4.1). A ball at the bottom of a hill depicted in the left picture of Fig. 4.1 is in a stable equilibrium state, because any small deviation from this state will bring the ball back to the equilibrium point. This is opposite to a ball on the top of a hill depicted in the right picture of Fig. 4.1. Any small deviation to its position, for instance, due to a sudden blow of wind from a random direction, will irreversibly move the ball outside its equilibrium point. Assuming the ball is point like and setting its mass to 1, the system near the equilibrium position can be approximately described by the Hamiltonian:

$$H = \frac{p^2}{2} \pm \frac{x^2}{2}, \tag{4.1}$$

where p and x are the momentum and the rescaled deviation of the ball from the equilibrium position along the horizontal direction respectively (Fig. 4.1). The $(-)+$ sign corresponds to the (un)stable situation. The stable scenario is known as the harmonic oscillator problem of a particle in a harmonic potential $V_{\mathrm{HO}} = x^2/2$, while the unstable case corresponds to the inverted harmonic oscillator problem determined by the inverted harmonic oscillator

potential $V_{\rm IHO} = -x^2/2$.

We now switch to a quantum mechanical description of the problem of the harmonic oscillator and its inverse counterpart. In quantum mechanics the quantisation condition $[x, p] = i$ is imposed. It is constructive, however, to introduce the annihilation and creation operators:

$$\hat{a} = (x + ip)/\sqrt{2}, \quad \hat{a}^\dagger = (x - ip)/\sqrt{2}. \tag{4.2}$$

In terms of these operators the Hamiltonian of a quantum harmonic oscillator takes the canonically diagonal form:

$$\hat{\mathcal{H}}_{\rm HO} = \hat{a}^\dagger \hat{a} + \frac{1}{2}. \tag{4.3}$$

The energy spectrum of $\hat{\mathcal{H}}_{\rm HO}$ is real, and only certain quantized values of energy are allowed $E = n + 1/2$, where $n \geq 0$ is an integer. Once the sign of the potential is flipped to the inverse one, the Hamiltonian of the inverse quantum harmonic oscillator in terms of the canonical operators (4.2) has a rather different form from $\hat{\mathcal{H}}_{\rm HO}$:

$$\hat{\mathcal{H}}_{\rm IHO} = -(\hat{a}\hat{a} + \hat{a}^\dagger \hat{a}^\dagger)/2. \tag{4.4}$$

The Hamiltonian $\hat{\mathcal{H}}_{\rm IHO}$ cannot be brought to a canonically diagonal form such as (4.3). Rather than having particles localized in an excited state $|n\rangle$, the system prefers moving them around from $|n\rangle$ to $|n-2\rangle$ and vice versa. This is how the instability of the inverse harmonic quantum oscillator looks in the second quantization terminology. The terms in (4.4) are called pairing terms, and naturally appear in Bogoliubov–de Gennes Hamiltonians for the excitations of the Bose-Einstein condensates. However many of these systems do not exhibit dynamical instabilities. To clarify this let us consider the simplest form of the Bogoliubov–de Gennes Hamiltonian:

$$\hat{\mathcal{H}}_{\rm BdG} = w\hat{a}^\dagger \hat{a} + g(\hat{a}\hat{a} + \hat{a}^\dagger \hat{a}^\dagger)/2. \tag{4.5}$$

Two competing terms can be identified in $\hat{\mathcal{H}}_{\rm BdG}$: a term that partly resembles the quantum harmonic oscillator (its strength is determined by w), and

a pairing term of strength g which for $g < 0$ reduces to the inverse harmonic oscillator Hamiltonian (4.4). The Hamiltonian (4.5) can be brought to canonically diagonal form $\hat{\mathcal{H}}_{\rm BdG} = E\hat{b}^\dagger\hat{b}$ using the Bogoliubov transformation:

$$\hat{a} = u\hat{b} - v^*\hat{b}^\dagger, \quad \hat{a}^\dagger = -v\hat{b} + u^*\hat{b}^\dagger, \tag{4.6}$$

where $|u|^2 - |v|^2 = 1$ in order to preserve the canonical commutation relations $[\hat{b}, \hat{b}^\dagger] = [\hat{a}, \hat{a}^\dagger] = 1$. The quasiparticle eigen-energy values are $E = \sqrt{w^2 - g^2}$. For a weakly interacting system, $w^2 - g^2 > 0$, the Bogoliubov transformation is always validated to diagonalize the Bogoliubov–de Gennes Hamiltonian. However for $w^2 - g^2 < 0$ the pairing terms are dominant, the transformation (4.6) does not preserve the canonical commutation relation $[\hat{b}, \hat{b}^\dagger] \neq 1$, and the Hamiltonian cannot be brought to canonically diagonal form. This can happen, for instance, for dissipational processes with w acquiring imaginary part such as in experiments with photon crystals. It can also happen when the system is abruptly driven out of equilibrium in a way that changes the sign of $w^2 - g^2$. In these cases we will refer to the system to be driven to a dynamically unstable phase. The emergence of complex, as opposed to real, values in the Bogoliubov energy spectrum in this sense signifies the emergence of a dynamical instability. As it will be shown below, dynamically unstable states lead to exponentially growing in time correlation functions.

To see the effect of dynamical instability on the dynamics of the system let us consider the Heisenberg equations of motion:

$$i\partial_t\hat{a}(t) = [\hat{a}(t), \hat{\mathcal{H}}], \tag{4.7}$$

where we have set $\hbar = 1$. The explicit form of $\hat{a}(t)$ can be found for instance by applying the Baker-Campbell-Hausdorff relation to $\hat{a}(t) = e^{i\hat{\mathcal{H}}t}\hat{a}e^{-i\hat{\mathcal{H}}t}$ or searching for a solution as a linear combination of creation and annihilation operators with time-dependent coefficients:

$$\hat{a}(t) = A(t)\hat{a} + B(t)\hat{a}^\dagger. \tag{4.8}$$

The coefficients $A(t)$ and $B(t)$ are subject to the initial conditions in that

$\hat{a}(t=0) = \hat{a}$, which requires $A(0) = 1$ and $B(0) = 0$. These coefficients consequently can be found to be:

$$A(t) = \cos(Et) - iw\frac{\sin(Et)}{E},$$
$$B(t) = -ig\frac{\sin(Et)}{E},$$

with the Bogoliubov energy

$$E = \sqrt{w^2 - g^2}. \tag{4.9}$$

This leads to the density population of the Bogoliubov fluctuations of the ground state $|0\rangle$:

$$\langle 0|\hat{a}^\dagger(t)\hat{a}(t)|0\rangle = \left| g^2 \frac{\sin(Et)^2}{E^2} \right|. \tag{4.10}$$

The above expression shows that the particle density oscillates in time with a frequency determined by the Bogoliubov energies $E = \sqrt{w^2 - g^2}$. However, in certain circumstances, such as a quench in w or g, that drives the system to a phase with $w^2 - g^2 < 0$ the Bogoliubov energies E acquire an imaginary part, and the system becomes dynamically unstable. The consequence on the population density of Bogoliubov excitations (4.10) is that it increases exponentially fast:

$$\langle 0|\hat{a}^\dagger(t)\hat{a}(t)|0\rangle = \frac{g^2}{g^2 - w^2} \sinh^2(\sqrt{g^2 - w^2}\ t) \text{ for } g^2 > w^2. \tag{4.11}$$

In this chapter it will be shown how the idea of dynamical instability can be applied to boson topological lattices, and how one can drive these systems only for the topological edge states to be become dynamically unstable.

4.1.2 Dynamical instability of topological edge states in 1D (Su-Schrieffer-Heeger model)

For one-dimensional systems the idea of populating topological edge states by making them dynamically unstable was introduced for the Su-Schrieffer-Heeger (SSH) model in [78]. The virtue of the one-dimensional systems is that these often can be solved exactly and illustrate important phenomena in a more clear way. The drawback, however, is the absence of rich dynamics as present in higher dimensional systems. Recall the Hamiltonian of the non-interacting SSH model that we introduced in the first chapters of this thesis:

$$\hat{\mathcal{H}}_{\text{SSH}} = -\sum_j (w + (-1)^j \delta w)\hat{a}_j^\dagger \hat{a}_{j-1} + h.c. - \mu a_j^\dagger \hat{a}_j \tag{4.12}$$

where the sum is taken along the chain sites j and μ is the chemical potential.

Next we consider an interaction term to the Hamiltonian above:

$$\hat{\mathcal{H}}_{\text{int}} = \frac{U}{2}\sum_j (\hat{a}_j^\dagger \hat{a}_j)^2. \tag{4.13}$$

The total Hamiltonian is then $\hat{\mathcal{H}} = \hat{\mathcal{H}}_{\text{SSH}} + \hat{\mathcal{H}}_{\text{int}}$. Consider a macroscopic occupation of the ground state. The energy spectrum of $\hat{\mathcal{H}}$ has a gap with a midgap topological state as shown in the left picture of Fig.4.2. We next add an additional term to the Hamiltonian:

$$\hat{\mathcal{H}}_{\text{quench}} = -\Delta \hat{a}_j^\dagger \hat{a}_j. \tag{4.14}$$

This term effectively shifts the chemical potential μ. We consider a quench from $\Delta = 0$ to a non-vanishing value of Δ. As was shown in [78] such a quench can induce dynamical instability in the edge states of the SSH model while keeping the bulk modes dynamically stable. This case is illustrated in Fig.4.2. As a result the edge states are populated exponentially fast [78].

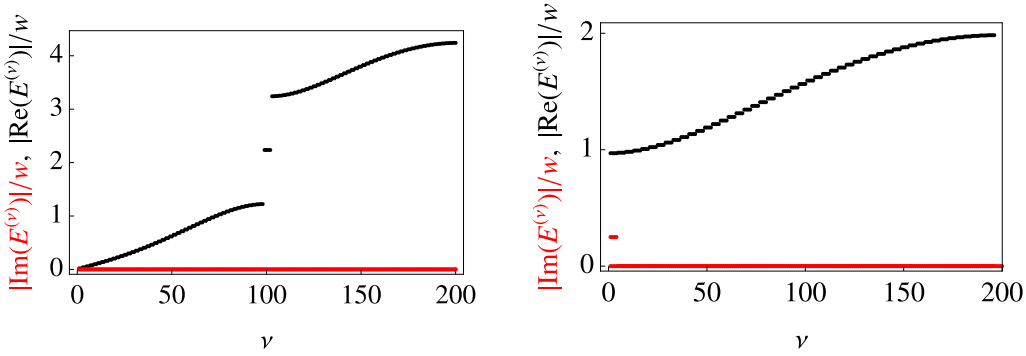

Figure 4.2: The real (black) and imaginary (red) parts of the Bogoliubov energy spectrum of the Su-Schrieffer-Heeger model in the absence of a quench (left figure), i.e. $\Delta = 0$, and after a quench with quench parameter $\Delta = 2w + \bar{\rho}U$. Here $\delta w = 2\bar{\rho}U = w/2$, and the lattice has 100 sites. To visualize the emergent edge states open boundary conditions at the edge were applied.

4.2 Nambu spinors and Bogoliubov energy

Prior to considering more complicated two-dimensional systems it is useful to reconsider the nature of dynamical instability discussed previously in this chapter by introducing Nambu spinors $\hat{\psi} = (\hat{a}_1, \hat{a}_2, \ldots, \hat{a}_1^\dagger, \hat{a}_2^\dagger, \ldots)^{\mathrm{T}}$. This is also a standard way to discuss the Bogoliubov–de Gennes Hamiltonian [79]. The symplectic transformation properties for bosons become apparent in terms of Nambu spinors. Let us introduce the Bogoliubov–de Gennes (BdG) Hamiltonian matrix H: $\hat{\mathcal{H}} = \hat{\psi}^\dagger H \hat{\psi}$. For a one-dimensional lattice of $\mathcal{N}$ sites H is a $2\mathcal{N} \times 2\mathcal{N}$ dimensional matrix. Although we consider here a one-dimensional system, the concept discussed below can be generalised to higher dimensional lattices. The Bogoliubov energies are the eigenvalues of $\tau_3 H$ [79]:

$$\tau_3 H v_\nu = E^{(\nu)} v_\nu, \tag{4.15}$$

where $\tau_3 = \mathrm{diag}(\mathbb{I}_\mathcal{N}, -\mathbb{I}_\mathcal{N})$ is the third Pauli matrix which acts on the Nambu spinor components, and $\mathbb{I}_\mathcal{N}$ is $\mathcal{N}$-dimensional identity matrix. The presence of τ_3 in the BdG equations is specific to bosons only, and it reflects the bosonic nature of the commutation relations: $[\hat{\psi}, \hat{\psi}^\dagger] = \tau_3$. The BdG Hamiltonian generically possesses a 'particle-hole' symmetry which requires the eigenval-

ues to come in $\pm E^{(\nu)}$ pairs. For each pair of stable (real) eigenvalues, one member will have positive norm defined with the τ_3 metric, $v^\dagger_{\nu^+}\tau_3 v_{\nu^+} > 0$, while the other will have negative norm $v^\dagger_{\nu^-}\tau_3 v_{\nu^-} < 0$. In analogy with BCS superconductors, we refer to bands composed of eigenstates with positive (negative) norms as 'particle' ('hole') bands. Notice that although H is a Hermitian matrix $\tau_3 H$ is not. This opens the possibility for complex values of the Bogoliubov energy, which is referred to as a dynamical instability in this thesis. For stable systems the Bogoliubov energies are always real. Also, negative norm states correspond to negative energies, while positive norm states correspond to positive energies, but this generally is not the case for unstable systems. In [80], the origin of a dynamical instability was traced to the overlap of positive and negative norm states in the limit when the pairing (non-particle number conserving) terms are small. Turning on finite pairing terms will generally lift such degeneracies and lead to complex Bogoliubov energies. This mechanism can be illustrated on the SSH model, and is shown in Fig.4.3. In Fig.4.3 the Bogoliubov energy values for positive norm states v_{ν^+} are represented by solid lines, while the dashed lines illustrate the energies corresponding to negative norm states v_{ν^-}. The energy dispersion of the topological edge states is shown in red. As the quenching parameter Δ changes the Bogoliubov energy bands of positive and negative norm states start to overlap, and at places where this overlap happens (shown in green) the energy spectrum becomes imaginary. On the other hand, as is evident from Fig. 4.3, one can have overlap between bulk particle and bulk hole bands which do not lead to dynamical instabilities. We interpret this as the states being protected from becoming dynamically unstable. We will discuss the origin of this effect later in this chapter, after we consider the dynamical instability in two-dimensional boson lattices. To our knowledge this effect of protection of the states from becoming dynamically unstable has not been discussed previously in the literature.

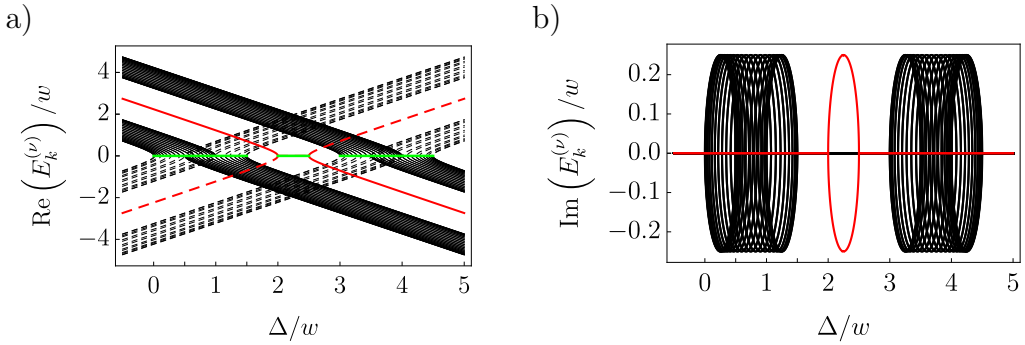

Figure 4.3: The real (a) and imaginary (b) parts of the Bogoliubov energy spectrum of the SSH model as a function of the quench parameter Δ. In red are highlighted the topological edge states, while the black color corresponds to the bulk spectrum. The solid (dashed) lines represent the particle (hole) energy spectrum. The region of Δ where the dynamical instability rises up is shown in green. All the relevant parameters of the SSH Hamiltonian were taken to be the same as in Fig. 4.2.

4.3 Topological spin dynamics in 2D boson lattices

To unveil the spin dynamics in two-dimensional boson lattices one has to introduce the spin components into the model Hamiltonian. For enabling the topological edge state to become dynamically unstable a different quench mechanism from the one discussed in the context of the Su-Schrieffer-Heeger model has to be introduced. Such a mechanism is suggested below. It will be shown how quenching spinor condensates can result in a fast population of edge states and a spin current at the edge of the lattice.

4.3.1 Quenching mechanism through quadratic Zeeman term

First, let us introduce spin-one boson operators $\hat{\mathbf{\Psi}}_i = (\hat{\Psi}_{i,1}, \hat{\Psi}_{i,0}, \hat{\Psi}_{i,-1})^T$ and consider a spin-one generalisation of lattice Hamiltonian

$$\hat{\mathcal{H}}_{\mathrm{latt}} = \sum_{ij} \hat{\mathbf{\Psi}}_i^\dagger \mathcal{H}_{\mathrm{latt}}^{ij} \hat{\mathbf{\Psi}}_j. \tag{4.16}$$

We consider on-site interactions terms that do not break spin rotational symmetry (the origin of these interaction terms has been discussed in Chapter 2):

$$\hat{\mathcal{H}}_{\text{int}} = \sum_j \frac{U}{2}\hat{\rho}_j^2 + \frac{U_S}{2}\hat{\mathbf{S}}_j^2, \tag{4.17}$$

where $\hat{\rho}_j = \hat{\mathbf{\Psi}}_j^\dagger \hat{\mathbf{\Psi}}_j$ and $\hat{\mathbf{S}}_j = \hat{\mathbf{\Psi}}_j^\dagger \mathbf{S} \hat{\mathbf{\Psi}}_j$ are the local density and spin operators respectively, and $\mathbf{S} = (S_x, S_y, S_z)$ denote the 3×3 spin-one matrices:

$$S_x = \frac{1}{\sqrt{2}}\begin{pmatrix} 0 & 1 & 0 \\ 1 & 0 & 1 \\ 0 & 1 & 0 \end{pmatrix}, \quad S_y = \frac{i}{\sqrt{2}}\begin{pmatrix} 0 & -1 & 0 \\ 1 & 0 & -1 \\ 0 & 1 & 0 \end{pmatrix}, \quad S_z = \begin{pmatrix} 1 & 0 & 0 \\ 0 & 0 & 0 \\ 0 & 0 & -1 \end{pmatrix}. \tag{4.18}$$

We also consider a quadratic Zeeman term $\hat{\mathcal{H}}_Z = q_Z \sum_j \hat{\mathbf{\Psi}}_j^\dagger S_z^2 \hat{\mathbf{\Psi}}_j$ which is experimentally adjustable using external magnetic fields or microwave fields [81]. The linear Zeeman term is omitted due to the S_z symmetry of our model. We require a positive q_Z in order to ensure the ground state is a spin-0 boson state. The total Hamiltonian reads:

$$\hat{\mathcal{H}} = \hat{\mathcal{H}}_{\text{latt}} + \hat{\mathcal{H}}_{\text{int}} + \hat{\mathcal{H}}_Z + \hat{V}_{\text{trap}} - \mu \sum_j \hat{\rho}_j, \tag{4.19}$$

where μ is the chemical potential and $\hat{V}_{\text{trap}} = \sum_j \hat{\mathbf{\Psi}}_i^\dagger V_{\text{trap}}^{ij} \hat{\mathbf{\Psi}}_j$ stands for trapping potential. All the terms that we have added to the lattice Hamiltonian can appear naturally as well as be synthetically induced in optical lattice experiments with cold atoms. Its relation to cold atoms has been introduced in the beginning of this thesis. In this chapter we focus on how such terms can contribute to dynamically excite boson topological edge states. In this section we consider strip geometry, i.e. periodic along one primitive lattice vector and a box-like potential with infinite walls in the direction of the other lattice vector. The effects of harmonic confining potential are discussed in the next chapter.

In order to investigate the dynamics of bosons in our system we will consider a quantum quench by abruptly changing the quadratic Zeeman energy strength

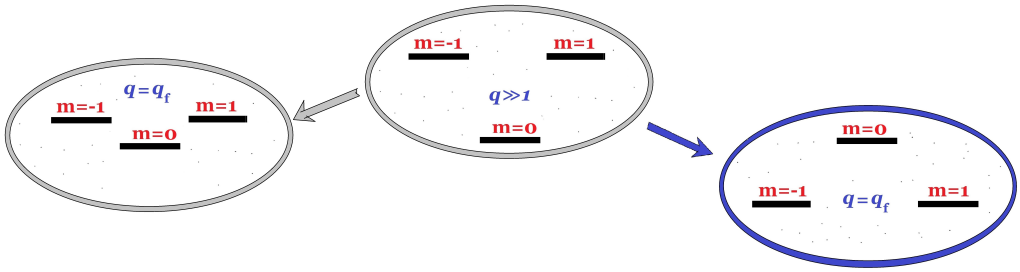

Figure 4.4: Schematic illustration of the quenching mechanism for spin-1 Bose gas: The system is first prepared in an initial state Ψ_{in} which is given by the $s_z = 0$ spin state at $q \gg 1$. Then a quench by changing q from a large and positive value to a smaller value q_f is performed.

q_Z from an initially large and positive value to a final value q_f (Fig. 4.4). This form of quenching has been experimentally achieved in several experiments in the past decade (see [57] and references therein). At low enough temperatures atoms occupy the ground state $\bar{\boldsymbol{\Psi}}_j$, which we treat classically. For sufficiently large and positive q_Z, the ground state is a polar state where $\bar{\mathbf{S}}_j = \bar{\Psi}_j^\dagger \mathbf{S} \bar{\Psi}_j = 0$ and $\bar{\boldsymbol{\Psi}}_j = (0, \sqrt{\bar{\rho}_j}, 0)^T$. We consider a slowly varying confining potential, much slower than the lattice characteristic length scale, so the ground state population extends over a considerable number of lattice sites. Provided the density and spin fluctuations, $\delta\hat{\rho} = \hat{\rho} - \bar{\rho}$ and $\delta\hat{\mathbf{S}} = \hat{\mathbf{S}} - \bar{\mathbf{S}}$, are small, the fluctuations about the ground state $\hat{\boldsymbol{\psi}} = \hat{\Psi} - \bar{\Psi}$ up to quadratic order are described by the Bogoliubov–de Gennes (BdG) Hamiltonian:

$$\begin{aligned}\hat{\mathcal{H}}_{\text{B}} &= \sum_{ij} \hat{\boldsymbol{\psi}}_i^\dagger \left(\mathcal{H}_{\text{latt}}^{ij} + \delta^{ij}(U\bar{\rho}_j - \mu) \right) \hat{\boldsymbol{\psi}}_j + \sum_j \hat{\boldsymbol{\psi}}_i^\dagger V_{\text{trap}}^{ij} \hat{\boldsymbol{\psi}}_j \\ &\quad + \sum_j q_Z \hat{\boldsymbol{\psi}}_j^\dagger S_z \hat{\boldsymbol{\psi}}_j + \frac{U}{2} \delta\hat{\rho}_j^2 + \frac{U_S}{2} \delta\hat{\mathbf{S}}_j^2. \end{aligned} \tag{4.20}$$

In this chapter we consider strip geometry with a box-like trapping potential along one primitive lattice vector, i.e. $V_{\text{trap}}^{i,j} = 0$ inside the trap and $V_{\text{trap}}^{i,j} = +\infty$ at the boundary, and periodic boundary conditions along the other directions. Due to S_z symmetry the spin-±1 components decouple from the spin-0 ones in $\mathcal{H}_B$. The density fluctuation term in (4.20) carries only spin-0 components $\delta\hat{\rho}_j^2 = \bar{\rho}_j(\hat{\psi}_{j,0}^\dagger \hat{\psi}_{j,0} + \hat{\psi}_{j,0}\hat{\psi}_{j,0} + \text{H.c.})$, while the spin fluctuation term couples the spin-±1 components: $\delta\hat{\mathbf{S}}_j^2 = 2\bar{\rho}_j(\hat{\psi}_{j,+1}^\dagger \hat{\psi}_{j,+1} +$

$\hat{\psi}^\dagger_{j,-1}\hat{\psi}_{j,-1} + \hat{\psi}_{j,+1}\hat{\psi}_{j,-1} + \hat{\psi}^\dagger_{j,+1}\hat{\psi}^\dagger_{j,-1}$). In typical spinor condensates, the spin-spin interaction is much smaller than the density-density interaction. For instance, for ^{87}Rb, U_S will be two orders of magnitude smaller than U. The Hamiltonian $\mathcal{H}_B$ is a more complicated version of the Bogoliubov Hamiltonian that was used to introduce dynamical instability in the beginning of this chapter. By analogy diagonalising the boson Bogoliubov Hamiltonian (4.20) is equivalent to diagonalising a non-Hermitian matrix. When complex valued Bogoliubov eigenenergies emerge the corresponding modes are referred to as dynamically unstable. As it will be shown on the example of the Kane-Mele model below, a situation can be achieved when only the edge states are dynamically unstable, while the bulk modes remain dynamically stable.

4.4 Topological spin dynamics of spin-one Kane-Mele model

For reasons related to symmetries, which will become evident at the end of this chapter, we consider a spin-one generalisation of the Kane-Mele model. The Kane-Mele model [16] has already been introduced in the first part of this thesis. It is a hexagonal lattice model with a non-trivial topological band structure. However, unlike Haldane's model the Kane-Mele model preserves the time-reversal symmetry. A spin-one generalisation of the Kane-Mele model is given by the Hamiltonian:

$$\hat{\mathcal{H}}_{\mathrm{S1KM}} = -w \sum_{\langle ij \rangle} \mathbf{\Psi}^\dagger_i \mathbf{\Psi}_j + i\lambda \sum_{\langle\langle ij \rangle\rangle} \nu_{ij} \mathbf{\Psi}^\dagger_i S_z \mathbf{\Psi}_j \tag{4.21}$$

where $\mathbf{\Psi}_i = (\mathbf{\Psi}_{i,1}, \mathbf{\Psi}_{i,0}, \mathbf{\Psi}_{i,-1})^T$ is a vector composed of bosonic annihilation operators at site i for each spin component. The second term above describes hopping between second neighbours, and $\nu_{ij} = +1(-1)$ if the atom makes a left (right) turn to reach a second-neighbour site [16]. The primitive lattice vectors, as shown in Fig. 4.5 are $\mathbf{a}_1 = \left(\sqrt{3}/2, 1/2\right)$ and $\mathbf{a}_2 = \left(\sqrt{3}/2, -1/2\right)$, where we have set the lattice constant to unity. The spin components are decoupled in $\hat{\mathcal{H}}_{\mathrm{S1KM}}$: the spin-zero component is described by the nearest-neighbour graphene model with hopping w while the spin-±1 components are described by two Haldane models [15] with opposite magnetic fields. The

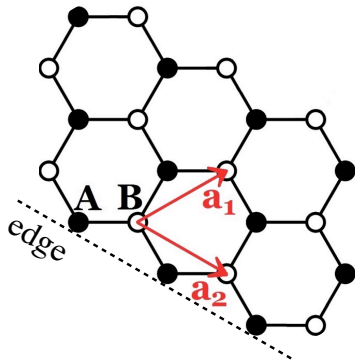

Figure 4.5: A portion of the hexagonal lattice used for the spin-one Kane-Mele Hamiltonian. Triangular sublattice sites A and B are labelled by closed and open circles respectively. The lattice basis vectors are given by $\mathbf{a}_1$ and $\mathbf{a}_2$.

total Hamiltonian is obtained by replacing $\hat{\mathcal{H}}_{\text{lattice}}$ with $\hat{\mathcal{H}}_{\text{S1KM}}$ in (4.19). It is invariant under time reversal and global spin rotations about the z-axis, the importance of which will be addressed later.

4.4.1 Initial state

At large positive q_Z and temperatures close to absolute zero the energetically favourable state is the null z-component spin state. Hence at large q_Z the low energy physics is determined by $\hat{\Psi}_{j,0}$ and all the bosons fall into its ground state, which forms a Bose-Einstein condensate. At this regime the ground state is macroscopically occupied and therefore it is reasonable to approximate the action of field operators $\hat{\mathbf{\Psi}}_j$ with vector functions $\bar{\Psi}_{j,0} = \sqrt{\bar{\rho}_j}\exp\{i\theta_j\}$. We use a variational approach to find the ground state. For this we define the Lagrangian $\mathcal{L} = i\sum_j(\bar{\Psi}^\dagger_{j,0}\partial_t\bar{\Psi}_{j,0} - \bar{\Psi}^{\mathrm{T}}_{j,0}\partial_t\bar{\Psi}^*_{j,0})/2 - \mathcal{H}[\bar{\Psi}_{j,0}, \bar{\Psi}^\dagger_{j,0}] - \mu\sum_j \bar{\Psi}^\dagger_{j,0}\bar{\Psi}_{j,0}$ which reduces to:

$$\begin{aligned}\mathcal{L} = &-\sum_l(\bar{\rho}^A_l\dot{\bar{\theta}}^A_j + \bar{\rho}^B_l\dot{\bar{\theta}}^B_l) + 2w\sum_{\langle l,l'\rangle}\sqrt{\bar{\rho}^A_{l'}\bar{\rho}^B_l}\cos(\bar{\theta}^B_{l'} - \bar{\theta}^A_l)\\ &-\frac{U}{2}\sum_l\left((\bar{\rho}^A_l)^2 + (\bar{\rho}^B_l)^2\right) - \mu\sum_l(\bar{\rho}^A_l + \bar{\rho}^B_l),\end{aligned} \tag{4.22}$$

where l label the unit cell, and A and B denote the two sublattices.

The corresponding Euler-Lagrange equations are:

$$\frac{d}{dt}\frac{d\mathcal{L}}{d\dot{\bar{\theta}}_l^A} = \frac{d\mathcal{L}}{d\bar{\theta}_l^A}: \quad -\dot{\bar{\rho}}_l^A = 2w \sum_{l':\langle l',l\rangle} \sqrt{\bar{\rho}_l^A \bar{\rho}_{l'}^B}\sin(\bar{\theta}_l^B - \bar{\theta}_{l'}^A),$$

$$\frac{d}{dt}\frac{d\mathcal{L}}{d\dot{\bar{\rho}}_l^A} = \frac{d\mathcal{L}}{d\bar{\rho}_l^A}: \quad 0 = -\dot{\theta}_l^A + w \sum_{l':\langle l',l\rangle} \sqrt{\frac{\bar{\rho}_{l'}^B}{\bar{\rho}_l^A}}\cos(\bar{\theta}_l^B - \bar{\theta}_{l'}^A) - U\bar{\rho}_l^A + \mu.$$

The above equations are satisfied for $\bar{\rho}_j^A = \bar{\rho}_j^B = \bar{\rho}$ and $\bar{\theta}_j^A = \bar{\theta}_j^B = 0$ with $\mu = -3J + U\bar{\rho}$. Hence, prior to quenching q we prepare the system in a spatially uniform spin-zero state state $\bar{\mathbf{\Psi}}_{\mathrm{in},j} = (0, \sqrt{\bar{\rho}}, 0)$ initial state. Open boundary conditions alter the uniformity of the initial state near the boundary. We, however, will neglect this effect in our computations.

4.4.2 Bogoliubov energy spectrum and the emergence of dynamical instabilities

We now turn to the investigation of the dynamics after the quench which is determined by the quantum fluctuation around the initial state $\left|\bar{\mathbf{\Psi}}_{\mathrm{in}}\right\rangle$. The small quantum fluctuation around the ground state, $\hat{\boldsymbol{\psi}}_i = \hat{\mathbf{\Psi}}_i - (0, \sqrt{\bar{\rho}}, 0)$, are described by the Bogoliubov Hamiltonian (5.3) with $q_Z = q_f$. For the Kane-Mele model one has

$$\begin{aligned}\hat{\mathcal{H}}_B = &-w\sum_{\langle ij\rangle}\hat{\boldsymbol{\psi}}_i^\dagger\hat{\boldsymbol{\psi}}_j + i\lambda\sum_{\langle\langle ij\rangle\rangle}\nu_{ij}\hat{\boldsymbol{\psi}}_i^\dagger S_z\hat{\boldsymbol{\psi}}_j + \sum_i \hat{\boldsymbol{\psi}}_i^\dagger M\hat{\boldsymbol{\psi}}_i \\ &+ \sum_i\left[\left(\frac{U\bar{\rho}}{2}\hat{\psi}_{i,0}\hat{\psi}_{i,0} + U_s\bar{\rho}\hat{\psi}_{i,1}\hat{\psi}_{i,-1}\right) + \mathrm{H.c.}\right] \qquad (4.23)\end{aligned}$$

where

$$M = \begin{pmatrix} 3w + U_s\bar{\rho} + q_f & 0 & 0 \\ 0 & 3w + U\bar{\rho} & 0 \\ 0 & 0 & 3w + U_s\bar{\rho} + q_f \end{pmatrix} \qquad (4.24)$$

and q_f is the quadratic Zeeman energy after the quench. Noticeably the spin-zero components decouple from the spin-±1 in $\hat{\mathcal{H}}_B$, i.e. $\hat{\mathcal{H}}_B = \hat{\mathcal{H}}_0 + \hat{\mathcal{H}}_{\pm1}$. The

energy spectrum of $\hat{\mathcal{H}}_0$ has a usual linearly-dispersing phonon mode and is real. Unlike the spin-zero component part, the Hamiltonian $\hat{\mathcal{H}}_{\pm 1}$ for spin-± 1 components has a spin-orbit coupling and depends on the quenched term q_f. From now on, we will focus on the spin-± 1 sector.

To investigate the energy spectrum and the dynamics of the edge states we consider a strip geometry with open boundary conditions along the primitive vector $\mathbf{a}_1$, and closed boundary conditions along $\mathbf{a}_2$. It is convenient to switch to the eigenbasis of the non-interacting spin-one Kane-Mele model (4.21). The spin-± 1 Hamiltonian then becomes

$$\hat{\mathcal{H}}_{\pm 1} = \sum_{k,\nu} \Big[(\varepsilon_k^{(\nu)} - \Delta)(\hat{\alpha}^\dagger_{k,\nu,1}\hat{\alpha}_{k,\nu,1} + \hat{\alpha}^\dagger_{-k,\nu,-1}\hat{\alpha}_{-k,\nu,-1}) + \; U_s\bar{\rho}(\hat{\alpha}_{k,\nu,1}\hat{\alpha}_{-k,\nu,-1} + \text{H.c.})\Big]\,. \tag{4.25}$$

Here, $\varepsilon_k^{(\nu)}$ are the single-particle energies of the Haldane model in the strip geometry, $k = \mathbf{k}\cdot\mathbf{a}_2$ denotes the momentum along the periodic direction, and $\hat{\alpha}_{k,\nu,m}$ annihilates a boson in the eigenbasis of (4.21). We have introduced $\Delta = -U_s\bar{\rho} - 3w - q_f$ which will serve as the tuning parameter for our quantum quench. Due to time-reversal symmetry and the spatial uniformity of the initial state, the Hamiltonian can be separated into pairwise couplings between (k,ν,m) and $(-k,\nu,-m)$ modes which greatly simplifies the analysis.

Unlike $\hat{\mathcal{H}}_0$, $\hat{\mathcal{H}}_{\pm 1}$ cannot in general be brought to diagonal form and may exhibit a dynamical instability. In order to investigate its dynamics one may solve the corresponding Heisenberg equations of motion:

$$i\partial_t\hat{\alpha}_{k,\nu,\pm 1}(t) = [\hat{\alpha}_{k,\nu,\pm 1}(t), \hat{\mathcal{H}}_{\pm 1}]. \tag{4.26}$$

The explicit form of $\hat{\alpha}_{k,\nu,\pm 1}(t)$ can be found for instance by applying the Baker-Campbell-Hausdorff relation to $\hat{\alpha}_{k,\nu,\pm 1}(t) = e^{i\hat{\mathcal{H}}_{\pm 1}t}\hat{\alpha}_{k,\nu,\pm 1}e^{-i\hat{\mathcal{H}}_{\pm 1}t}$ or searching for a solution as a linear combination of creation and annihilation oper-

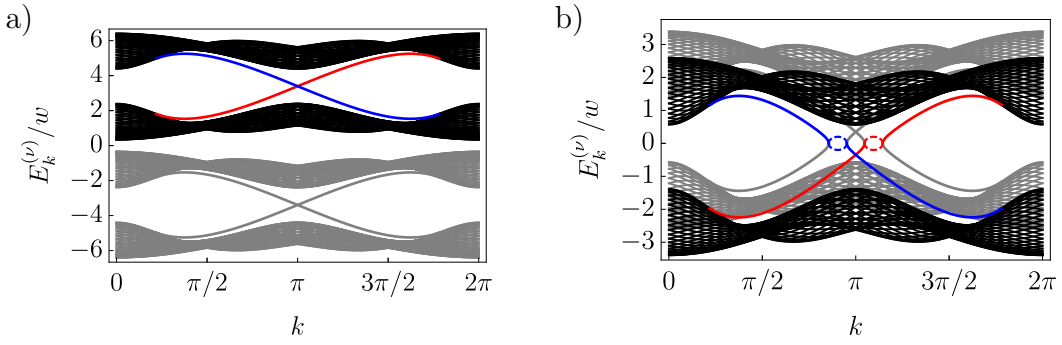

Figure 4.6: The Bogoliubov energy spectrum $\pm E_k^{(\nu)}$ corresponding to (4.28) for the interacting spin-one Kane-Mele model in the strip geometry. Parameters in (a) are $U_s\bar{\rho} = 0.2w$, $\lambda = w/2$ and $q_f = U_s\bar{\rho}$ which corresponds to a shallow quench with stable spectrum. Parameters in (b) are the same as (a) except $q_f = -3w - 3U_s\bar{\rho}$ for which the bulk states are stable while the edge states experience an exponentially fast population growth. Grey curves indicate hole bands while black curves indicate bulk particle bands. Red and blue curves indicate edge states propagating in opposite directions. For clarity, edge states on only one side of the system are plotted (on the opposite side, the roles of the particle and hole edge bands are reversed). Imaginary parts of eigenvalues are given by dashed lines.

ators with time dependent coefficients. These give

$$\begin{aligned}\hat{\alpha}_{k,\nu,1}(t) &= A_{k,\nu}(t)\hat{\alpha}_{k,\nu,1} + B_{k,\nu}(t)\hat{\alpha}^\dagger_{-k,\nu,-1}\,,\\ \hat{\alpha}_{-k,\nu,-1}(t) &= B_{k,\nu}(t)\hat{\alpha}^\dagger_{k,\nu,1} + A_{k,\nu}(t)\hat{\alpha}_{-k,\nu,-1}\,.\end{aligned} \tag{4.27}$$

where

$$\begin{aligned}A_{k,\nu}(t) &= \cos(E_k^{(\nu)}t) - i(\varepsilon_k^{(\nu)} - \Delta)\frac{\sin(E_k^{(\nu)}t)}{E_k^{(\nu)}},\\ B_{k,\nu}(t) &= -iU_s\bar{\rho}\frac{\sin(E_k^{(\nu)}t)}{E_k^{(\nu)}},\end{aligned}$$

with the Bogoliubov energies

$$E_k^{(\nu)} = \sqrt{(\varepsilon_k^{(\nu)} - \Delta)^2 - (U_s\bar{\rho})^2}. \tag{4.28}$$

For the sake of this work it is important is to notice that the energy values $E_k^{(\nu)}$ in (4.28) may acquire imaginary part when the quench parameter Δ is

tuned to satisfy

$$\varepsilon_k^{(\nu)} - U_s\bar{\rho} < \Delta < \varepsilon_k^{(\nu)} + U_s\bar{\rho}. \tag{4.29}$$

This is known to be due to emergence of dynamical instability in the system. Physically, this provides exponentially fast population of the unstable modes.

The same criteria of the emergence of dynamical instabilities (4.29) holds for both bulk and edge modes. However, the edge states have different energy dispersions ϵ_k^{edge}, which connect the bulk energy bands ϵ_k^{ν} separated by gaps. Previously it was shown that the dispersion of the edge states is

$$\varepsilon_k^{\text{edge}} = \pm\frac{6w\lambda\sin(k)}{\sqrt{w^2 + 16\lambda^2\sin^2(\frac{k}{2})}}, \tag{4.30}$$

where the spin-±1 modes propagate in opposite directions.

This suggests that there are different "windows" for inducing dynamical instabilities for bulk and edge modes when changing the tuning parameter Δ. One can take advantage of this in order to create a situation when only the edge states are dynamically unstable, while the bulk ones remain stable. A similar scheme for populating edge modes has been previously reported in [78]. However, unlike [78], due to the tuneability of Δ, the current scheme allows one to selectively populate states with particular momenta along the edge. From (4.28), we see that the most unstable modes occur at momenta for which $\varepsilon_k^{(\nu)} = \Delta$, so, for instance, when $\Delta = 0$, edge modes with momenta $k = \pi$ will be populated most rapidly. Bulk and edge energy bands are shown in Fig. 4.6 for two particular quenches. Fig. 4.6(a) shows the Bogoliubov energy spectrum after a a shallow quench to $q_f = U_s\bar{\rho}$. The energy spectrum is real, and therefore no dynamical instability is induced. Fig. 4.6(b), on the other hand, shows a quench which makes part of the Bogoliubov energy spectrum imaginary (illustrated by the dashed lines). The system therefore exhibits dynamical instability. Notice, however, that only the edge states become dynamically unstable, while the bulk bands remain stable during the quenched dynamics. The figure illustrates how edge states can be selectively driven to a dynamically unstable state. In the next sections we will address

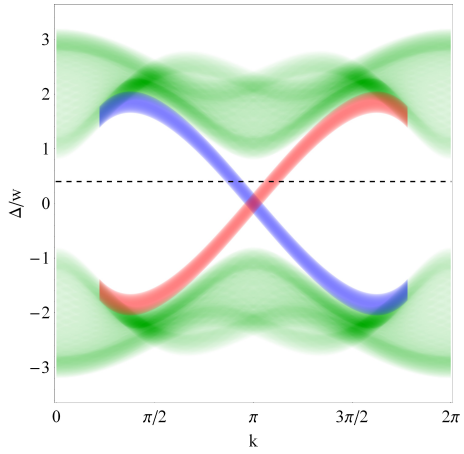

Figure 4.7: Instability phase diagram. The blue and red regions correspond to regions of edge-mode dynamical instabilities. The edge colour scheme used is the same as in Fig. 4.6. The green region signifies the emergence of bulk instabilities. Its intensity is proportional to the mode degeneracy. Here $U_s\bar{\rho} = 0.2w$ and $\lambda = w/2$. The dashed line shows to the choice of quenching parameter $\Delta = 2U_s\bar{\rho}$ used in Fig. 4.6, i.e. $q_f = -3w - 3U_s\bar{\rho}$. It is clearly seen that there is a wide range of parameter choice Δ where only the edge states are dynamically unstable (in correspondence with the instability condition (4.29)).

the consequences of the selectively induced dynamical edge instability on the time evolution of the particle density and the spin current.

4.4.3 Dynamically induced edge density population and spin current

We now move on to discuss the physical consequences related to the quenching protocol. For sufficiently low condensate depletion, the Bogoliubov Hamiltonian can be used to propagate the initial state as $|\Psi(t)\rangle = e^{-i\hat{\mathcal{H}}_B t}\left|\bar{\mathbf{\Psi}}_{\text{in}}\right\rangle$. The solutions to the Heisenberg equations of motion (4.27) can then be used to obtain the expectation value of bilinear operators as

$$\begin{aligned} \langle\Psi(t)|\,\hat{\alpha}^{\dagger}_{k,\nu,m}\hat{\alpha}_{k',\nu',m'}\,|\Psi(t)\rangle &= \delta_{k,k'}\delta_{\nu,\nu'}\delta_{m,m'}|B_{k,\nu}|^2 \\ \langle\Psi(t)|\,\hat{\alpha}_{k,\nu,m}\hat{\alpha}_{k',\nu',m'}\,|\Psi(t)\rangle &= \delta_{k,-k'}\delta_{\nu,\nu'}\delta_{m,-m'}A_{k,\nu}B_{k,\nu} \end{aligned} \tag{4.31}$$

for spin $m = \pm 1$ components.

Let us now consider the number of particles excited into the spin-± 1 modes

as a result of the quench. Using (4.31), we find

$$\mathcal{N}_{\pm 1}(t) = \langle \Psi(t)| \sum_i (\hat{\psi}^\dagger_{i,1}\hat{\psi}_{i,1} + \hat{\psi}^\dagger_{i,-1}\hat{\psi}_{i,-1}) |\Psi(t)\rangle = 2\sum_{k,\nu} |B_{k,\nu}(t)|^2. \quad (4.32)$$

When all bulk energies are real and only the edgestates acquire imaginary energies the time evolution of $\mathcal{N}_{\pm 1}$ will become dominated by the edgestates with imaginary eigenvalues $E^{(c)}_{edge,\pm} = \pm i|E^{(c)}|$:

$$|B^{\text{edge}}_{k,\pm 1}(t)|^2 \quad \sim \quad (\bar{\rho}U_s)^2 \frac{\sinh^2(|E^{(c)}_{k_x}|t)}{|E^{(c)}_{k_x}|^2}.$$

Keeping only unstable modes and linearising the edge spectrum about $k = \pi$, for $\bar{\rho}|U_s|t \gg 1$ one finds

$$\mathcal{N}_{\pm 1}(t) \approx \sqrt{1 + \frac{16\lambda^2}{w^2}} \frac{N_2}{12\lambda} \sqrt{\frac{|U_s|\bar{\rho}}{\pi t}} e^{2|U_s|\bar{\rho}t}, \quad (4.33)$$

where N_2 is the number of lattice sites along the $\mathbf{a}_2$ direction.

A physically important dynamical observable is spin current. As we show next, the quenching protocol induces a spin current along the edge. An expression for the spin current operator can be found using the continuity equation for the local spin moments $\hat{\mathbf{\Psi}}^\dagger_i S_z \hat{\mathbf{\Psi}}_i$. At long wavelengths this gives [13] (see also Appendix A)

$$\hat{\mathcal{J}}^{(s_z)}_k = \frac{1}{N_2} \sum_{k',m=\pm 1} m\, \hat{\Psi}^\dagger_{k-\frac{k'}{2},m} \partial_{k'} H^{(m)}_{k'} \hat{\Psi}_{k+\frac{k'}{2},m}, \quad (4.34)$$

where $\hat{\Psi}_{k,m}$ is a $2N_1$-dimensional vector composed of annihilation operators for spin-m bosons on sites in a unit cell of the strip geometry. $H^{(m)}_k$ is the non-interacting Bloch Hamiltonian matrix for spin component m which can be directly determined from (4.21). We wish to evaluate the expectation value of this operator with the state $|\Psi(t)\rangle$. Writing $\hat{\mathcal{J}}^{(s_z)}_k$ in an eigenbasis of the non-interacting Hamiltonian, employing (4.31) and the Feynman-Hellman

relation, we find the intuitive relation

$$J^{(s_z)}(t) \equiv \langle \hat{\mathcal{J}}^{(s_z)}_{k=0} \rangle = \frac{2}{N_2} \sum_{k',\nu} \partial_{k'} \varepsilon^{(\nu)}_{k'} |B_{k',\nu}(t)|^2, \tag{4.35}$$

where the two spin components have contributed an equal amount. Additionally, the $k \neq 0$ components of $\langle \hat{\mathcal{J}}^{(s_z)}_{k} \rangle$ vanish. Under the same conditions as were used for the evaluation of $\mathcal{N}_{\pm 1}$, one finds

$$J^{(s_z)}(t) \approx \frac{1}{4} \sqrt{\frac{|U_s|\bar{\rho}}{\pi t}} e^{2|U_s|\bar{\rho}t}. \tag{4.36}$$

We would like to stress the importance of our results. The exponential growth in the particle population (4.33) and the spin current (4.36) at the edge imply that the topological edge states dominate the dynamics of the system within the quench framework we introduced in this chapter. This can potentially open new possibilities for the experimental investigation of the topological edge dynamics in bosonic systems. We will come back to this discussion at the end of this chapter. Note that our results are also valid for negative U_s, *e.g.* for Rb atoms.

4.4.4 Role of time reversal (TRS), inversion (IS) and S_z symmetries in Spin-1 Kane-Mele model

The spin 1 Kane-Mele model has time reversal (TRS), inversion (IS) and S_z symmetries, which considerably simplify the analysis. In this subsection we address the question of how important these symmetries are for the dynamical instabilities to occur. In fact, we show that small perturbations to the Bogoliubov Hamiltonian $\hat{\mathcal{H}}_B$ that break time reversal symmetry (TRS), inversion symmetry (IS), or S_z symmetry can lead to the emergence of dynamical instabilities coming from the hybridisation of bulk modes in the particle-hole picture. Below we give three terms that we add to the Hamiltonian $\hat{\mathcal{H}}_B$ which break either TRS, IS, or S_z symmetry while preserving the other two.

Time reversal symmetry is a symmetry under inversion of time $t \to -t$.

Such an operation changes the signs of momentum and spin, and can be represented by the operator $\hat{T} = \exp(-i\pi S_y)\hat{K}$, where $\hat{K}$ stands for complex conjugation and S_y is spin-1 generator that rotates the spin around the y-axis by π (consequently $\exp(-i\pi S_y)$ flips the spin). To break TRS we consider a term that changes sign under time reversal, but preserves IS and S_z symmetry:

$$\hat{V}_T = i\delta \sum_{i,j} \nu_{i,j} \hat{\boldsymbol{\psi}}_i^\dagger S_z^2 \hat{\boldsymbol{\psi}}_i \tag{4.37}$$

where δ is taken to be a real and small in comparison to other energy scales of the problem.

Inversion symmetry, on the other hand, is a symmetry related to the two triangular sublattices A and B (Fig.4.5). Consequently it reverses the sign of coordinate and momentum operators, while keeping the spins untouched. IS can be broken, while keeping the TRS and S_z symmetry intact, by adding a staggered pairing between the two triangular sublattices A and B (Fig. 4.5):

$$\hat{V}_I = \delta \sum_n \left(\hat{\psi}_{n,1}^{(A)} \hat{\psi}_{n,-1}^{(A)} - \hat{\psi}_{n,1}^{(B)} \hat{\psi}_{n,-1}^{(B)} + \text{H.c.} \right) \tag{4.38}$$

where n labels unit cells.

Finally, S_z symmetry reflects the conservation of $\hat{S}_z \equiv \hat{\boldsymbol{\psi}}^\dagger S_z \hat{\boldsymbol{\psi}} = \hat{\psi}_1^\dagger \hat{\psi}_1 - \hat{\psi}_{-1}^\dagger \hat{\psi}_{-1}$: $[\hat{S}_z, \hat{\mathcal{H}}] = 0$. To break S_z symmetry we consider the contribution of same spin-component pairing terms

$$\hat{V}_{S_z} = \delta \sum_i \left(\hat{\psi}_{i,1} \hat{\psi}_{i,1} + \hat{\psi}_{i,-1} \hat{\psi}_{i,-1} + \text{H.c.} \right) \tag{4.39}$$

This term preserves TRS and IS.

In Fig. 4.8 we show the real and imaginary parts of Bogoliubov energy spectrum computed numerically after adding each of these terms to the Hamiltonian $\hat{\mathcal{H}}_B$. In addition to edge dynamical instabilities discussed in the main text, some bulk bands acquire a small imaginary part in the energy spectrum. This effect is amplified with the increase of δ and disappears in the absence

of the symmetry breaking terms.

4.5 Remarks on symmetry protection of mode dynamical stability

We have shown that breaking the time-reversal, inversion or S_z symmetry in our model forces some of the bulk modes to become dynamically unstable. The reason behind this has not yet been discussed. Below we show from general considerations that the time-reversal, inversion and S_z symmetry protect the bulk modes from becoming dynamically unstable. For this reason we split the Bogoliubov Hamiltonian $\hat{\mathcal{H}}_B$ into pairing and non-pairing terms:

$$\hat{\mathcal{H}}_B = \sum_{i,j} \left(\hat{\boldsymbol{\psi}}_i^\dagger F_{i,j} \hat{\boldsymbol{\psi}}_j + \hat{\boldsymbol{\psi}}_i^\dagger G_{i,j} \hat{\boldsymbol{\psi}}_j^\dagger + \text{H.c.} \right) \tag{4.40}$$

where the non-pairing term is Hermitian $F^\dagger = F$, while the pairing matrix is symmetric $G^{\mathrm{T}} = G$ for bosons. We also switched to coordinate representation for the sake of generality. It is constructive changing to Nambu basis $(\hat{\boldsymbol{\psi}}, \hat{\boldsymbol{\psi}}^\dagger)^{\mathrm{T}}$. In this basis the Hamiltonian $\hat{\mathcal{H}}_B$ is determined by a Hermitian matrix:

$$H = \begin{pmatrix} F & G \\ G^* & F^* \end{pmatrix} \tag{4.41}$$

It has to be stressed that even though H is Hermitian, the Bogoliubov energy values E are eigenvalues of a non-Hermitian operator $\tau_3 H$. The eigenvalues of $(\tau_3 H)^2$ are E^2. Hence, if $(\tau_3 H)^2$ is Hermitian matrix then E^2 are real and $\tau_3 H$ admits only either pure imaginary or pure real eigenvalues.

It is easy to see that for $(\tau_3 H)^2$ to be Hermitian one has to impose $FG = GF^*$, or $F = GF^*G^{-1}$ if G is invertible. This means that G has to act as a complex conjugation operator K on F. For a time-reversal invariant system $F = TFT^{-1} = R_S F^* R_S$, where $T = R_S K$ is time-reversal operator and

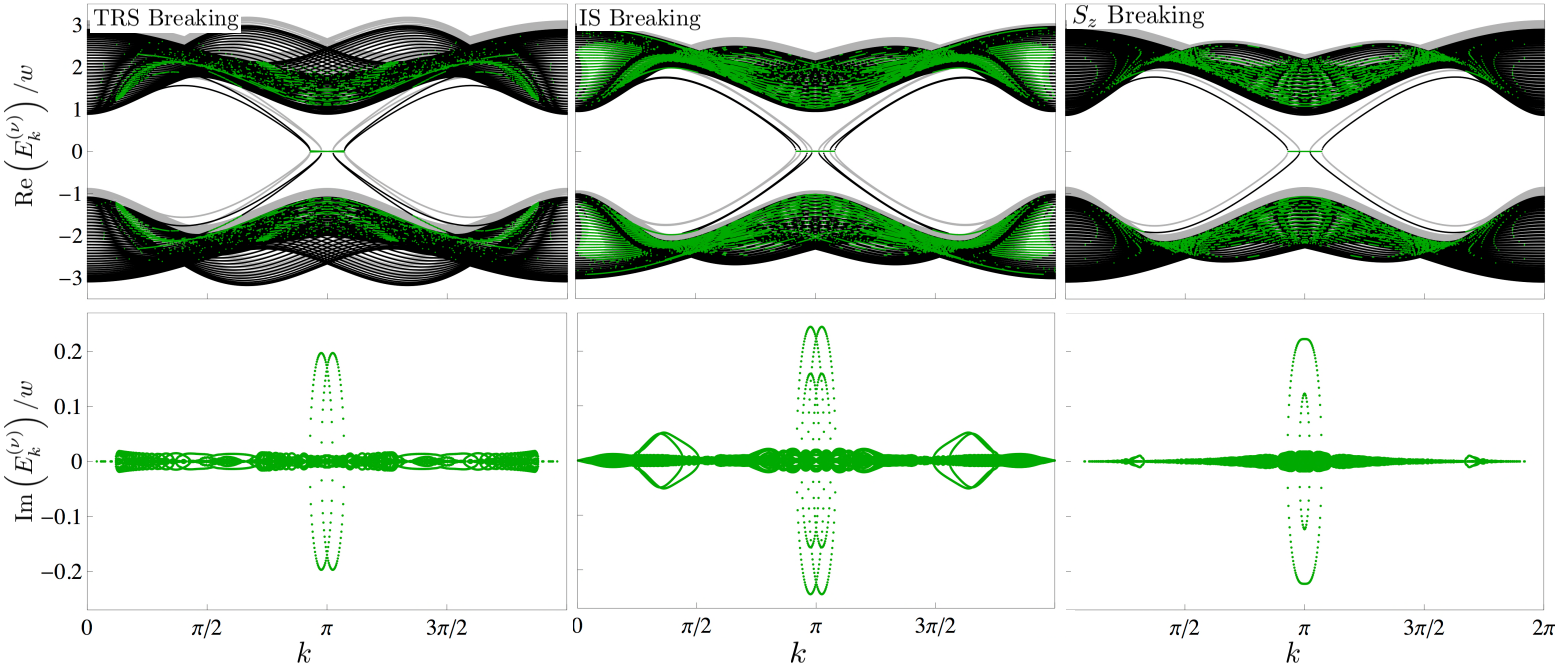

Figure 4.8: Bogoliubov energy spectrum $E_k^{(\nu)}$ for the interacting spin-one Kane-Mele model with a broken time-reversal, inversion, and S_z symmetries. Parameters are chosen to be $U_s\bar{\rho} = 0.2w$, $\lambda = w/2$, and $q_f = -3w - 3U_s\bar{\rho}/2$, and $\delta = 0.095w$. Grey curves indicate hole bands while black curves indicate bulk bands. The energy values corresponding to dynamically unstable modes (with finite imaginary component) are coloured in green. For clarity, modes from the zero spin component (which is always stable) are excluded from these figures/Chapter3.

$R_S = \exp(-i\pi S_y)$ flips the spins by a rotation by π around y-direction:

$$S_y = \frac{1}{\sqrt{2}} \begin{pmatrix} 0 & -i & 0 \\ i & 0 & -i \\ 0 & i & 0 \end{pmatrix}, \quad R_s = e^{-i\pi S_y} = \begin{pmatrix} 0 & 0 & 1 \\ 0 & -1 & 0 \\ 1 & 0 & 0 \end{pmatrix}.$$

Then the condition for hermicity of H for time-reversal systems translates to G being a product of a spin-flip operator R_S and an operator A that commutes with the non-pairing term F: $G = R_S A$. If the system has certain symmetries, then A may include a product of operators that leave the system invariant.

For spin-1 Kane-Mele model $A = -\bar{\rho}(U - U_s)/2 - \bar{\rho}(U + U_s)\exp(i\pi S_z)/2$, which commutes with F due to S_z symmetry. A also preserves the inversion symmetry. Hence, with the TRS, IS and S_z symmetries present and further requirement that the mean-field density (used to derive the Bogoliubov Hamiltonian) is spatially uniform, $(\tau_3 H)^2$ is a Hermitian matrix. This implies that the eigenvalues of $(\tau_3 H)^2$, namely E^2, will be real numbers and so E will either be pure real or pure imaginary. This means that an imaginary part in the energy spectrum will arise only in the region of overlap of particle and hole bands with vanishing real part of the energy. When the zero value of the real energy spectrum is situated in the gapped region, no dynamical instability is induced except in the crossing edge states. In this sense, these symmetries protect the bulk bands from becoming dynamically unstable. While the spin-1 Kane-Mele model possesses these symmetries, it is possible that less stringent conditions exist. Below we explore this question. In particular, we show that the symmetries of the Hamiltonian and the initial state, which make the single-particle Hamiltonian matrix commute with the anomalous matrix term, are crucial in protecting the dynamical stability of bulk states when the zero energy level sits in the middle of the gap. Although we find some indications that less stringent conditions can exist, a full classification based on symmetries that protect the bulk modes from becoming dynamically unstable remains to be found.

Let $(u_E, v_E)^{\mathrm{T}}$ be the eigenvector with eigenvalue E of the Bogoliubov Hamiltonian written in Nambu representation. Then the Schrodinger equation can

be written as a set of coupled equations:

$$(F - E)u_E = -Gv_E \text{ and } (F^* + E)v_E = -G^*u_E \tag{4.42}$$

where '*' stands for complex conjugation, G and G^* are the anomalous terms, and F and F^* correspond to non-pairing terms. For bosons $G^{\mathrm{T}} = G$ and $F^\dagger = F$.

By multiplying first term with $F^* + E$ and second term by $F - E$ one gets

$$\begin{aligned}\left[F^*F - GG^* - E^2 + E(F - F^*)\right] u_E &= -[F^*, G]v_E \\ \left[FF^* - G^*G - E^2 + E(F - F^*)\right] v_E &= -[F, G^*]u_E\end{aligned}$$

When $[G, F] = 0$ and the single-particle Hamiltonian F is time reversal invariant, i.e. $F^* = F$, the above system decouples and the dynamically unstable modes can acquire only pure imaginary energy values. This means that the imaginary part in energy spectrum will rise only in the region of overlap of particle and hole bands with vanishing real part of energy E. When the zero value of real energy spectrum is situated in the midgap region, no dynamical instability is induced except for crossing edge states. In this sense, time reversal symmetry and the symmetries that guarantee $[G, F] = 0$ protect the bulk bands from becoming dynamically unstable. Notice that this can be generalised to any physical system of interacting Bosons in regime where Bogoliubov approximation is valid.

In order to reflect the significance of time-reversal symmetry in our model, it is convenient to switch from the conventional Nambu representation of spinors $(\hat{\boldsymbol{\psi}}, \hat{\boldsymbol{\psi}}^\dagger)^{\mathrm{T}} = (\hat{\psi}_1, \hat{\psi}_0, \hat{\psi}_{-1}, \hat{\psi}_1^\dagger, \hat{\psi}_0^\dagger, \hat{\psi}_{-1}^\dagger)^{\mathrm{T}}$ to the one of $(\hat{\boldsymbol{\psi}}, R_s\hat{\boldsymbol{\psi}}^\dagger)^{\mathrm{T}} = (\hat{\psi}_1, \hat{\psi}_0, \hat{\psi}_{-1}, \hat{\psi}_{-1}^\dagger, -\hat{\psi}_0^\dagger, \hat{\psi}_1^\dagger)^{\mathrm{T}}$. This leads to a replacement $F^* \to F_T = R_sF^*R_s^\dagger = TFT^{-1}$ i.e. a time reversed expression of F, $G \to G' = GR_s^\dagger$ and $G^* \to R_sG^* = G'^\dagger$ in the Bogoliubov Hamiltonian:

$$H_B = \hat{\boldsymbol{\psi}}^\dagger F\hat{\boldsymbol{\psi}} + (R_s\hat{\boldsymbol{\psi}})F_T(R_s\hat{\boldsymbol{\psi}})^\dagger + \hat{\boldsymbol{\psi}}^\dagger G'(R_s\hat{\boldsymbol{\psi}}^\dagger) + (\hat{\boldsymbol{\psi}}R_s)G'^\dagger\hat{\boldsymbol{\psi}} \tag{4.43}$$

i.e.

$$H_B = \begin{pmatrix} F & G \\ G^* & F^* \end{pmatrix} \rightarrow H_B = \begin{pmatrix} F & GR_s^\dagger \\ R_sG^* & R_sF^*R_s^\dagger \end{pmatrix} = \begin{pmatrix} F & G' \\ G'^\dagger & F_T \end{pmatrix} \quad (4.44)$$

Let $(u_E, v_E)^{\mathrm{T}}$ be the eigenvector with eigenvalue E of the Bogoliubov Hamiltonian written in representation $(\hat{\boldsymbol{\psi}}, R_s\hat{\boldsymbol{\psi}}^\dagger)^{\mathrm{T}}$. Then the Schrodinger equation can be written as a set of coupled equations:

$$(F - E)u_E = -G'v_E \text{ and } (F_T + E)v_E = -G'^\dagger u_E \quad (4.45)$$

By multiplying first term with $F_T + E$ and second term by $F - E$ one gets

$$\left[F_TF - G'G'^\dagger - E^2 + E(F - F_T)\right] u_E = -[F_T, G']v_E$$
$$\left[FF_T - G'^\dagger G' - E^2 + E(F - F_T)\right] v_E = -[F, G'^\dagger]u_E$$

where $F_T = TFT^{-1}$ is the time reversed expression of F. Spin 1 Kane Mele model is time-reversal invariant, i.e. $F_T = F$ and has the pairing term $G' = R_sG = \bar{\rho}U_s\mathrm{diag}(1, 1, 1)$, which commutes with F and F_T. Thus for Spin-1 Kane-Mele model the equations from above reduce to

$$\left[F^2 - G^2 - E^2\right] u_E = \left[F^2 - G^2 - E^2\right] v_E = 0$$

Since F^2 and G^2 are Hermitian operators, the eigenvalues E^2 have to be real. This implies that either E is real or either E is pure imaginary, i.e. $\mathrm{Re}E = 0$ when $\mathrm{Im}E \neq 0$.

To sum up, time-reversal symmetry guarantees $F_T = F$. However, in order to have $[F_T, G'] = 0$ for a spin rotationally and S_z invariant system, it might be that G' has to be made out of Casimir $\mathbf{S}^2 = S_x^2 + S_y^2 + S_z^2 = 2$ and S_z operators (notice that $G' = \bar{\rho}U_s\mathbf{1} = \bar{\rho}U_s\mathbf{S}^2/2$). This implies some restrictions on the pairing term G, that require G to be a combination of S_zR_s and $\mathbf{S}^2R_s = 2R_s$. Sublattice symmetry can be regarded as a symmetry in a quasi-spin space, meaning similar ideas as to spin symmetry may apply.

4.6 Conclusion and outlook

In this chapter the possibility of driving a two-dimensional topological interacting lattice system onto a phase with dynamically unstable edge states while bulk states remaining stable has been described. Such a mechanism allows for the topological edge states to dominate the dynamics of the boson lattice model. A quench in the quadratic Zeeman term has been shown to lead to the population of the edge states of a spin-1 Kane-Mele model, which resulted in an exponential increase in spin current at the edge of the system. The results, however, give an accurate insight into the topological dynamics only in the short-time scale of the evolution. Due to an exponentially fast growth of the edge-state population the mean-field approximation used in this chapter is expected to break down once the Bogoliubov fluctuations become comparable to the ground state population. How the system behaves in the longer run is an interesting question to ask. We will partially address this question in Chapter 6, where Truncated Wigner Approximation will be used to find the long time evolution of the SSH model. Also, the assumption of open boundary conditions mimicking the boundary behaviour in solids has been assumed. Although experimental techniques creating sharp potentials in ultracold atoms experiments are being developed these are not very common yet. The harmonic potential which is commonly adopted in cold atoms experiments is known to obscure the band structure of the non-interacting models used in optical lattice experiments. Therefore ways to overcome these challenges can be of a major experimental interest. One such possibility related to the Kane-Mele model is described in the next chapter of this thesis. Other aspects of future work could include a deeper investigation of the symmetries involved in protecting boson states from becoming dynamically unstable. Based on this it would be interesting to know what are the quench effects on the dynamics of other topological models of interacting bosons.

5

Edge states in a harmonic potential

Unlike solids, ultracold atoms are typically confined by a harmonic trapping potential. Theoretical studies suggest the presence of a confining potential can modify both the bulk and edge energy spectrum significantly, leading not only to a change in group velocity of edge modes but also to an emergence of additional edge states [82, 83], their disappearance [84], or localisation and a shrinking of the bulk region [83, 85]. The influence of the harmonic trap on the band structure and its topology is therefore of significant importance. This chapter is dedicated to the influence of the harmonic trap on the band structure and its topology.

Let us first emphasise the importance of the sharp boundaries for the edge manifestation of topological phenomena. Consider a non-interacting Kane-Mele model in a the strip geometry (see Fig. 5.1). We keep the lattice periodicity along the $\mathbf{a}_1$ primitive lattice vector by imposing closed boundary conditions, while considering three cases of boundary conditions in the perpendicular direction: closed boundary condition, open boundary condition

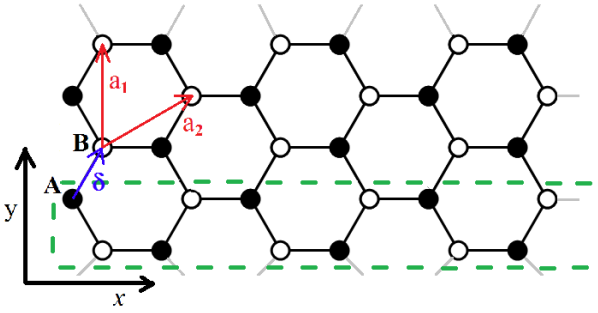

Figure 5.1: Honeycomb lattice structure, determined by the primitive lattice vectors $\mathbf{a}_1$ and $\mathbf{a}_2$ of length a. Closed and open circles denote the triangular sublattice sites A and B respectively. We consider strip geometry with closed boundary conditions in the y-direction, and a harmonic potential in the x-direction.

(box/hard-wall potential) and external harmonic potential given by:

$$\hat{V}_\omega = \sum_j \frac{M\omega^2 x_j^2}{2}\hat{\rho}_j, \tag{5.1}$$

where ω is the confining frequency, $\hat{\rho}_j$ is the local number operator and x_j is the location of the j-th site with respect to the centre of the trap taken along the x-direction as depicted in Fig. 5.1. The energy spectra corresponding to the three cases of boundary conditions are depicted in Fig. 5.2. When closed boundary conditions are applied only extended (bulk) modes exists and no mid-gap states are present. An open boundary condition (box/hard wall potential) forces the appearance of topological edge states that cross the gap. These states are a consequence of topological bulk-boundary correspondence. The presence of a harmonic potential, however, changes the energy spectrum considerably: the density of extended (bulk) states is reduced, and the difference between localised and extended states becomes obscure. In that sense the manifestation of topological phenomena in systems with soft boundaries or in presence of smooth potentials can be obscured. The aim of this chapter is to show that the interactions of boson spinor condensates can facilitate the emergence of topological edge-states in the presence of a harmonic potential. The current chapter also aims to answer how the topological edge states manifest in the presence of a harmonic confinement, and how these states differ from the edge-states of a system with idealised open boundary

conditions. The role of mean field interactions in the Haldane boson model was also considered in [86] where it was shown that the bulk gap can close when the harmonic trap is taken into account. Possible ways of overcoming these difficulties include inducing topological interfaces [5, 87] and creating a confinement sharper than harmonic [32–34, 83]. Creation of such trapping potentials represents a separate challenge and cost for experimental setup. The results obtained in this chapter suggest boson topological edge-states reassembling the ones from solids, i.e. with open boundary conditions, could still be achievable in typical experimental setups with harmonic confinement potentials.

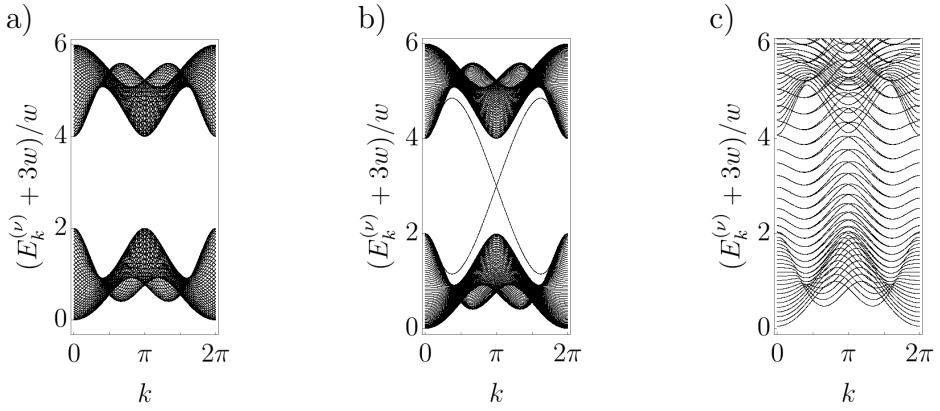

Figure 5.2: Comparison of energy spectra of non-interacting Kane-Mele model in closed boundary condition (a), open boundary condition (hard-wall boundaries) (b) and in a harmonic potential (only the lowest energy bands are shown) (c). Here $\lambda = w/2$ and $M\omega^2 a^2 = 0.02w$. The total number of sites in the unit cell strip in x-direction is 200.

5.1 Screening effect of the confining potential in trapped spin-1 Bose condensates

Non-trivial topological properties can exist in models described by just quadratic Hamiltonians on a lattice $\hat{\mathcal{H}}_{\text{latt}} = \sum_{ij} \hat{\mathbf{\Psi}}_i^\dagger \hat{\mathcal{H}}_{\text{latt}}^{ij} \hat{\mathbf{\Psi}}_j$, where $\hat{\mathbf{\Psi}}_j$ is the annihilation operator for a particle at site j and $\hat{\mathcal{H}}_{\text{latt}}^{ij}$ is the Hamiltonian lattice matrix. $\hat{\mathbf{\Psi}}_j$ can carry more indices corresponding to other quantum numbers such as spin. In this chapter atoms of spin-1 on a two dimensional lattice are considered. We use same setup as in the previous chapters where we introduce spin rotationally invariant interaction term $\hat{\mathcal{H}}_{\text{int}}$, a quadratic Zeeman

term $\hat{\mathcal{H}}_Z$, and an external confining potential $\hat{V}_\omega$. The total Hamiltonian is:

$$\hat{\mathcal{H}} = \hat{\mathcal{H}}_{\rm latt} + \hat{\mathcal{H}}_{\rm int} + \hat{\mathcal{H}}_Z + \hat{V}_\omega - \mu \sum_j \hat{\rho}_j, \tag{5.2}$$

where μ is the chemical potential and $\hat{\rho}_j = \hat{\mathbf{\Psi}}_j^\dagger \hat{\mathbf{\Psi}}_j$ is the local number operator at site j. All other notations correspond to the ones adopted in the previous chapters. We consider regimes of low temperatures, such that the boson atoms condense onto the ground state described by the wave-function $\bar{\mathbf{\Psi}}$. We then treat the interactions at mean-field level. For sufficiently large and positive q_Z, the ground state is a polar state where $\bar{\mathbf{S}}_j = \bar{\Psi}_j^\dagger \mathbf{S} \bar{\Psi}_j = 0$ and $\bar{\mathbf{\Psi}}_j = (0, \sqrt{\bar{\rho}_j}, 0)^T$. For a slowly varying confining potential, much slower than the lattice characteristic length scale, the ground state population extends over a considerable number of lattice sites. Provided the density and spin fluctuations, $\delta\hat{\rho} = \hat{\rho} - \bar{\rho}$ and $\delta\hat{\mathbf{S}} = \hat{\mathbf{S}} - \bar{\mathbf{S}}$, are small, the fluctuations about the ground state $\hat{\boldsymbol{\psi}} = \hat{\Psi} - \bar{\Psi}$ up to quadratic order are described by the Bogoliubov-de Gennes (BdG) Hamiltonian:

$$\begin{aligned}\hat{\mathcal{H}}_{\rm B} = &\sum_{ij} \hat{\boldsymbol{\psi}}_i^\dagger \left(\mathcal{H}_{\rm latt}^{ij} - \delta^{ij} \bar{\mathcal{H}}_{\rm latt} \right) \hat{\boldsymbol{\psi}}_j + \sum_j V_{{\rm eff},j} \hat{\boldsymbol{\psi}}_j^\dagger \hat{\boldsymbol{\psi}}_j + \sum_j q_Z \hat{\boldsymbol{\psi}}_j^\dagger S_z \hat{\boldsymbol{\psi}}_j \\ &+ \frac{U}{2} \delta\hat{\rho}_j^2 + \frac{U_S}{2} \delta\hat{\mathbf{S}}_j^2,\end{aligned} \tag{5.3}$$

where we have introduced the mean kinetic energy per particle in the condensate $\bar{\mathcal{H}}_{\rm latt} = \sum_{i,j} \bar{\mathbf{\Psi}}_i^\dagger \, \mathcal{H}_{\rm latt}^{ij} \bar{\mathbf{\Psi}}_j / \sum_{j'} \bar{\rho}_{j'}$ and the effective potential:

$$V_{{\rm eff},j} = M\omega^2 x_j^2/2 + \bar{\mathcal{H}}_{\rm latt} + U\bar{\rho}_j - \mu. \tag{5.4}$$

Prior to evaluating the fluctuation modes of the BdG Hamiltonian, we first discuss the effect of screening of confining potential. The ground state density profile $\bar{\Psi}$ is determined by the time-independent Gross-Pitaevskii equation:

$$\sum_j \left(\mathcal{H}_{\rm latt}^{ij} - \bar{\mathcal{H}}_{\rm latt} \delta^{ij} + V_{{\rm eff},i} \delta^{ij} \right) \bar{\Psi}_j = 0. \tag{5.5}$$

At large distances from the centre of the trap the population density $\bar{n}_j$ vanishes and the confining potential takes the leading role in $V_{\rm eff}$. On the

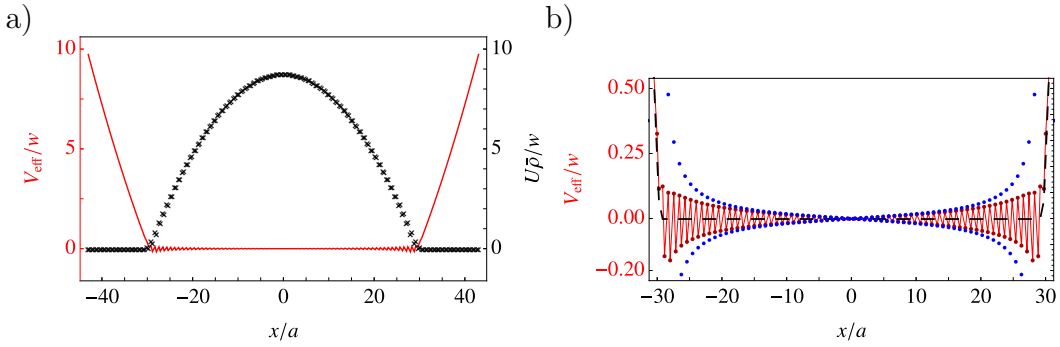

Figure 5.3: a) The effective potential $V_{\rm eff}$ (solid lines; red) and the density profile of the ground state $U\bar{\rho}$ (cross marks; black). These quantities are obtained numerically and are in excellent agreement with the Thomas-Fermi profile. b) The zoomed-in part of the effective potential shown in figure (a). Red connected dots correspond to $V_{\rm eff}$ computed numerically, while blue dots correspond to one iteration of the recursive analytical expression (5.8) with the initial value $V_{\rm eff} = 0$. The black dashed line gives the Thomas-Fermi profile. Here $\lambda = w/2$, $M\omega^2 a^2 = 0.02w$ and $UN_{\rm str} = 800w$, where $N_{\rm str}$ is the total number of bosonic particles in a strip denoted by the (green) dashed lines in Fig. 5.1. The Thomas-Fermi radius is $x_{\rm TF} \approx 30a$.

other hand, for distances closer to the centre of the trap, the ground state population is larger. Under the Thomas Fermi approximation for the mean-field density, applicable when $\sqrt{M\omega^2 a^2 w}/U \max_j \bar{\rho}_j$, the effective potential $V_{\rm eff}$ indeed will vanish identically inside the Thomas-Fermi radius given by $x_{TF} = \sqrt{2(\mu - \tilde{\mathcal{H}}_{\rm latt})/(M\omega^2)}$. Shown in Fig.5.3 is the effective potential which is computed numerically and demonstrates the statements above. Such a screening occurs in standard scalar BECs. In this sense, interactions contribute to the screening of the harmonic trap inside the Thomas Fermi region. Deviations from perfect Thomas-Fermi screening can be seen as oscillations on the scale of the lattice spacing in the effective potential $V_{\rm eff}$. These are due to variations of the harmonic potential within the unit cell that are not perfectly screened. Although the magnitude of these variations is small in comparison to the band width, we retain them in our numerical computation. The origin of small unscreened variations in $V_{\rm eff}$ can be understood in more details from the Gross-Pitaevskii equation (5.5) and the expression for the effective potential (5.4). Notice that inside the Thomas-Fermi radius the particle density does not vanish, i.e. $\bar{\Psi}_j \neq 0$. With this assumption we divide

equation (5.5) by $\bar{\Psi}_i$ to obtain

$$V_{\text{eff},i} = \bar{\mathcal{H}}_{\text{latt}} - \sum_j \mathcal{H}^{ij}_{\text{latt}} \frac{\bar{\Psi}_j}{\bar{\Psi}_i}. \tag{5.6}$$

The above relation allows for small unscreened fluctuations of V_{eff} inside the Thomas-Fermi radius. This is due to the second term in the right hand-side of (5.6). This term is not constant and can fluctuate due to variation of the ground state function within the nearest neighbours. However, in the Thomas-Fermi regime the fluctuations due to the lattice Hamiltonian $\mathcal{H}^{ij}_{\text{latt}}$ are small in comparison to the band and gap widths. One can partly reproduce these oscillations. By introducing the particle density $\bar{\rho}_j = |\bar{\Psi}_j|^2$ one can write $\bar{\Psi}_j/\bar{\Psi}_i = \sqrt{\bar{\rho}_j/\bar{\rho}_i}\exp(i\Delta\theta_{i,j})$, where $\Delta\theta_{i,j}$ denotes the phase difference of the ground-state wave-function at sites j and i. Since V_{eff} and $\bar{\mathcal{H}}_{\text{latt}}$ are real the phase difference $\Delta\theta_{i,j}$ should not contribute to (5.6). Indeed, due to time-reversal symmetry the ground-state wave-function $\bar{\Psi}_j$ can be chosen to be real. Thus one has

$$V_{\text{eff},i} = \bar{\mathcal{H}}_{\text{latt}} - \sum_j \mathcal{H}^{ij}_{\text{latt}} \sqrt{\frac{\bar{\rho}_j}{\bar{\rho}_i}}. \tag{5.7}$$

We next express $\bar{\rho}_j$ from equation defining V_{eff} (5.4), and plug it into equation (5.7):

$$V_{\text{eff},i} = \bar{\mathcal{H}}_{\text{latt}} - \sum_j \mathcal{H}^{ij}_{\text{latt}} \sqrt{1 - \frac{V_{\omega_j} - V_{\omega_i} - V_{\text{eff},j} + V_{\text{eff},i}}{\mu - \bar{\mathcal{H}}_{\text{latt}} - V_{\omega_i} + V_{\text{eff},i}}}. \tag{5.8}$$

Notice that the above relation is exact inside the Thomas-Fermi radius. Next, we regard (5.8) as a recursive relation for V_{eff}. In what follows we compute the value of V_{eff} by plugging $V_{\text{eff}} = 0$ into the right-hand side of the relation (5.8). Then the obtained value we plug back into the right-hand side again, and repeat this procedure for a couple of times. The results after one iteration are shown in Fig. 5.3b. There is excellent agreement with the exact value of V_{eff} in the middle of the trap. One can obtain a better approximation by including more terms in the expansion. However, this procedure gives

poor convergence near the Thomas-Fermi radius. These results complement the screened value of the effective potential by taking into account the small variations within the nearest-neighbour hopping.

5.2 Bogoliubov excitations and topological bulk-boundary correspondence in a harmonic potential

We now turn to the the discussion of the fluctuation spectrum of the BdG Hamiltonian (5.3), which is the central focus of this chapter. The spin-±1 components in (5.3) decouple from the spin-0 ones in $\hat{\mathcal{H}}_B$ due to S_z symmetry. The density fluctuation term in (5.3) carries only spin-0 components $\delta\hat{\rho}_j^2 = \bar{\rho}_j(\hat{\psi}_{j,0}^\dagger\hat{\psi}_{j,0} + \hat{\psi}_{j,0}\hat{\psi}_{j,0} + \text{H.c.})$, while the spin fluctuation term couples the spin-±1 components: $\delta\hat{\mathbf{S}}_j^2 = \bar{\rho}_j(\hat{\psi}_{j,+1}^\dagger\hat{\psi}_{j,+1} + \hat{\psi}_{j,-1}^\dagger\hat{\psi}_{j,-1} + \hat{\psi}_{j,+1}\hat{\psi}_{j,-1} + \hat{\psi}_{j,+1}^\dagger\hat{\psi}_{j,-1}^\dagger + \text{H.c.})$. Because, in typical condensates, the spin-spin interaction is much smaller than the density-density interaction (for instance, for ^{87}Rb, U_S is two orders of magnitude smaller than U), the Hamiltonian describing the ±1 components will be, to a good approximation, translationally invariant within the Thomas-Fermi radius. An interface is then encountered around $x = x_{TF}$, where the effective potential rises (Fig. 5.3) and the system loses its translational invariance. Similar approximations have previously been employed to simplify the computation of the spatial structure of parametrically amplified spin modes [88]. In Fig. 5.4 the full energy spectrum for Bogoliubov excitations is depicted. The spin-0 components exhibit a linear dispersion at $k = 0$ and $k = 2\pi$ which is due to Goldstone modes. Unlike spin-0 components, a reconstruction of the bulk energy bands of the Kane-Mele model is observed for the spin-±1 components. A gap in the energy spectrum is also distinguishable, with numerous bands crossing it. These band correspond to the edge-states, and differ from the situation of the idealised open boundary conditions. Therefore, questions related to how these bands reflect topological bulk-boundary correspondence in the presence of a harmonic potential have to be addressed. To better understand the effect of trap screening on the manifestation of topological edge-modes, we give an effective description of the edge state emergence around the screening

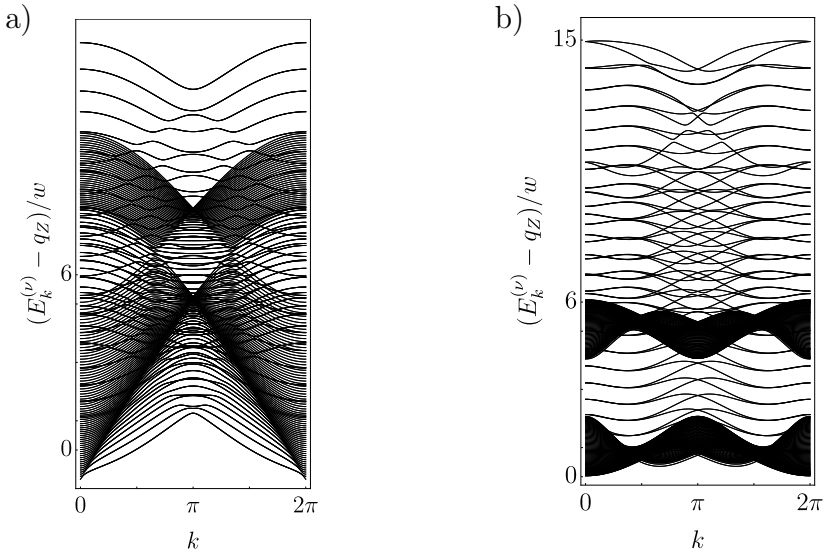

Figure 5.4: Energy spectrum of Bogoliubov excitations for spin-0 (a) and spin-± 1 (b) components. A phonon linear dispersion due to Goldstone mode is seen at $k = 0$ and $k = 2\pi$ in (a). b) Energy spectrum for spin-± 1 excitations. A linear dispersion due to Goldstone mode is clearly seen at $k = 0$ and $k = 2\pi$. Here $\lambda = w/2$, $M\omega^2 a^2 = 0.02w$ and $UN_{\rm str} = 800w$, where $N_{\rm str}$ is the total number of bosonic particles in a strip denoted by the (green) dashed lines in Fig. 5.1.

boundaries outside the Thomas-Fermi radius below.

Topological edge-state manifestation in a harmonic potential

Although, we consider the spin-1 Kane-Mele model in this chapter, we give a fairly general technique of computing states in a soft potential in what follows. Since the edge states are composed entirely of ± 1 components, we will restrict our attention to these modes. Outside of the Thomas Fermi radius, we may neglect the last two terms in (5.3) as the mean-field particle density vanishes in this region. In particular, outside of the Thomas-Fermi radius, pairing terms are absent. We assume the boundary region to be sufficiently small in comparison to the lattice constant induced by the optical lattice potential and will discuss the effect of these restrictions later. Note that outside the Thomas-Fermi radius, the effective potential reduces to the trapping potential, and interactions are unimportant since the mean-field density vanishes in this region. As a result the spin components decouple

and without loss of generality we focus around one spin component. Let k denote the wave number along the $\mathbf{a}_1$ periodic direction, while n label the unit cells along the $\mathbf{a}_2$ lattice vector. The two sublattices of our model are specially separated and consequently the corresponding atoms at the same n-th unit cell experience a different magnitude of the confining potential. While the excitations related to one sublattice experience an effective potential $\mathcal{V}(n)$, the excitations related to the other sublattice experience a potential $\mathcal{V}(n+s)$, where s accounts for the relative lattice separation. For reasons of computational convenience we have considered the trapping potential to be oriented in the direction perpendicular to the primitive lattice vector $\mathbf{a}_1$. Thus the excitations within the sublattice A experience a harmonic potential $\mathcal{V}(n) = M\omega^2 n^2(\mathbf{a}_2 \cdot \hat{\mathbf{x}} - x_c)^2/2 + q_Z - \mu$ centred at position $x_c = (\mathbf{a}_2 \cdot \hat{\mathbf{x}})(N_{\rm str} + 1 + s)/2$ and shifted by the chemical potential μ and quadratic Zeeman coupling q_Z, where $2N_{\rm str}$ is the total number of sites in a unit cell strip highlighted in Fig. 5.1. The sublattice B site are displaced by a vector $\boldsymbol{\delta}$ and consequently experience a slightly different magnitude of the harmonic trap $\mathcal{V}(n+s)$. The value of the shift s accounts for the displacement $\boldsymbol{\delta}$ and is related to the primitive lattice vectors $\mathbf{a}_1$ and $\mathbf{a}_2$. This leads to a general expression for the relative separation s:

$$s = \frac{\mathbf{a}_1^2(\boldsymbol{\delta} \cdot \mathbf{a}_2) - (\mathbf{a}_1 \cdot \mathbf{a}_2)(\boldsymbol{\delta} \cdot \mathbf{a}_1)}{\mathbf{a}_1^2\mathbf{a}_2^2 - (\mathbf{a}_1 \cdot \mathbf{a}_2)^2}. \tag{5.9}$$

For the regular hexagonal lattice $s = 1/3$. The energy spectrum of the system outside of the Thomas-Fermi radius is given by the eigenvalues E_k of a difference equation of the form:

$$\sum_{n'} H_{k,n-n'}\mathbf{\Phi}_{k,n'} + V_n\mathbf{\Phi}_{k,n} = E_k\mathbf{\Phi}_{k,n}, \tag{5.10}$$

where $H_{k,n}$ and $V_n = \mathrm{diag}(\mathcal{V}(n), \mathcal{V}(n+s))$ are 2×2 matrices (the treatment can also be generalised to larger matrices). In (5.10) $H_{k,n} = H^\dagger_{k,-n}$ follows from $\mathcal{H}^{ij}_{\rm latt}$ while V_n follows from the effective potential. We next introduce the variable $\hat{\varphi}$ which is canonically conjugate to $\hat{n}$: $[\hat{n}, \hat{\varphi}] = i$. With this,

(5.10) can be rewritten as

$$(H_{k,\hat{\varphi}} + V_{\hat{n}})\,|\mathbf{\Phi}_k\rangle = E_k\,|\mathbf{\Phi}_k\rangle\,, \tag{5.11}$$

where we use the notation $\langle n|\,\mathbf{\Phi}_k\rangle = \mathbf{\Phi}_{k,n}$ and $\langle\varphi|\,\mathbf{\Phi}_k\rangle = \mathbf{\Phi}_{k,\varphi}$, and note that $\mathbf{\Phi}_{k,\varphi}$ must be 2π periodic in φ. The eigenvalues of $H_{k,\hat{\varphi}}$ give the bulk band dispersions in the non-interacting limit. We next perform a unitary transformation: $\tilde{H}_{k,\hat{\varphi}} = \mathcal{U}^{\dagger}_{\hat{\varphi}} H_{k,\hat{\varphi}} \mathcal{U}_{\hat{\varphi}}$, $\tilde{V}_{\hat{n}} = \mathcal{U}^{\dagger}_{\hat{\varphi}} V_{\hat{n}} \mathcal{U}_{\hat{\varphi}}$, and $|\mathbf{\Phi}_k\rangle = \mathcal{U}_{\hat{\varphi}} \left|\tilde{\mathbf{\Phi}}_k\right\rangle$ where $\mathcal{U}_{\hat{\varphi}} = \mathrm{diag}(1, e^{is\hat{\varphi}})$. This transformation is useful because it makes $\tilde{V}_{\hat{n}}$ proportional to the identity matrix: $\tilde{V}_{\hat{n}} = \mathcal{V}(\hat{n})\mathbb{1}$.

We expand $\tilde{V}_{\hat{n}}$ about a particular location $\bar{n}$ and keep only the linear term, which is a good approximation outside of the Thomas Fermi radius (see Fig. 5.3), to obtain $\tilde{V}_{\hat{n}} = \tilde{V}_{\bar{n}} + \gamma_{\bar{n}}\mathbb{1}(\hat{n} - \bar{n})$ where $\gamma_{\bar{n}} = \tilde{V}'(\bar{n})$. We search for solutions localized near $\bar{n}$. In the φ basis, (5.10) then becomes

$$i\gamma_{\bar{n}}\partial_{\varphi}\tilde{\mathbf{\Phi}}_k = (E_k - \tilde{H}_{k,\varphi} - \tilde{V}_{\bar{n}})\tilde{\mathbf{\Phi}}_k,$$

and the solution is readily found to be

$$\tilde{\mathbf{\Phi}}_{k,\varphi} = e^{-i\left(\bar{n} + \frac{E_k - \mathcal{V}(\bar{n})}{\gamma_{\bar{n}}}\right)\Delta\varphi} \mathcal{P} e^{\frac{i}{\gamma_{\bar{n}}}\int_{\varphi_0}^{\varphi} d\varphi'\, \tilde{H}_{k,\varphi'}} \tilde{\mathbf{\Phi}}_{k,\varphi_0}. \tag{5.12}$$

Here $\mathcal{P}$ is the path ordering operator for φ and $\Delta\varphi = \varphi - \varphi_0$ and φ_0 can take arbitrary value.

For the case when $\gamma_{\bar{n}}$ is significantly smaller than the eigenvalue spacing of $\tilde{H}_{k,\varphi}$, which corresponds to the bulk band gap, the adiabatic approximation can be used. To do so, we introduce the 'instantaneous' eigenbasis: $\tilde{H}_{k,\varphi}\tilde{\boldsymbol{\phi}}^{(\nu)}_{k,\varphi} = \varepsilon^{(\nu)}_{k,\varphi}\tilde{\boldsymbol{\phi}}^{(\nu)}_{k,\varphi}$ where ν labels the eigenvector/eigenenergies and let $\boldsymbol{\phi}^{(\nu)}_{k,\varphi} = \mathcal{U}_{\varphi}\tilde{\boldsymbol{\phi}}^{(\nu)}_{k,\varphi}$. Here, $\varepsilon^{(\nu)}_{k,\varphi}$ are the bulk eigenstates of the non-interacting infinite system. Invoking the adiabatic approximation, and transforming back

to the original variables, one finds

$$\begin{aligned}\mathbf{\Phi}_{k,\varphi} = e^{-i\left(\bar{n}+\frac{E_k-\mathcal{V}(\bar{n}+\frac{s}{2})}{\gamma_{\bar{n}}}\right)\Delta\varphi} \\ \times \sum_{\nu} e^{i\int_{\varphi_0}^{\varphi} d\varphi' \left(\frac{\varepsilon^{(\nu)}_{k,\varphi'}}{\gamma_{\bar{n}}}+A^{(\nu)}_{k,\varphi'}-\frac{sZ^{(\nu)}_{k,\varphi'}}{2}\right)} \left[\boldsymbol{\phi}^{(\nu)\dagger}_{k,\varphi_0}\mathbf{\Phi}_{k,\varphi_0}\right]\boldsymbol{\phi}^{(\nu)}_{k,\varphi}\end{aligned} \tag{5.13}$$

where $A^{(\nu)}_{k,\varphi} = i\boldsymbol{\phi}^{(\nu)\dagger}_{k,\varphi}\partial_\varphi\boldsymbol{\phi}^{(\nu)}_{k,\varphi}$ is the Berry connection and $Z^{(\nu)}_{k,\varphi} = \boldsymbol{\phi}^{(\nu)\dagger}_{k,\varphi}\sigma_z\boldsymbol{\phi}^{(\nu)}_{k,\varphi}$ (σ_z is a Pauli matrix).

Requiring $\mathbf{\Phi}_{k,\varphi}$ to be 2π periodic in φ, enables one to determine the allowable energies E_k entering (5.13). Labelling these as $E^{(\bar{n}\nu)}_k$, one finds

$$E^{(\bar{n}\nu)}_k = \mathcal{V}\left(\bar{n}+\frac{s}{2}\right) + \frac{1}{2\pi}\int_0^{2\pi} d\varphi \left(\varepsilon^{(\nu)}_{k,\varphi} + \gamma_{\bar{n}}A^{(\nu)}_{k,\varphi} - \frac{s\gamma_{\bar{n}}}{2}Z^{(\nu)}_{k,\varphi}\right). \tag{5.14}$$

Different values of $\bar{n}$ correspond to edge states localized at different places along the x-direction. This expression is remarkable in that it expresses the edge state dispersion purely in terms of the external potential and basic quantities of the bulk system. The (integer) Chern numbers of the bulk system are given by

$$\mathcal{C}_\nu = \frac{1}{2\pi}\int_0^{2\pi} d\varphi \int_0^{2\pi} dk\Omega^{(\nu)}_{k,\varphi}, \tag{5.15}$$

where $\Omega^{(\nu)}_{k,\varphi} = i\left(\partial_k\phi^{(\nu)\,\dagger}_{k,\varphi}\partial_\varphi\phi^{(\nu)}_{k,\varphi} - \partial_\varphi\phi^{(\nu)\,\dagger}_{k,\varphi}\partial_k\phi^{(\nu)}_{k,\varphi}\right)$ is the Berry curvature. Using this and (5.14), one sees that the edge state band energies change by $\gamma_{\bar{n}}\mathcal{C}_\nu$ as the one-dimensional Brillouin zone is traversed:

$$\Delta E^{(\bar{n}\nu)} = E^{(\bar{n}\nu)}_{k=2\pi} - E^{(\bar{n}\nu)}_{k=0} = \gamma_{\bar{n}}\mathcal{C}_\nu. \tag{5.16}$$

We support our results by performing numerical computations. We use imaginary time evolution to solve the Gross-Pitaevskii equation (5.5) for the ground state in the Thomas-Fermi regime. We then numerically compute the collective spin excitations and our comparison with analytical result (5.14) shows excellent agreement (see Fig. 5.5). Deviations from (5.14) can be con-

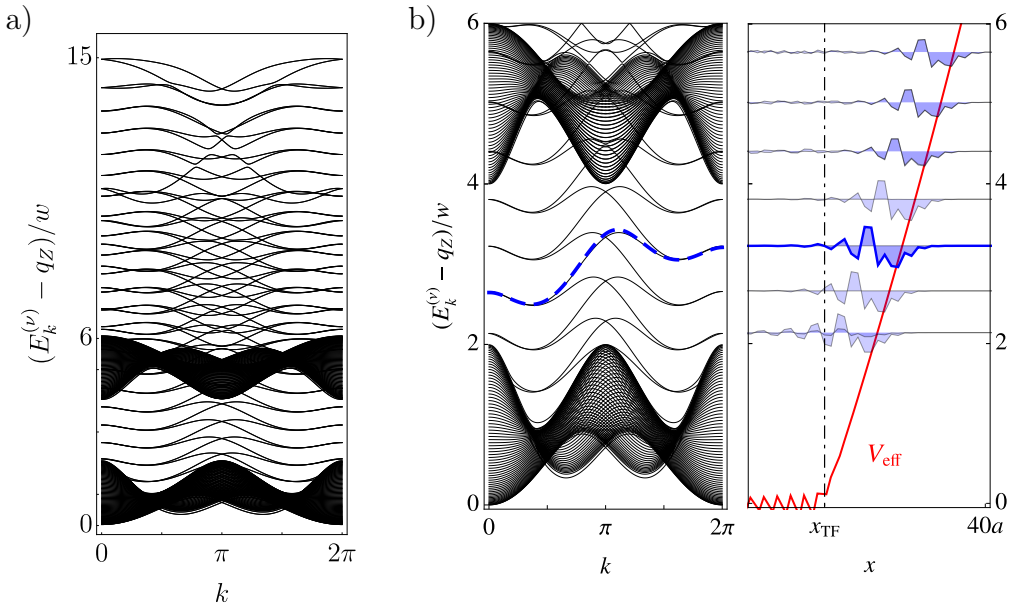

Figure 5.5: a) The energy spectrum corresponding to the spin-$1(-1)$ excitations. b) Left: The lower part of the energy spectrum corresponding to the spin-$1(-1)$ excitations. The solid lines correspond to numerical results, while the dashed line corresponds to the analytical expression (5.14) for a particular mode. Right: The effective potential in units of w near the Thomas-Fermi radius x_{TF} (red) and the wave functions of the eigenmodes in arbitrary units at $k = 2\pi$ (blue). Here $\lambda = w/2$, $m\omega^2 = 0.02w$ and $UN = 1600w$, where N is the total number of atoms. The total number of sites in a unit cell strip in x-direction is 200.

siderable for the edge states with energies close to the corresponding bulk band from which they emerge. For these energy levels the overlap between states (5.13) and bulk states cannot be ignored. The focus of this work however, lies in describing emergence of topological edge states of energies well within the gap and/or outside the bulk bands. Nevertheless, we point out that our method can be improved by requiring corresponding matching conditions at the screening radius and taking higher order corrections in $\gamma_{\bar{n}}$. We also find that the degeneracy of the edge states changes depending on their energy. As can be seen in Fig. 5.5 the chiral edge states can pass through a given energy level several times. However, the difference between the number of right and left movers, N_R^ν and N_L^ν correspondingly, at the same energy level is fixed by the topological structure of the bulk states: $N_R^\nu - N_L^\nu = C_\nu$. This is a direct indication of the topological nature of the bulk states and a consequence of the bulk-boundary correspondence [11, 12].

5.3 Conclusions and outlook

Despite harmonic confinement being known for obscuring observation of topological edge-states we have shown that interactions can facilitate the emergence of these states in topological lattices populated by spinor Bose condensates. In the Thomas-Fermi regime sharp boundaries emerge due to the screening of the harmonic trap inside the Thomas-Fermi radius. These states carry information about the lattice topology inside the screening radius, which is reflected in the analytical expression (5.14) for the edge-state dispersion. We would like to point out that despite the presence of a harmonic potential the bulk energy spectrum for the spin-± 1 components, which is depicted in Fig. 5.4(b), reconstructs the bulk energy band structure of the non-interacting model (Fig. 5.2(b)). This is different from the energy spectrum of the spin-0 components, which are depicted in Fig. 5.4(a), and is due to the spin interaction strength U_s being weaker than the density interaction strength U. The outlined results suggest that non-interacting topological lattice models with sharp boundaries can effectively be simulated in optical lattice experiments with interacting spinor condensates using conventional harmonic confinement. Unlike alternative methods that require creating box-like potentials [33, 34] or topological interfaces [5, 87], the mechanism described in this chapter has the advantage of relying on already established experimental facilities.

It is also worth mentioning how the results presented in this chapter differ from the topological manifestation of the edge states when hard-wall boundaries are considered. In particular, a common feature of 2D topological insulators is that the energy of the topological edge states connects the bulk energy bands, the way it is depicted for the non-interacting Kane-Mele model in Fig. 5.2(b). This feature seems to be altered in the presence of a harmonic trap (see Fig. 5.2(c), Fig. 5.4 and Fig. 5.5). The results (5.14) and (5.16) can be used to explain how this altering occurs. The energy dispersion of the edge states experiences a jump (5.16) while crossing the Brillouin zone, which is smaller than the gap and is determined by the steepness of the harmonic potential $\gamma_{\bar{n}}$ at the Thomas-Fermi radius. One can therefore relate

the number of edge states crossing the gap using this result, by dividing the gap energy by the energy jump of a single edge mode within the gap.

All results presented in this chapter are valid both for antiferromagnetic ($U_s > 0$) and ferromagnetic ($U_s < 0$) interactions, while the scheme of evaluating edge-states in the presence of a harmonic potential presented in this chapter can be generalised to more complicated lattice models and other soft external potentials.

6

Time evolution of the quenched spinor condensate for longer times

In Chapter 4 the time evolution of a quenched spinor condensates has been discussed in the context of the edge-state manifestation of boson topological lattice models. It was shown that right after the quench topological edge-states to be populated exponentially fast and to dominate the dynamics of the system. However, the Bogoliubov treatment that was used is valid only for short time scales for which the number of atoms excited in the unstable modes is small compared to the total atom number. Intuitively one cannot expect an everlasting exponentially fast population of edge states, nor that the edge-state dynamics would not be affected by the particle redistribution across the entire lattice. This chapter is devoted to the investigation of the time evolution of the quenched systems introduced in Chapter 4 beyond the Bogoliubov treatment. This short chapter utilises the Truncated Wigner Approximation (TWA), and includes only preliminary results of ongoing research. Nevertheless some insights into the long-time behaviour can

be gained from the results presented in this chapter.

6.1 Introduction

Time evolution of the expectation value of an operator $\hat{\Omega}$, which could be density or current, can be formally written as [89]:

$$\langle \hat{\Omega}(t) \rangle = \mathrm{Tr}\left[\hat{\rho} \mathcal{T} e^{i \int_0^t d\tau \ \hat{H}(\tau)} \hat{\Omega}(t) e^{-i \int_0^t d\tau \ \hat{H}(\tau)} \right], \tag{6.1}$$

where $\hat{\rho}$ is the time independent density operator, $\mathcal{T}$ stands for time ordering, and $\hat{\mathcal{H}}$ is the Hamiltonian of the system. The operators $\hat{\Omega}$, $\hat{\mathcal{H}}$ and $\hat{\rho}$ can be expressed in terms of boson creation and annihilation operators. Although the expression (6.1) is compact, its evaluation is rather difficult. Most often numerical evaluation of the expectation values (6.1) cannot be avoided for systems out of equilibrium, and certain approximate treatments are required. This chapter makes use of the Truncated Wigner Approximation [89]. It is a method that can accurately describe the system when it closely follows the dynamics of a semiclassical path. The contribution of quantum fluctuations in this case is considered perturbatively. Other similar methods include Keldysh formalism [90]. One important difference of the Truncated Wigner Approximation from the Keldysh formalism is that the latter often considers interaction strength perturbatively [89, 90]. The quench mechanism introduced in Chapter 4 does not involve quenching the interaction strength, but rather relies on an abrupt change of the ground state through quenching the quadratic Zeeman term. In order to describe this kind of quenched dynamics we prefer to keep the interaction terms fixed and not treat them perturbatively. Also, the experiments with ultracold atoms are performed at very low temperatures (of the order of micro-Kelvin and below). The initial state of the system that precedes the quench, a Bose-Einstein condensation, is well described by a semiclassical equation, the Gross-Pitaevskii equation. Based on the above, we treat the quenched dynamics of the systems using the Truncated Wigner Approximation. The method gives the following approximate

expression for the evaluation of the relation (6.1):

$$\langle\hat{\Omega}(t)\rangle = \int d\psi^* d\psi W(\psi,\psi^*)\Omega_W(\psi(t),\psi^*(t),t), \tag{6.2}$$

where we introduced the Wigner transform $W(\psi,\psi^*)$ of the intitial density matrix ρ:

$$W(\psi,\psi^*) = \frac{1}{2}\int d\eta^* d\eta \left\langle \psi - \frac{\eta}{2}\right| \rho \left|\psi + \frac{\eta}{2}\right\rangle e^{\frac{1}{2}(\eta^*\psi - \eta\psi^*)}, \tag{6.3}$$

and the Weyl symbol:

$$\Omega_W(\psi(t),\psi^*(t),t) = \int d\eta^* d\eta \left\langle \psi(t) - \frac{\eta}{2}\right| \hat{\Omega}(\hat{\psi}(t),\hat{\psi}^\dagger(t),t) \left|\psi(t) + \frac{\eta}{2}\right\rangle e^{\frac{1}{2}(\eta^*\psi - \eta\psi^*)}. \tag{6.4}$$

In the above, we have used the shortened notation $\psi = \psi(t=0)$ for compactness. In this and the following section, for simplicity of presentation, we are considering only a single bosonic mode. The generalisation to spinor condensates on a lattice is straightforward but notationally more cumbersome. The states $\psi(t)$ evolve through the semi-classical equations of motion (for our case, the Gross-Pitaevskii equation). The expression (6.2) can be regarded as an average with a quasi-probability distribution $W(\psi,\psi^*)$. In this chapter we apply (6.2) to the time evolution of the particle population number of the spin one generalisation of the SSH model after a quench in the quadratic Zeeman term in the way it was described in Chapter 4.

6.2 Truncated Wigner Approximation

Prior to considering the quenched dynamics of spinor condensates, we briefly derive the expression (6.2). We follow [89] in our derivation, and for a detailed review we suggest [89].

In order to evaluate (6.1) it is convenient to switch to a basis of coherent states. These are eigenstates of the annihilation operators: $\hat{\psi}\,|\psi\rangle = \psi\,|\psi\rangle$. It can be shown [89] that the relation (6.1) in the coherent state representation

reduces to

$$\langle\Omega(t)\rangle = \int d\psi^* d\psi W(\psi,\psi^*) \int D\psi(\tau) D\psi^*(\tau) \Omega_W(\psi(t),\psi^*(t),t) \\ \times \int D\eta(\tau) D\eta^*(\tau) \exp\left(\int_0^t d\tau \left[\eta^* \partial_\tau \psi - \eta \partial_\tau \psi^*\right]\right) \\ \times \exp\left\{ i \int_0^t d\tau \left[\mathcal{H}_W(\psi+\eta/2,\psi^*+\eta^*/2) - \mathcal{H}_W(\psi-\eta/2,\psi^*-\eta^*/2)\right]\right\}. \tag{6.5}$$

where the Hamiltonian $\mathcal{H}_W$ is Weyl ordered. Weyl ordering can be obtained from a normal ordered Hamiltonian $\hat{\mathcal{H}}(\hat{\psi}^\dagger,\hat{\psi})$ by a replacement $\hat{\psi} \to \psi + \partial_{\psi^*}/2$ and $\hat{\psi}^\dagger \to \psi^* - \partial_\psi/2$. If the Hamiltonian $\mathcal{H}_W$ is expanded in a series of η and η^*, then one notices that in the linear order in η the functional integral over $\eta(\tau)$ enforces a δ-function constraint:

$$i\partial_t \psi(t) = \frac{\partial \mathcal{H}_W(\psi(t),\psi^*(t),t)}{\partial \psi^*(t)}. \tag{6.6}$$

The equation (6.6) is the Gross-Pitaevskii equation for $\psi(t)$. The functions η can thus be regarded as quantum fluctuations about the classical evolution of the system. In this chapter we limit our computation to this linear expansion.

6.3 Quench dynamics of the SSH model

Let us consider a spin-one generalisation of the SSH lattice Hamiltonian:

$$\hat{\mathcal{H}}_{\text{SSH}} = -\sum_j (w + (-1)^j \delta w) \hat{\mathbf{\Psi}}_j^\dagger \hat{\mathbf{\Psi}}_{j-1} + h.c. - \mu \hat{\mathbf{\Psi}}_j^\dagger \hat{\mathbf{\Psi}}_j. \tag{6.7}$$

In the same way as it was introduced in Chapter 4 we consider spin-rotationally invariant interaction terms:

$$\hat{\mathcal{H}}_{\text{int}} = \sum_j \frac{U}{2} \hat{\rho}_j^2 + \frac{U_s}{2} \hat{\mathbf{S}}_j^2. \tag{6.8}$$

We also consider a quadratic Zeeman term $\hat{\mathcal{H}}_Z = q_Z \sum_j \hat{\mathbf{\Psi}}_j^\dagger S_z^2 \hat{\mathbf{\Psi}}_j$.

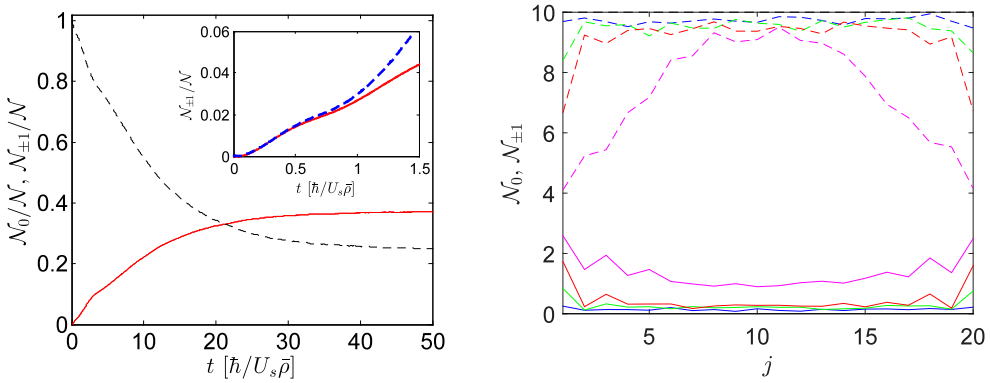

Figure 6.1: Particle population $\mathcal{N}_0$ of spin-0 state (dashed lines) and $\mathcal{N}_{\pm1}$ of spin-±1 state (solid lines) during the time evolution of the SSH model after the quench. Left: The particle population is given per total number of bosons in the system $\mathcal{N}$. In the upper-right corner the particle population (solid red line) is compared with the Bogoliubov prediction from Chapter 4 (dashed blue line) for $t = 0$ to $t = 3/2(\hbar/U_s\bar{\rho})$. A divergence from the Bogoliubov theory is observed after $t = \hbar/U_s\bar{\rho}$. Right: The number of particles per site j in the spin-0 state (dashed lines) and spin-±1 (solid lines) state at different time intervals. The blue lines correspond to the particle population at $t = 1/2(\hbar/U_s\bar{\rho})$, the green lines at $t = \hbar/U_s\bar{\rho}$, red ones at $t = 3/2(\hbar/U_s\bar{\rho})$, and magenta line at $t = 5(\hbar/U_s\bar{\rho})$. The initial state was prepared in spin-0 state with 10 bosons per site. Also, $\delta w = 0.3w$, $U = 2U_s = 0.1w$, $q_f = \mu - 10.5w$ and the lattice has 20 sites.The system was averaged over 500 runs, each with random initial conditions sampled from the Wigner function.

Prior to the quench, the system is prepared in an initial polar state $\mathbf{\Psi}_j(t = 0) = (0, \sqrt{\bar{\rho}}, 0)^{\mathrm{T}}$ with $\bar{\rho}$ bosons per site. The initial state corresponds to the ground state at large q_Z. We can now evaluate the Wigner function (6.3) for the corresponding initial density matrix:

$$W(\mathbf{\Psi}, \mathbf{\Psi}^*) \propto \prod_j e^{-2|\Psi_{j,0}-\sqrt{\bar{\rho}}|^2} e^{-2|\Psi_{j,1}|^2} e^{-2|\Psi_{j,-1}|^2}. \tag{6.9}$$

The (positive) Wigner function corresponds to the normal probability distribution for the present case. Thus one can evaluate the integral in (6.2) by stochastic means. In particular, one averages over semi-classical trajectories with initial conditions given by the probability distribution in (6.9).

The results of such an evolution for a lattice chain of 20 sites are shown in Fig. 6.1. The particle population has been computed numerically using Truncated Wigner Approximation. The final value of the quench parameter has been chosen such that only the edge-states become dynamically unstable in

the short-time evolution. The short-time evolution was found to be in good quantitative agreement with the results from Chapter 4 where Bogoliubov theory was used. At longer times, a saturation of the particle occupation of spin states is observed. This is not predicted by the Bololiubov theory. Deviations from the exponential growth of the particle population are observed at times $t \gg 1/\bar{\rho}U_s$. The small number of sites, $n = 20$, has been chosen because of the computational cost of evaluating systems of large size. For small lattices, however, finite size effects can become considerable. It would be interesting to investigate larger lattice systems in the future.

6.4 Conclusions and outlook

This chapter addressed questions related to the time evolution of quenched boson topological systems beyond regimes of validity of the Bogoliubov treatment that was used in Chapter 4. The Bogoliubov theory predicted growing spin currents at the edge of the lattice. This description, however, was validated for short times $t \lesssim 1/\bar{\rho}U_s$. The Truncated Wigner Approximation, on the other hand, can be utilised to characterise the evolution of the density population and the edge spin current at longer times. The preliminary results for the SSH model, presented in this chapter, suggest a particle redistribution from the edge back into the bulk (Fig. 6.1, right), and a saturation in the particle populations of the spin-± 1 states (Fig. 6.1, left). Whether the same effect can be observed for the spin-one Kane-Mele model is an open question. Two dimensional lattices hide a more interesting dynamics than the one-dimensional SSH model. A deeper investigation of the origin of the density saturation, as well as questions related to the thermalisation of the topological boson lattices constitute new directions for future research in topological quenched dynamics of interacting bosons.

7

Conclusions and future work

The interest in topological phases of matter lies partly in the properties related to topological edge-states. Although such properties have been vastly explored in fermionic systems, topological phenomena that involve bosons are much less investigated, and currently encounter many experimental challenges. One of the modern tools for modelling and investigating condensed matter phenomena is optical lattice experiments with ultracold atoms. The advantages of clean and well-controlled experimental setup is a very unique feature to the field. Nevertheless the very nature of bosons, namely that they condense at sufficiently low temperature, prevents topological edge states from being probed in standard experiments. Moreover, the presence of harmonic confining potential in cold atom experiments obscures the manifestation of the edge states. These are the main questions which were addressed in this thesis. To sum up the results, a mechanism based on quench dynamics of spinor boson condensates has been shown to trigger a fast population of topological edge states, unlocking the boson topological edge dynamics in two-dimensional lattice models in box potential. The effect of harmonic confining potential was also considered. It has been shown that the harmonic potential can be effectively screened out in the Thomas-Fermi regime leading

to a sharpening of the boundaries for trapped atomic gases. The manifestation of the topological edge states, however, was shown to deviate from the case of box potential. An analytical description of edge-state energy and the corresponding bulk-boundary correspondence in presence of harmonic potential has been derived. The results described in this thesis imply a possibility of direct manipulation and observation of topological edge dynamics of interacting spin-one bosons in optical lattice experiments. Below we give a more detailed summary of the results and conclusions obtained per each chapter. We also comment on the outreach of the results and raise some open questions related to this work. Possible future directions of research that can be based on this thesis is also discussed.

In Chapter 3 exact analytical expressions for the edge-state energies of the non-interacting Haldane and Harper-Hofstadter models have been derived using generating function technique. This represents an interesting technical result, especially since the edge state dispersion is experimentally accessible in solids using ARPES measurements [72]. The results of this chapter also helped us finding the instability criteria (4.29) in Chapter 4, as well as the short-time evolution of the particle density (4.33) and the spin current (4.36) of a quenched boson topological lattice system.

Chapter 4 discussed techniques to selectively populated boson topological edge states. It has been shown that due to interactions the topological edge-state dynamics can dominate the time evolution of a quenched system. The Kane-Mele model of spin-one bosons populating a honeycomb lattice has been considered. A spin-rotationally symmetric boson interaction was employed. It was shown that an initial state of polar Bose-Einstein condensate after a quench in the quadratic Zeeman term can lead to an exponential population of the edge modes and an exponentially growing edge spin current. The conclusions are valid for short-time evolution as long as the spin fluctuation can be considered small. The results show promise for the direct experimental probe of the topological edge states in interacting boson spinor condensates.

An important question related to topological band insulators is their classification. Quadratic fermion Hamiltonians have been already classified [91–98]. As was shown in [99, 100] for a topological characterisation of interacting

bosons the symplectic transformation properties need to be taken into account. Moreover, for the quenched dynamics described in Chapter 4 the time-reversal, inversion and S_z symmetries have been found to play an important role in keeping the bulk states dynamically stable, while allowing only for the topological edge states to become dynamically unstable. To my knowledge a full classification of topological band insulator models based on the protection of dynamical stability of bulk states is absent. An interesting problem for future research would hence be to find such a classification.

A flat box-like confining potential with hard-wall boundaries has been employed to derive the results in Chapter 4. The role of more realistic - harmonic - potential represents an important question requiring further investigation for the purpose of experimental value. The question of the effect of harmonic trap has been partly addressed in Chapter 5. Although the results in this chapter suggests a band structure with topological edge modes even in presence of a harmonic potential, the effect of the harmonic trap on quench dynamics has not been investigated. For a more complete theoretical modelling of quench dynamics, which is closer to experimental realisation in atomic gases with harmonic confinement, a consideration harmonic potential in quenched system remains to be investigated. Other ways include engineering interfaces that separate regions of different topological phase [5, 87], and creating confinement sharper than harmonic trap [32–34, 83]. For the Kane-Mele model this could be achieved by implementing a kink in the next nearest neighbour tunnelling amplitude.

Some of the recent advances in modelling condensed matter phenomena in optical lattice experiments have come to question the suitability of mimicking some of solid-state physics phenomena, such as topological band insulators, in optical lattice experiments. For the sake of the modelling of solid-state physics with cold atoms sharp boundaries and flat box-like confining potentials are desirable. Although new techniques of designing sharp boundary conditions have been realised [32–34], creation of such elaborate experimental setups represents a considerable experimental challenge and cost, and currently not many experimental groups have the right capabilities. Chapter 5 investigates the problem of the manifestation of boson topological edge

states in presence of a harmonic potential. A rather simple mechanism based on spinor condensates and which relies on experimentally available setups has been suggested. It implies that the presence of interactions in boson-spinor condensates can actually lead to the sharpening of the boundaries and facilitate the emergence of boson topological edge states in presence of harmonic trap. A two-dimensional topological lattice model of interacting spin-one bosons has been considered. The Bogoliubov energy spectrum of the fluctuations above the macroscopically occupied polar ground state was investigated. It has been shown that in Thomas-Fermi regime the interactions screen the harmonic confining potential, which for a weak spin-interaction strength results in a reconstruction of the non-interacting bulk energy spectrum for the spin ± 1 components of the Bogoliubov modes. A sharpening of the boundaries occurs at the Thomas-Fermi radius, and localised edge states exists outside the Thomas-Fermi radius. The energy of the edge state in the presence of a harmonic trap, however, manifests differently from the case of the box-like confining potential. If in the case of the hard-wall boundaries the band energy gap is closed by chiral edge-states which account for the Chern number of the bulk states, then the presence of a harmonic potential leads to an appearance of multiple edge states crossing the gap. The energy of these edge states has been derived analytically in the adiabatic approximation, giving a rather compact expression that relates edge and bulk quantities (Eq. (5.14)):

$$E_k^{(\bar{n}\nu)} = \mathcal{V}_{\bar{n}} + \frac{1}{2\pi}\int_0^{2\pi} d\varphi \left(\varepsilon_{k,\varphi}^{(\nu)} + \gamma_{\bar{n}} A_{k,\varphi}^{(\nu)} - \frac{s\gamma_{\bar{n}}}{2} Z_{k,\varphi}^{(\nu)}\right),$$

where different values of $\bar{n}$ correspond to edge states localised at different places along the direction of confinement. In the above expression, $\mathcal{V}_{\bar{n}}$ depends only on the confining potential, $\varepsilon_{k,\varphi}^{(\nu)}$ are the single-particle bulk energies, $A_{k,\varphi}^{(\nu)}$ is the Berry connection which carries information of the topological nature of the bulk states onto the edge, and $Z_{k,\varphi}^{(\nu)}$ depends on whether the confining potential acts in a same way inside the lattice unit cell. Further theoretical investigation in Chapter 5 showed that the edge-state energy experiences a jump while crossing the Brillouin zone. Moreover, this jump has been related to the topological invariants of the bulk state, which reflects the

bulk-boundary correspondence for topological band insulators in presence of soft boundaries. The concept was illustrated on the spin-one Kane-Mele model. It has to be mentioned that the computation of the edge-states relied on strip geometry, in which periodic boundary conditions were considered in the direction along one primitive lattice vector, and a harmonic potential in the perpendicular direction. For the complete relevance to experiment one has to consider a radial harmonic potential. We leave this for future research. For a Thomas-Fermi radius much bigger than the lattice characteristic length-scale the approximation used in Chapter 5 gives experimentally realistic conclusions. Another open question that naturally arises is the effect of the harmonic confining potential on quenched dynamics. Due to the sharpening of the boundaries and screening effect inside the Thomas-Fermi radius the method of investigation of boson topological edge states described in Chapter 4 seems to apply, which strengthens the experimental suitability of the techniques described in this thesis.

Some of the conclusions presented in this thesis can be expanded beyond cold atoms, and we hope it will trigger new directions of research. The mean-field approach used in Chapter 4 breaks down at times when the fluctuations become comparable to the population of the condensate. Time evolution of boson topological systems through dynamically unstable phase represents an interesting topic for future research. Preliminary results for such a time evolution presented in Chapter 6 indicate a redistribution of particles from the edge back into the bulk, and a saturation in the particle population of the spin-± 1 states. One can ask whether the same applies for the edge spin current in the Kane-Mele model. In [101] the robustness of topological invariants after a quench has been investigated in a non-interacting fermionic system. Peculiar out-of-equilibrium response has been noticed in the form of light-cone spreading of the currents into the bulk, which relax towards new equilibrium values. Although bosons considerably differ from fermions, and interactions usually complicate theoretical investigation, it would be rather interesting to analyse the thermalisation effects in boson topological band insulators. Do the interactions considerably alter the topological manifestation of the systems reaching thermal equilibrium? Or is the information related

to the topological structure of the system translated to longer time evolution after the quench? Can the topological structure affect the thermalisation of the physical systems and prevent them from reaching a complete thermal equilibrium? These questions naturally rise from the investigation presented in this thesis, and represent a possible direction for future research.

Although this thesis focuses on optical lattice experiments with ultracold atoms, it would be interesting to understand whether similar implications can be made in other areas for the realisation of boson topological phenomena. Whether non-linearities in mechanical and optical systems can trigger similar effects discussed in this thesis poses a particularly intriguing question. Notably, similar ideas have been suggested in photonic crystals in recent years [102, 103], and in Floquet boson models [104]. These systems, however, are usually non-interacting. In photonic crystals, the pairing terms which appeared in the Bogoliubov Hamiltonian in this thesis and which were responsible for the dynamical instability can be generated using parametric amplification [102, 103].

References

[1] Bogdan Galilo, Derek K. K. Lee, and Ryan Barnett. Selective population of edge states in a 2d topological band system. *Phys. Rev. Lett.*, 115:245302, Dec 2015. doi: 10.1103/PhysRevLett.115.245302. URL http://link.aps.org/doi/10.1103/PhysRevLett.115.245302.

[2] Bogdan Galilo, Derek K. K. Lee, and Ryan Barnett. Topological edge-state manifestation of interacting 2d condensed boson-lattice systems in a harmonic trap. *Phys. Rev. Lett.*, 119:203204, Nov 2017. doi: 10.1103/PhysRevLett.119.203204. URL https://link.aps.org/doi/10.1103/PhysRevLett.119.203204.

[3] D.A. King and D.P. Woodruff, editors. *The Chemical Physics of Solid Surfaces and Heterogeneous Catalysis*, volume 5 of *The Chemical Physics of Solid Surfaces*. Elsevier, 1988. doi: https://doi.org/10.1016/B978-0-444-42782-3.50001-7. URL http://www.sciencedirect.com/science/article/pii/B9780444427823500017.

[4] Peter J. Eng, Thomas P. Trainor, Gordon E. Brown Jr., Glenn A. Waychunas, Matthew Newville, Stephen R. Sutton, and Mark L. Rivers. Structure of the hydrated α-Al_2O_3 (0001) surface. *Science*, 288(5468): 1029–1033, 2000. ISSN 0036-8075. doi: 10.1126/science.288.5468.1029. URL http://science.sciencemag.org/content/288/5468/1029.

[5] N. Goldman, G. Jotzu, M. Messer, F. Görg, R. Desbuquois, and T. Esslinger. Creating topological interfaces and detecting chiral edge modes in a two-dimensional optical lattice. *Phys. Rev. A*, 94: 043611, Oct 2016. doi: 10.1103/PhysRevA.94.043611. URL https://link.aps.org/doi/10.1103/PhysRevA.94.043611.

[6] John Bardeen. Surface states and rectification at a metal semi-

conductor contact. *Phys. Rev.*, 71:717–727, May 1947. doi: 10.1103/PhysRev.71.717. URL https://link.aps.org/doi/10.1103/PhysRev.71.717.

[7] Walter H. Brattain. Surface properties of semiconductors. *Nobel Prize Lecture*, 1956.

[8] John Bardeen. Semiconductor research leading to the point contact transistor. *Nobel Prize Lecture*, 1956.

[9] William B Shockley. Transistor technology evokes new physics. *Nobel Prize Lecture*, 1956.

[10] Jed Z. Buchwald and Robert Fox. *The Oxford Handbook of the History of Physics*. Oxford University Press, 2013.

[11] M. Z. Hasan and C. L. Kane. *Colloquium*: Topological insulators. *Rev. Mod. Phys.*, 82:3045–3067, Nov 2010. doi: 10.1103/RevModPhys.82.3045. URL http://link.aps.org/doi/10.1103/RevModPhys.82.3045.

[12] Xiao-Liang Qi and Shou-Cheng Zhang. Topological insulators and superconductors. *Rev. Mod. Phys.*, 83:1057–1110, Oct 2011. doi: 10.1103/RevModPhys.83.1057. URL http://link.aps.org/doi/10.1103/RevModPhys.83.1057.

[13] B Andrei Bernevig. *Topological insulators and topological superconductors*. Princeton University Press, 2013.

[14] K. v. Klitzing, G. Dorda, and M. Pepper. New method for high-accuracy determination of the fine-structure constant based on quantized Hall resistance. *Phys. Rev. Lett.*, 45:494–497, Aug 1980. doi: 10.1103/PhysRevLett.45.494. URL https://link.aps.org/doi/10.1103/PhysRevLett.45.494.

[15] F. D. M. Haldane. Model for a quantum Hall effect without Landau levels: Condensed-matter realization of the "parity anomaly". *Phys. Rev. Lett.*, 61:2015–2018, Oct 1988. doi: 10.1103/PhysRevLett.61.2015. URL http://link.aps.org/doi/10.1103/PhysRevLett.61.2015.

[16] C. L. Kane and E. J. Mele. Z_2 topological order and the quantum spin Hall effect. *Phys. Rev. Lett.*, 95:146802, Sep 2005. doi: 10.1103/PhysRevLett.95.146802. URL http://link.aps.org/doi/10.1103/PhysRevLett.95.146802.

[17] B. Andrei Bernevig, Taylor L. Hughes, and Shou-Cheng Zhang. Quantum spin Hall effect and topological phase transition in HgTe quantum wells. *Science*, 314(5806):1757–1761, 2006. ISSN 0036-8075. doi: 10.1126/science.1133734. URL http://science.sciencemag.org/content/314/5806/1757.

[18] Markus König, Steffen Wiedmann, Christoph Brüne, Andreas Roth, Hartmut Buhmann, Laurens W. Molenkamp, Xiao-Liang Qi, and Shou-Cheng Zhang. Quantum spin Hall insulator state in HgTe quantum wells. *Science*, 318(5851):766–770, 2007. ISSN 0036-8075. doi: 10.1126/science.1148047. URL http://science.sciencemag.org/content/318/5851/766.

[19] Andreas Roth, Christoph Brüne, Hartmut Buhmann, Laurens W. Molenkamp, Joseph Maciejko, Xiao-Liang Qi, and Shou-Cheng Zhang. Nonlocal transport in the quantum spin Hall state. *Science*, 325(5938):294–297, 2009. ISSN 0036-8075. doi: 10.1126/science.1174736. URL http://science.sciencemag.org/content/325/5938/294.

[20] Christoph Brüne, Andreas Roth, Hartmut Buhmann, Ewelina M. Hankiewicz, Laurens W. Molenkamp, Joseph Maciejko, Xiao-Liang Qi, and Shou-Cheng Zhang. Spin polarization of the quantum spin Hall edge states. *Nature Physics*, 8:485 EP –, May 2012. URL http://dx.doi.org/10.1038/nphys2322. Article.

[21] Lisa M. Nash, Dustin Kleckner, Alismari Read, Vincenzo Vitelli, Ari M. Turner, and William T. M. Irvine. Topological mechanics of gyroscopic metamaterials. *Proceedings of the National Academy of Sciences*, 112(47):14495–14500, 2015. doi: 10.1073/pnas.1507413112. URL http://www.pnas.org/content/112/47/14495.abstract.

[22] F. D. M. Haldane and S. Raghu. Possible realization of directional optical waveguides in photonic crystals with broken time-reversal symmetry. *Phys. Rev. Lett.*, 100:013904, Jan 2008. doi: 10.1103/PhysRevLett.100.013904. URL https://link.aps.org/doi/10.1103/PhysRevLett.100.013904.

[23] S. Raghu and F. D. M. Haldane. Analogs of quantum-Hall-effect edge states in photonic crystals. *Phys. Rev. A*, 78:033834, Sep 2008. doi: 10.1103/PhysRevA.78.033834. URL https://link.aps.org/doi/10.1103/PhysRevA.78.033834.

[24] Zheng Wang, Y. D. Chong, John D. Joannopoulos, and Marin Soljačić. Reflection-free one-way edge modes in a gyromagnetic photonic crystal. *Phys. Rev. Lett.*, 100:013905, Jan 2008. doi: 10.1103/PhysRevLett.100.013905. URL https://link.aps.org/doi/10.1103/PhysRevLett.100.013905.

[25] Zheng Wang, Yidong Chong, J. D. Joannopoulos, and Marin Soljacic. Observation of unidirectional backscattering-immune topological electromagnetic states. *Nature*, 461(7265):772–775, Oct 2009. ISSN 0028-0836. doi: 10.1038/nature08293. URL http://dx.doi.org/10.1038/nature08293.

[26] Mikael C Rechtsman, Julia M Zeuner, Yonatan Plotnik, Yaakov Lumer, Daniel Podolsky, Felix Dreisow, Stefan Nolte, Mordechai Segev, and Alexander Szameit. Photonic Floquet topological insulators. *Nature*, 496(7444):196–200, 2013. URL http://dx.doi.org/doi:10.1038/nature12066.

[27] P G Harper. The general motion of conduction electrons in a uniform magnetic field, with application to the diamagnetism of metals. *Proceedings of the Physical Society. Section A*, 68(10):879, 1955. URL http://stacks.iop.org/0370-1298/68/i=10/a=305.

[28] M.Ya. Azbel'. Energy spectrum of a conduction electron in a magnetic field. *Sov. Phys. JETP*, 19:634–645, Aug 1964. URL http://www.jetp.ac.ru/cgi-bin/e/index/e/19/3/p634?a=list.

[29] Douglas R. Hofstadter. Energy levels and wave functions of Bloch electrons in rational and irrational magnetic fields. *Phys. Rev. B*, 14: 2239–2249, Sep 1976. doi: 10.1103/PhysRevB.14.2239. URL https://link.aps.org/doi/10.1103/PhysRevB.14.2239.

[30] M. Aidelsburger, M. Atala, M. Lohse, J. T. Barreiro, B. Paredes, and I. Bloch. Realization of the Hofstadter Hamiltonian with ultracold atoms in optical lattices. *Phys. Rev. Lett.*, 111:185301, Oct 2013. doi: 10.1103/PhysRevLett.111.185301. URL http://link.aps.org/doi/10.1103/PhysRevLett.111.185301.

[31] Hirokazu Miyake, Georgios A. Siviloglou, Colin J. Kennedy, William Cody Burton, and Wolfgang Ketterle. Realizing the Harper Hamiltonian with laser-assisted tunneling in optical lattices. *Phys. Rev. Lett.*, 111:185302, Oct 2013. doi: 10.1103/PhysRevLett.111.185302. URL http://link.aps.org/doi/10.1103/PhysRevLett.111.185302.

[32] Alexander L. Gaunt, Tobias F. Schmidutz, Igor Gotlibovych, Robert P. Smith, and Zoran Hadzibabic. Bose-Einstein condensation of atoms in a uniform potential. *Phys. Rev. Lett.*, 110:200406, May 2013. doi: 10.1103/PhysRevLett.110.200406. URL http://link.aps.org/doi/10.1103/PhysRevLett.110.200406.

[33] Lauriane Chomaz, Laura Corman, Tom Bienaimé, Rémi Desbuquois, Christof Weitenberg, Sylvain Nascimbène, Jérôme Beugnon, and Jean Dalibard. Emergence of coherence via transverse condensation in a uniform quasi-two-dimensional Bose gas. *Nat. Commun.*, 6:6162, 2015. URL http://dx.doi.org/10.1038/ncomms7162.

[34] Biswaroop Mukherjee, Zhenjie Yan, Parth B. Patel, Zoran Hadzibabic, Tarik Yefsah, Julian Struck, and Martin W. Zwierlein. Homogeneous atomic Fermi gases. *Phys. Rev. Lett.*, 118:123401, Mar 2017. doi: 10.1103/PhysRevLett.118.123401. URL https://link.aps.org/doi/10.1103/PhysRevLett.118.123401.

[35] C. L. Kane. Chapter 1 - topological band theory and the $\mathbb{Z}_2$ invariant. In *Topological Insulators*, volume 6 of *Contemporary Concepts of Condensed Matter Science*, pages 3 – 34. Elsevier, 2013. doi: https://doi.org/10.1016/B978-0-444-63314-9.00001-9. URL http://www.sciencedirect.com/science/article/pii/B9780444633149000019.

[36] M. V. Berry. Quantal phase factors accompanying adiabatic changes. *Proceedings of the Royal Society of London A: Mathematical, Physical and Engineering Sciences*, 392(1802):45–57, 1984. ISSN 0080-4630. doi: 10.1098/rspa.1984.0023. URL http://rspa.royalsocietypublishing.org/content/392/1802/45.

[37] W. P. Su, J. R. Schrieffer, and A. J. Heeger. Solitons in polyacetylene. *Phys. Rev. Lett.*, 42:1698–1701, Jun 1979. doi: 10.1103/PhysRevLett.42.1698. URL https://link.aps.org/doi/10.1103/PhysRevLett.42.1698.

[38] A. J. Heeger, S. Kivelson, J. R. Schrieffer, and W. P. Su. Solitons in conducting polymers. *Rev. Mod. Phys.*, 60:781–850, Jul 1988. doi: 10.1103/RevModPhys.60.781. URL http://link.aps.org/doi/10.1103/RevModPhys.60.781.

[39] K. S. Novoselov, A. K. Geim, S. V. Morozov, D. Jiang, Y. Zhang, S. V. Dubonos, I. V. Grigorieva, and A. A. Firsov. Electric field effect in atomically thin carbon films. *Science*, 306(5696):666–669, 2004. ISSN 0036-8075. doi: 10.1126/science.1102896. URL http://science.sciencemag.org/content/306/5696/666.

[40] M. O. Goerbig. Electronic properties of graphene in a strong magnetic field. *Rev. Mod. Phys.*, 83:1193–1243, Nov 2011. doi: 10.1103/RevModPhys.83.1193. URL https://link.aps.org/doi/10.1103/RevModPhys.83.1193.

[41] Claude Cohen-Tannoudji and David Guery-Odelin. *Advances in atomic physics: an overview*. World Scientific Publishing Co. Pte. Ltd., 2011.

[42] C. J. Pethick and H. Smith. *Bose-Einstein Condensation in Dilute Gases*. Cambridge University Press, 2002.

[43] Lev Pitaevskii and Sandro Stringari. *Bose-Einstein Condensation*. Oxford University Press, 2003.

[44] Panayotis G. Kevrekidis, Dmitri J. Frantzeskakis, and Ricardo Carretero-Gonzalez. *Emergent Nonlinear Phenomena in Bose-Einstein Condensates: Theory and Experiment*. Springer, 2008.

[45] M. H. Anderson, J. R. Ensher, M. R. Matthews, C. E. Wieman, and E. A. Cornell. Observation of Bose-Einstein condensation in a dilute atomic vapor. *Science*, 269(5221):198–201, 1995. ISSN 0036-8075. doi: 10.1126/science.269.5221.198. URL http://science.sciencemag.org/content/269/5221/198.

[46] K. B. Davis, M. O. Mewes, M. R. Andrews, N. J. van Druten, D. S. Durfee, D. M. Kurn, and W. Ketterle. Bose-Einstein condensation in a gas of sodium atoms. *Phys. Rev. Lett.*, 75:3969–3973, Nov 1995. doi: 10.1103/PhysRevLett.75.3969. URL https://link.aps.org/doi/10.1103/PhysRevLett.75.3969.

[47] C. C. Bradley, C. A. Sackett, J. J. Tollett, and R. G. Hulet. Evidence of Bose-Einstein condensation in an atomic gas with attractive interactions. *Phys. Rev. Lett.*, 75:1687–1690, Aug 1995. doi: 10.1103/PhysRevLett.75.1687. URL https://link.aps.org/doi/10.1103/PhysRevLett.75.1687.

[48] Marcis Auzinsh, Dmitry Budker, and Simon M. Rochester. *Optically Polarized Atoms: Understanding Light-Atom Interactions*. Oxford University Press, 2010.

[49] Richard A. Dunlap. *An Introduction to the Physics of Nuclei and Particles*. Brooks/Cole, 2004.

[50] M. Weidemüller and C. Zimmermann. *Cold Atoms and Molecules*. Physics textbook. Wiley, 2009. ISBN 9783527407507. URL https://books.google.co.uk/books?id=LTGWwU5XjNAC.

[51] K. Mendelssohn. *The quest for absolute zero: the meaning of the low temperature physics*. Halsted, New York, 1978.

[52] Viktor I Balykin. Ultracold atoms and atomic optics. *Physics-Uspekhi*, 54(8):844, 2011. URL http://stacks.iop.org/1063-7869/54/i=8/a=A06.

[53] V. I. Balykin, V. G. Minogin, and V. S. Letokhov. Electromagnetic trapping of cold atoms. *Reports on Progress in Physics*, 63(9):1429, 2000. URL http://stacks.iop.org/0034-4885/63/i=9/a=202.

[54] L. Fallani and A. Kastberg. Cold atoms: A field enabled by light. *EPL (Europhysics Letters)*, 110(5):53001, 2015. URL http://stacks.iop.org/0295-5075/110/i=5/a=53001.

[55] Harold J. Metcalf and Peter van der Straten. *Laser Cooling and Trapping*. Springer New York, 1999.

[56] Durfee D.S. Stamper-Kurn D.M. Ketterle, W. Making, probing and understanding Bose-Einstein condensates. *arXiv:cond-mat/9904034v2*, 1999. URL https://arxiv.org/abs/cond-mat/9904034v2.

[57] Dan M. Stamper-Kurn and Masahito Ueda. Spinor Bose gases: Symmetries, magnetism, and quantum dynamics. *Rev. Mod. Phys.*, 85: 1191–1244, Jul 2013. doi: 10.1103/RevModPhys.85.1191. URL http://link.aps.org/doi/10.1103/RevModPhys.85.1191.

[58] Yu-Ju Lin and I B Spielman. Synthetic gauge potentials for ultracold neutral atoms. *Journal of Physics B: Atomic, Molecular and Optical Physics*, 49(18):183001, 2016. URL http://stacks.iop.org/0953-4075/49/i=18/a=183001.

[59] A. Celi, P. Massignan, J. Ruseckas, N. Goldman, I. B. Spielman, G. Juzeliūnas, and M. Lewenstein. Synthetic gauge fields in synthetic dimensions. *Phys. Rev. Lett.*, 112:043001, Jan 2014. doi: 10.1103/PhysRevLett.112.043001. URL https://link.aps.org/doi/10.1103/PhysRevLett.112.043001.

[60] Hannah M. Price, Tomoki Ozawa, and Nathan Goldman. Synthetic dimensions for cold atoms from shaking a harmonic trap. *Phys. Rev. A*, 95:023607, Feb 2017. doi: 10.1103/PhysRevA.95.023607. URL https://link.aps.org/doi/10.1103/PhysRevA.95.023607.

[61] Nathan Goldman, G Juzeliūnas, P Ohberg, and Ian B Spielman. Light-induced gauge fields for ultracold atoms. *Reports on progress in physics. Physical Society (Great Britain)*, 77(12):126401–126401, 2014. URL http://dx.doi.org/10.1088/0034-4885/77/12/126401.

[62] Jean Dalibard, Fabrice Gerbier, Gediminas Juzeliūnas, and Patrik Öhberg. Colloquium: Artificial gauge potentials for neutral atoms. *Rev. Mod. Phys.*, 83:1523–1543, Nov 2011. doi: 10.1103/RevModPhys.83.1523. URL https://link.aps.org/doi/10.1103/RevModPhys.83.1523.

[63] Maciej Lewenstein, Anna Sanpera, and Veronica Ahufinger. *Ultracold atoms in optical lattices*. Oxford University Press, 2012.

[64] Gregor Jotzu, Michael Messer, Rémi Desbuquois, Martin Lebrat, Thomas Uehlinger, Daniel Greif, and Tilman Esslinger. Experimental realization of the topological Haldane model with ultracold fermions. *Nature*, 515(7526):237–240, 2014. URL http://dx.doi.org/10.1038/nature13915.

[65] Y.-J. Lin, R. L. Compton, K. Jimenez-Garcia, W. D. Phillips, J. V. Porto, and I. B. Spielman. A synthetic electric force acting on neutral atoms. *Nat Phys*, 7(7):531–534, Jul 2011. ISSN 1745-2473. doi: 10.1038/nphys1954. URL http://dx.doi.org/10.1038/nphys1954.

[66] Colin J. Kennedy, William Cody Burton, Woo Chang Chung, and Wolfgang Ketterle. Observation of Bose-Einstein condensation in a strong synthetic magnetic field. *Nat Phys*, 11(10):859–864, Oct 2015. ISSN 1745-2473. URL http://dx.doi.org/10.1038/nphys3421. Article.

[67] D. H. Lee and J. D. Joannopoulos. Simple scheme for surface-band calculations. i. *Phys. Rev. B*, 23:4988–4996, May 1981. doi:

10.1103/PhysRevB.23.4988. URL https://link.aps.org/doi/10.1103/PhysRevB.23.4988.

[68] D. H. Lee and J. D. Joannopoulos. Simple scheme for surface-band calculations. ii. the green's function. *Phys. Rev. B*, 23:4997–5004, May 1981. doi: 10.1103/PhysRevB.23.4997. URL https://link.aps.org/doi/10.1103/PhysRevB.23.4997.

[69] Sergey S. Pershoguba and Victor M. Yakovenko. Shockley model description of surface states in topological insulators. *Phys. Rev. B.*, 86:075304, 2012. doi: 10.1103/PhysRevB.86.075304. URL http://link.aps.org/doi/10.1103/PhysRevB.86.075304.

[70] Doru Sticlet. *Edge states in Chern Insulators and Majorana fermions in topological superconductors*. Theses, Université Paris Sud - Paris XI, November 2012. URL https://tel.archives-ouvertes.fr/tel-00770666.

[71] Sydney G. Davison and Maria Steslicka. *Basic Theory of Surface States*. Clarendon Press, 1992.

[72] Donghui Lu, Inna M. Vishik, Ming Yi, Yulin Chen, Rob G. Moore, and Zhi-Xun Shen. Angle-resolved photoemission studies of quantum materials. *Annual Review of Condensed Matter Physics*, 3(1):129–167, 2012. doi: 10.1146/annurev-conmatphys-020911-125027. URL https://doi.org/10.1146/annurev-conmatphys-020911-125027.

[73] L. Fallani, L. De Sarlo, J. E. Lye, M. Modugno, R. Saers, C. Fort, and M. Inguscio. Observation of dynamical instability for a Bose-Einstein condensate in a moving 1d optical lattice. *Phys. Rev. Lett.*, 93:140406, Sep 2004. doi: 10.1103/PhysRevLett.93.140406. URL https://link.aps.org/doi/10.1103/PhysRevLett.93.140406.

[74] Zheng Wang, Yidong Chong, JD Joannopoulos, and Marin Soljačić. Observation of unidirectional backscattering-immune topological electromagnetic states. *Nature*, 461(7265):772–775, 2009. URL http://dx.doi.org/doi:10.1038/nature08293.

[75] L. E. Sadler, J. M. Higbie, S. R. Leslie, M. Vengalattore, and D. M. Stamper-Kurn. Spontaneous symmetry breaking in a quenched ferromagnetic spinor Bose-Einstein condensate. *Nature*, 443(7109):312–315, Sep 2006. ISSN 0028-0836. doi: 10.1038/nature05094. URL http://dx.doi.org/10.1038/nature05094.

[76] R. W. Cherng, V. Gritsev, D. M. Stamper-Kurn, and E. Demler. Dynamical instability of the xy spiral state of ferromagnetic condensates. *Phys. Rev. Lett.*, 100:180404, May 2008. doi: 10.1103/PhysRevLett.100.180404. URL https://link.aps.org/doi/10.1103/PhysRevLett.100.180404.

[77] Tomoki Ozawa, Lev P. Pitaevskii, and Sandro Stringari. Supercurrent and dynamical instability of spin-orbit-coupled ultracold Bose gases. *Phys. Rev. A*, 87:063610, Jun 2013. doi: 10.1103/PhysRevA.87.063610. URL https://link.aps.org/doi/10.1103/PhysRevA.87.063610.

[78] Ryan Barnett. Edge-state instabilities of bosons in a topological band. *Phys. Rev. A*, 88:063631, 2013. doi: 10.1103/PhysRevA.88.063631. URL http://link.aps.org/doi/10.1103/PhysRevA.88.063631.

[79] Jean-Paul Blaizot and Georges Ripka. *Quantum theory of finite systems*. Cambridge, Mass. ; London : MIT Press, 1986. ISBN 0262022141.

[80] Y. Nakamura, M. Mine, M. Okumura, and Y. Yamanaka. Condition for emergence of complex eigenvalues in the Bogoliubov˘de Gennes equations. *Phys. Rev. A*, 77:043601, Apr 2008. doi: 10.1103/PhysRevA.77.043601. URL http://link.aps.org/doi/10.1103/PhysRevA.77.043601.

[81] Fabrice Gerbier, Artur Widera, Simon Fölling, Olaf Mandel, and Immanuel Bloch. Resonant control of spin dynamics in ultracold quantum gases by microwave dressing. *Phys. Rev. A*, 73:041602, Apr 2006. doi: 10.1103/PhysRevA.73.041602. URL http://link.aps.org/doi/10.1103/PhysRevA.73.041602.

[82] Tudor D. Stanescu, Victor Galitski, and S. Das Sarma. Topological states in two-dimensional optical lattices. *Phys. Rev. A*, 82:013608, Jul 2010. doi: 10.1103/PhysRevA.82.013608. URL http://link.aps.org/doi/10.1103/PhysRevA.82.013608.

[83] Michael Buchhold, Daniel Cocks, and Walter Hofstetter. Effects of smooth boundaries on topological edge modes in optical lattices. *Phys. Rev. A*, 85:063614, Jun 2012. doi: 10.1103/PhysRevA.85.063614. URL http://link.aps.org/doi/10.1103/PhysRevA.85.063614.

[84] Zhongbo Yan, Bo Li, Xiaosen Yang, and Shaolong Wan. A general time-periodic driving approach to realize topological phases in cold atomic systems. *Scientific Reports*, 5:16197 EP –, Nov 2015. URL http://dx.doi.org/10.1038/srep16197. Article.

[85] Andrey R. Kolovsky, Fabian Grusdt, and Michael Fleischhauer. Quantum particle in a parabolic lattice in the presence of a gauge field. *Phys. Rev. A*, 89:033607, Mar 2014. doi: 10.1103/PhysRevA.89.033607. URL http://link.aps.org/doi/10.1103/PhysRevA.89.033607.

[86] Shunsuke Furukawa and Masahito Ueda. Excitation band topology and edge matter waves in BoseEinstein condensates in optical lattices. *New Journal of Physics*, 17(11):115014, 2015. URL http://stacks.iop.org/1367-2630/17/i=11/a=115014.

[87] Martin Leder, Christopher Grossert, Lukas Sitta, Maximilian Genske, Achim Rosch, and Martin Weitz. Real-space imaging of a topological protected edge state with ultracold atoms in an amplitude-chirped optical lattice. *arXiv:1604.02060*, 2016. URL https://doi.org/10.1038/ncomms13112.

[88] M. Scherer, B. Lücke, G. Gebreyesus, O. Topic, F. Deuretzbacher, W. Ertmer, L. Santos, J. J. Arlt, and C. Klempt. Spontaneous breaking of spatial and spin symmetry in spinor condensates. *Phys. Rev. Lett.*, 105:135302, Sep 2010. doi: 10.1103/PhysRevLett.105.135302. URL http://link.aps.org/doi/10.1103/PhysRevLett.105.135302.

[89] Anatoli Polkovnikov. Phase space representation of quantum dynamics. *Annals of Physics*, 325(8):1790–1852, 2010.

[90] Alex Kamenev and Alex Levchenko. Keldysh technique and non-linear σ-model: basic principles and applications. *Advances in Physics*, 58 (3):197–319, 2009.

[91] Andreas P. Schnyder, Shinsei Ryu, Akira Furusaki, and Andreas W. W. Ludwig. Classification of topological insulators and superconductors in three spatial dimensions. *Phys. Rev. B*, 78:195125, Nov 2008. doi: 10.1103/PhysRevB.78.195125. URL http://link.aps.org/doi/10.1103/PhysRevB.78.195125.

[92] A. Kitaev. Periodic table for topological insulators and superconductors. *AIP Conf. Proc.*, 1134, 2009. URL http://dx.doi.org/10.1063/1.3149495.

[93] Andreas P. Schnyder, Shinsei Ryu, Akira Furusaki, and Andreas W. W. Ludwig. Classification of topological insulators and superconductors. *AIP Conf. Proc.*, 1134(1):10–21, 2009. doi: 10.1063/1.3149481. URL http://aip.scitation.org/doi/abs/10.1063/1.3149481.

[94] Shinsei Ryu, Andreas P. Schnyder, Akira Furusaki, and Andreas W. W. Ludwig. Topological insulators and superconductors: tenfold way and dimensional hierarchy. *New Journal of Physics*, 12(6):065010, 2010. URL http://stacks.iop.org/1367-2630/12/i=6/a=065010.

[95] Gilles Abramovici and Pavel Kalugin. Clifford modules and symmetries of topological insulators. *International Journal of Geometric Methods in Modern Physics*, 09(03):1250023, 2012. doi: 10.1142/S0219887812500235. URL http://www.worldscientific.com/doi/abs/10.1142/S0219887812500235.

[96] Takahiro Morimoto and Akira Furusaki. Topological classification with additional symmetries from Clifford algebras. *Phys. Rev. B*, 88:125129, Sep 2013. doi: 10.1103/PhysRevB.88.125129. URL https://link.aps.org/doi/10.1103/PhysRevB.88.125129.

[97] Xiao-Gang Wen. Symmetry-protected topological phases in noninteracting fermion systems. *Phys. Rev. B*, 85:085103, Feb 2012. doi: 10.1103/PhysRevB.85.085103. URL https://link.aps.org/doi/10.1103/PhysRevB.85.085103.

[98] Ching-Kai Chiu, Jeffrey C. Y. Teo, Andreas P. Schnyder, and Shinsei Ryu. Classification of topological quantum matter with symmetries. *Rev. Mod. Phys.*, 88:035005, Aug 2016. doi: 10.1103/RevModPhys.88.035005. URL https://link.aps.org/doi/10.1103/RevModPhys.88.035005.

[99] Ryuichi Shindou, Ryo Matsumoto, Shuichi Murakami, and Jun-ichiro Ohe. Topological chiral magnonic edge mode in a magnonic crystal. *Phys. Rev. B*, 87:174427, May 2013. doi: 10.1103/PhysRevB.87.174427. URL http://link.aps.org/doi/10.1103/PhysRevB.87.174427.

[100] G. Engelhardt and T. Brandes. Topological Bogoliubov excitations in inversion-symmetric systems of interacting bosons. *Phys. Rev. A*, 91:053621, May 2015. doi: 10.1103/PhysRevA.91.053621. URL http://link.aps.org/doi/10.1103/PhysRevA.91.053621.

[101] M. D. Caio, N. R. Cooper, and M. J. Bhaseen. Quantum quenches in Chern insulators. *Phys. Rev. Lett.*, 115:236403, Dec 2015. doi: 10.1103/PhysRevLett.115.236403. URL https://link.aps.org/doi/10.1103/PhysRevLett.115.236403.

[102] Vittorio Peano, Martin Houde, Christian Brendel, Florian Marquardt, and Aashish A. Clerk. Topological phase transitions and chiral inelastic transport induced by the squeezing of light. *Nat Commun*, 7, Mar 2016. URL http://dx.doi.org/10.1038/ncomms10779. Article.

[103] Vittorio Peano, Martin Houde, Florian Marquardt, and Aashish A. Clerk. Topological quantum fluctuations and traveling wave amplifiers. *Phys. Rev. X*, 6:041026, Nov 2016. doi: 10.1103/PhysRevX.6.041026. URL https://link.aps.org/doi/10.1103/PhysRevX.6.041026.

[104] G. Engelhardt, M. Benito, G. Platero, and T. Brandes. Topological instabilities in ac-driven bosonic systems. *Phys. Rev. Lett.*, 117:045302, Jul 2016. doi: 10.1103/PhysRevLett.117.045302. URL http://link.aps.org/doi/10.1103/PhysRevLett.117.045302.

A

Spin current

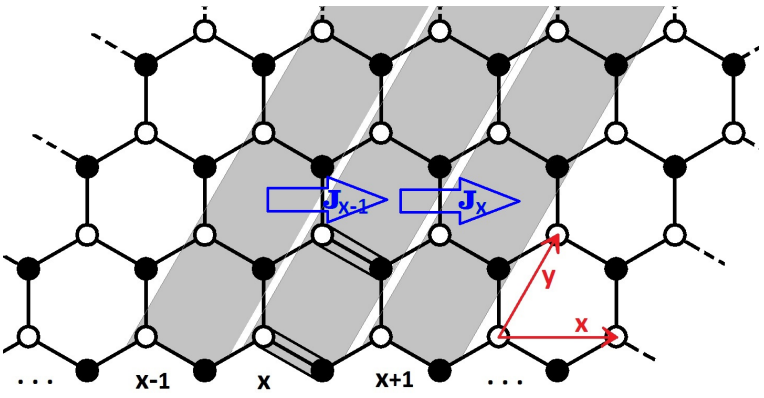

Figure A.1: Schematic illustration of the honeycomb lattice used to compute the spin current.

Here we show how to compute the spin current for the Kane-Mele model discussed in Chapter 3. We start from the continuity equation:

$$\frac{d}{dt}\rho = -\boldsymbol{\nabla} \cdot \mathbf{J} \tag{A.1}$$

where for a one dimensional current along the x-direction the above expression reduces to $\frac{d}{dt}\rho_x = -\partial_x J(x) = -\partial_x \sum_y J(x,y)$. In Fourier space this

equation takes the form:

$$\frac{d}{dt}\rho_q = -iqJ_q. \tag{A.2}$$

We can apply the above expression to our Kane-Mele model in the long wavelength limit:

$$\begin{aligned}
-iqJ_q &= -\frac{d}{dt}\frac{1}{\sqrt{N_x}}\sum_{p,y} a^\dagger_{p+q,y}a_{p,y} = \frac{i}{\sqrt{N_x}}\sum_{p,y}\left[a^\dagger_{p+q,y}a_{p,y}, \hat{\mathrm{H}}\right] \\
&= \frac{i}{\sqrt{N_x}}\sum_{p,y}\sum_{k,y',y''}\left[a^\dagger_{p+q,y,\gamma}a_{p,y,\gamma}, a^\dagger_{k,y',\alpha}a_{k,y'',\beta}\right] h^{\alpha\beta}_{k,y',y''} \\
&= \frac{i}{\sqrt{N_x}}\sum_{p,y}\sum_{k,y',y''}\left[-\delta_{p+q,k}\delta_{y,y''}\delta_{\gamma,\beta}a^\dagger_{k,y',\alpha}a_{p,y,\gamma} + \delta_{p,k}\delta_{y,y'}\delta_{\gamma,\alpha}a^\dagger_{p+q,y,\gamma}a_{k,y'',\beta}\right] h^{\alpha\beta}_{k,y',y''} \\
&= -\frac{i}{\sqrt{N_x}}\sum_{p,y',y''} a^\dagger_{p+q,y',\alpha}\left[h^{\alpha\beta}_{p+q,y',y''} - h^{\alpha\beta}_{p,y',y''}\right] a_{p,y'',\beta} \\
&\overset{p\to p-q/2}{=} -\frac{i}{\sqrt{N_x}}\sum_{p,y',y''} a^\dagger_{p+q/2,y',\alpha}\left[h^{\alpha\beta}_{p+q/2,y',y''} - h^{\alpha\beta}_{p-q/2,y',y''}\right] a_{p-q/2,y'',\beta} \\
&= -\frac{i}{\sqrt{N_x}}\sum_{p,y',y''} a^\dagger_{p+q/2,y',\alpha}\left[q\left(\partial_k h^{\alpha\beta}_{k,y',y''}\right)_{k=p} + \mathcal{O}(q^2)\right] a_{p-q/2,y'',\beta}
\end{aligned}$$

$$J_q = \frac{1}{\sqrt{N_x}}\sum_{p,y',y''} a^\dagger_{p+q/2,y',\alpha}\left(\partial_k h^{\alpha\beta}_{k,y',y''}\right)_{k=p} a_{p-q/2,y'',\beta}$$

Since $\rho_{-1}(t) = \rho_1(t)$ hence $-\partial_x J(x) = \frac{d}{dt}\langle 0|\Psi^\dagger S_z \Psi|0\rangle = 0$ and consequently $J_q \sim \delta_{q,0}$. Therefore

$$J = \frac{1}{\sqrt{N_x}}\sum_{p,y',y''} a^\dagger_{p,y',\alpha}\left(\partial_k h^{\alpha\beta}_{k,y',y''}\right)_{k=p} a_{p,y'',\beta} \tag{A.3}$$

B

Vieta's theorem

Consider a polynomial of degree n:

$$P_n(x) = c_n x^n + c_{n-1} x^{n-1} + ... + c_1 x + c_0, \tag{B.1}$$

where x is a complex variable, and $(c_j)_{j\geq 0}$ are complex number coefficients. The polynomial (B.1) has n roots x_1, x_2,..., x_n (i.e. $P(x_j) = 0,\ j = 1...n$), which can be related with the coefficients $(c_j)_{j\geq 0}$ by Vieta's relations:

$$\begin{aligned}
&x_1 + x_2 + ... + x_n = -\tfrac{c_{n-1}}{c_n},\\
&(x_1x_2 + x_1x_3 + ... + x_1x_n) + (x_2x_3 + x_2x_4 + ... + x_2x_n) + ... + x_{n-1}x_n = \tfrac{c_{n-2}}{c_n},\\
&...\\
&x_1x_2...x_n = -\tfrac{c_0}{c_n}.
\end{aligned} \tag{B.2}$$

In Chapter 3 we are in particular interested in the last relation of (B.2).